# MICROSTRUCTURE DEVELOPMENT UNDER HIGH-GRAVITATIONAL FIELDS

# MICROSTRUCTURE DEVELOPMENT DURING CRYSTALLIZATION OF TIN AND TIN-BASED ALLOYS UNDER HIGH-GRAVITATIONAL FIELDS SIMULATED BY CENTRIFUGAL ACCELERATION

**By**

**JACKIE LEUNG, B.ENG.MGMT.**

A Thesis

Submitted to the School of Graduate Studies

in Partial Fulfillment of the Requirements

for the Degree

Master of Applied Science

McMaster University

MASTER OF APPLIED SCIENCE (2009) McMaster University

(Materials Science and Engineering) Hamilton, Ontario

TITLE: Microstructure Development during Crystallization of Tin and Tin-Based Alloys under High-Gravitational Fields Simulated by Centrifugal Acceleration

AUTHOR: Jackie Leung, B.Eng.Mgmt. (McMaster University)

SUPERVISOR: Dr. G.P. Johari, Professor Emeritus

NUMBER OF PAGES: xiii, 120

## ABSTRACT

Succinonitrile, commercially-pure Sn, Sn-0.3 wt% Cu, and Bi-Sn of several weight ratios were solidified under high-gravitational fields 287 times that of the earth's gravity simulated by centrifugal acceleration. The microstructure of the samples solidified in high-gravity was examined and compared with those solidified in normal gravity. Solidification was also done under varying cooling rates to determine its combined effect with high-gravity on microstructure development. The microstructure was quantified in terms of grain size, eutectic spacing, and primary phase distribution against the radial position of the samples. Vickers hardness of the samples was also measured by using both low load and a high load, in order to determine the solidified samples' relative strength.

The microstructure of the Sn sample solidified in high-gravity possessed a higher percentage of small grains than that solidified in normal gravity. For Bi-Sn alloys solidified by slow-cooling, the eutectic phase formed in high-gravity had a complex but regular lamellar structure whereas that formed in normal gravity was irregular. In the hyper- and hypoeutectic Bi-Sn sample, the primary phase was segregated to the inner or outer radius of the samples formed in high-gravity, depending on the variation of density between the phases. The Sn-Cu alloy solidified in high-gravity had a cellular structure whereas that solidified in normal gravity had a dendritic structure.

The effects of high-gravity on microstructure development are explained by the enhanced fluid flow and Rayleigh-Bénard convection during solidification of the melt. This convection is caused by thermally-induced density gradients within the melt and is confirmed by calculating the Rayleigh number. Other effects on microstructure are explained in terms of the Stokes equation and the Mullins-Sekerka criteria for solidification stability. Change in the solidification temperature as a result of increasing centrifugal acceleration was calculated from the Clausius-Clapeyron equation, and its magnitude is discussed.

## ACKNOWLEDGEMENTS

I would like to acknowledge the following individuals for their assistance during the development of this work. Without their help, I would not have been able to complete this degree. First, I would like to express my sincerest gratitude to Dr. G.P. Johari; his supervision and advice during this research has been most appreciated. I would also like to thank the lab technicians and lab managers of the Materials Engineering laboratory: Doug Culley, John Rodda, and Ed McCaffrey for their advice and assistance in the sample preparation and analyses of this research; the administrative staff of the Materials Engineering department; the Student Machine Shop supervisor, Mr. Paul Bray, for his consultation and guidance during the design and machining of the experimental components in addition to the training that he provided so that I could use the machines; my fellow graduate students who contributed their ideas and advice during my research; in particular Mr. Daisman Aji for his assistance developing the software for analysis. Finally, I would like to thank Dr. S. Shankhar for his course on Solidification Processing and Dr. H. Zurob for his course on Phase Transformations.

## TABLE OF CONTENTS

## LIST OF FIGURES

## LIST OF TABLES

# CHAPTER 1: INTRODUCTION

Microstructure development on solidification and crystal growth are critical aspects of materials science and engineering. Since these processes occur on Earth, gravity plays a role in the development of the final microstructure. Gravitational fields affect the fluid flow in a melt, thereby changing thermal diffusion, and hence its solidification morphology and the microstructure (Flemings 1974). Many important material properties such as toughness, corrosion resistance, and electrical conductivity are determined by a material's microstructure (Glicksman et al. 1995). Gravitational fields also play a role in the development of macroscopic properties such as porosity, sedimentation, and void formation (Müller 1990). Although the microstructure can typically be improved by subsequent mechanical or thermal heat treatments, the initial microstructure is still important to the success of those treatments (Glicksman et al. 1995).

Thermal and concentration gradients that develop within a melt cause unstable density gradients. Due to the buoyancy effect, these density gradients cause convective instabilities within the melt. In the gravitational field of Earth, the buoyancy effect is relatively constant. If the gravitational field was increased in a laboratory, the magnitude of buoyancy-induced convection would be enhanced and so the microstructure would be affected. To simulate the effects of a high-gravitational field, a device designed to produce centrifugal acceleration, otherwise known as a centrifuge, was used. Centrifuges have been used to enhance gravity in many areas of materials processing and medical sciences, mainly to separate particles or fluids of different densities in liquids and gases. For example, centrifuges are used to purify raw uranium into refined uranium based on the different molecular weights of their isotopes (Fishlock 2004). Centrifuges are also commonly used in medical technology to separate proteins and particles from fluids. Large devices to generate centrifugal acceleration are used by NASA to train their astronauts to withstand the high-gravitational forces that are experienced during a shuttle launch. It has been proposed that short-radius centrifuges could be used in space to create artificial gravity environments for astronauts in order to reduce the physiological effects of microgravity during long-term space missions (Scott 2005).

Solidification in high-gravity simulated by centrifugal acceleration is analogous to an industrial process known as *centrifugal casting*. This process involves a melt being poured into a spinning mould rotated along its center axis. As a result, the melt is pushed towards the walls of the mould and allowed to solidify. Centrifugally cast products have several benefits over other conventional castings such as a denser and more uniform grain structure, reduced porosity, and segregation of impurities to the outer or inner surface (depending on densities) that could be machined away. Centrifugal casting is commonly used for the production of symmetric components such as high-speed train wheels, weld-free pressure vessels, and steel rollers. It has also been used to overcome the high viscosity of liquid metals during the production of jewelry where high-

detail is required. Solidification in high-gravity also has added benefits for single-crystal growth. Rodot, Regel, and Turtchaninov (1990) grew large single crystals for semiconductor applications using the Bridgman technique under centrifugal acceleration and found that at certain levels of simulated gravity, the crystals exhibited greater perfection and the impurity profile was similar to a purely diffusive crystal growth. Centrifugal casting has also been used to produce inclusion-free optical crystals for use in telescopic mirrors and lenses (Shlichta 1992).

Most solidification models typically have not included melt convection into their parameters. These models have shown to work in microgravity conditions, but not in normal gravity conditions (Glicksman et al. 1995). Only recently has melt convection and fluid motion been taken into consideration. Other models that take gravity into consideration are limited to gravity levels between microgravity and terrestrial gravity. In order for a true solidification model to work, it must hold up to all levels of gravity. Other experiments have been performed in high-gravity up to $10^6 g_0$, where $g_0 = 9.81$ m/s$^2$ (Regel 1987).

In this thesis, melts were solidified under a high-gravitational field simulated by spinning the melts along its center axis thereby generating centrifugal acceleration using a custom-built device. Microstructures of the samples solidified under centrifugal acceleration (analogous to high-gravity) were examined and compared with the microstructures of the samples of the same materials, but solidified without centrifugal acceleration (analogous to terrestrial gravity). After relatively less successful experiments on succinonitrile, an organic material often used as a model for the study of solidification (Glicksman et al. 1995), studies were done on commercially-pure Sn, and several Bi-Sn alloys. Low-melting materials were selected instead of high-melting materials due to the physical limitations of the research equipment. Microstructure properties such as average grain size, grain size distribution, and eutectic spacing were studied. The strength of the solidified samples was determined in terms of the Vickers hardness. It was believed that by varying the gravitational field on Earth, microstructure development on solidification could be optimized (Müller 1990). It should be noted that "true gravity" is not being generated since the Newtonian force of attraction between two large bodies of mass is expressed as:

$$F_g = \frac{G m_1 m_2}{r^2} \tag{1.1}$$

where $F_g$ is the force of gravitational attraction [N], $G$ is the gravitational constant ($6.67\times10^{-11}$ m$^3$/kg·s), $m_1$ and $m_2$ are the masses of the two bodies [kg], and $r$ is the distance between the centers of each body of mass. Although gravity cannot be replicated, its effects could still be simulated by generating centrifugal acceleration. Therefore in this thesis, spinning an object along its center axis to produce centrifugal acceleration will be referred to as producing "high-gravity," a terminology used in this field.

Some of the results of these studies were presented at the ASM poster competition in March 2009 and the Canadian Materials Science Conference in June 2009.

# CHAPTER 2: THEORETICAL ASPECTS OF CONVECTION, SOLIDIFICATION, AND GRAVITY

## 2.1 Thermal Convection

There are two ways that thermal instabilities cause fluid convection within a liquid: buoyancy-induced convection or *Rayleigh-Bénard convection*, and capillary-induced convection or *Marangoni convection* (Koschmieder 1993).

### 2.1.1 Buoyancy-Induced Thermal Convection

To explain Rayleigh-Bénard convection, consider a horizontal layer of liquid at rest and sandwiched between two metal plates; the top and bottom plates are respectively cooled and heated creating a thermal gradient. The liquid near the bottom plate would be heated through conduction and its volume would increase. Simultaneously, the liquid near the top plate would be cooled and its volume would decrease. As a result, there would be an unstable density gradient within the liquid which would cause convection due to the buoyancy effect. Figure 2.1 shows an illustration describing Rayleigh-Bénard convection.

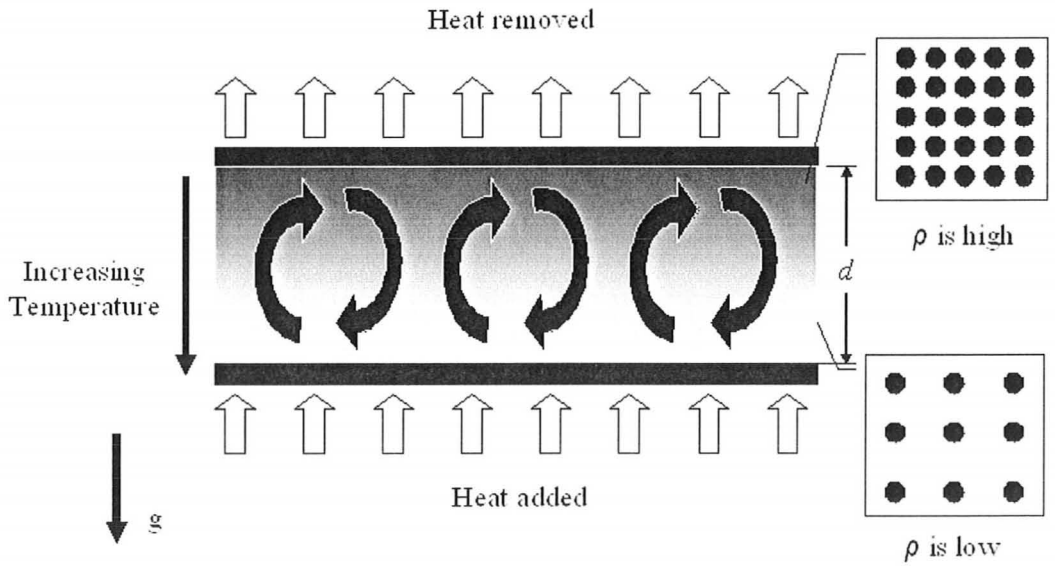


Figure 2.1: An illustration demonstrating Rayleigh-Bénard convection

In Figure 2.1, the horizontal layer of liquid (white to black region) of depth, $d$, and of infinite length and width is "sandwiched" between two parallel metal plates (black rectangles). The liquid is heated from below by the bottom plate and cooled from above by the top plate creating a thermal gradient parallel to the direction of the gravitational field. Assuming the liquid has a positive coefficient of thermal expansion; the liquid would expand when heated and contract when cooled. Since the liquid near the bottom plate (white region) is heated, it would

expand making it less dense than the liquid at the top. Conversely, the liquid near the top plate (black region) is cooled causing it to contract and become denser than the liquid at the bottom. This creates an unstable density gradient between the top and bottom regions of the liquid so that the cold liquid at the top would be driven to "sink" to the bottom and the hot liquid at the bottom would be driven to "float" to the top. When the hot liquid reaches the top, it would cool down causing it to contract and return to the bottom. Simultaneously, when the cold liquid from the top reaches the bottom, it would heat up causing it to expand making it return to the top. This creates a convective loop (depicted by the black arrows) that would be sustained as long as the top and bottom plates remain cooled and heated, respectively (Koshmieder 1993).

In order for convection to occur, the buoyancy effect must overcome the liquid's internal viscosity. Otherwise, the fluid would remain static and heat transfer would only occur by thermal conduction. Therefore, the temperature difference between the top and bottom plates must be greater than a critical value for convection to occur. The Rayleigh number, *Ra*, is a non-dimensional number that compares the viscosity and thermal conductivity of a fluid to the buoyancy effect on a fluid with a known thermal gradient to describe Rayleigh-Bénard convection. The Rayleigh number is expressed as:

$$Ra = \frac{\alpha g \beta d^4}{\upsilon \kappa} \tag{2.1}$$

where $\alpha$ is the coefficient of thermal expansion [/K], $g$ is the gravitational acceleration [m/s$^2$], $d$ is the depth of the fluid [m], $\beta$ is the vertical thermal gradient between the two boundaries [K], $\upsilon$ is the kinematic viscosity [m$^2$/s], and $\kappa$ is the thermal diffusivity [m$^2$/s] (Koschmieder 1993). Kinematic viscosity is the ratio of viscous force to inertial force expressed as:

$$\upsilon = \frac{\mu}{\rho} \tag{2.2}$$

where $\mu$ is the dynamic viscosity [kg/(m·s)] and $\rho$ is the density [kg/m$^3$]. Thermal diffusivity is the ratio of thermal conductivity to volumetric heat capacity expressed as:

$$\kappa = \frac{K}{\rho \cdot c_p} \tag{2.3}$$

where $K$ is the thermal conductivity [W/(m·K)] and $c_p$ is the specific heat capacity [J/(m·K)]. Therefore, the expanded Rayleigh number can be expressed as:

$$Ra = \frac{\alpha g \beta d^4}{\frac{K}{\rho c_p}\frac{\mu}{\rho}} \tag{2.4}$$

The Rayleigh number can also be expressed as the product of the Prandtl number and the Grashof number:

$$Ra = (Pr)(Gr) \tag{2.5}$$

where the Prandtl number, *Pr*, is a non-dimensional number expressing the ratio of kinematic viscosity to thermal diffusivity:

$$Pr = \frac{\upsilon}{\kappa} \tag{2.6}$$

and the Grashof number, *Gr*, is a non-dimensional number expressing the ratio of buoyancy to viscous forces:

$$Gr = \frac{\alpha g \beta d^4}{\upsilon^2} \tag{2.7}$$

At the critical Rayleigh number, a fluid will undergo a transition from no fluid motion to laminar fluid motion (Koschmieder 1993). The value of the critical Rayleigh number depends on the conditions of the surfaces confining the fluid which can either be a rigid like a metal plate, or non-rigid such as air or another fluid (Koschmieder 1993). The critical Rayleigh numbers are 1707.8 for rigid-rigid boundary conditions, 1100.7 for rigid-non-rigid boundary conditions, and 657.5 for non-rigid-non-rigid boundary conditions (Koschmieder 1993). The critical Rayleigh numbers for non-rigid boundary conditions are lower because the presence of surface tension fluctuations assists the onset of convection. A higher Rayleigh number would indicate that convection would become more turbulent. In practice, Rayleigh-Bénard convection could only be fully realized under rigid-rigid boundary conditions, but in principle Rayleigh-Bénard convection could also be realized under rigid-non-rigid and non-rigid-non-rigid boundary conditions if surface-traction is neglected (Koschmieder 1993).

### 2.1.2 Capillary-Induced Thermal Convection

To explain Marangoni convection, consider a thin horizontal layer of fluid being heated from below by a metal plate and cooled from above by air. Also consider that a warm spot forms on the surface of the fluid creating a lateral thermal gradient. Assuming surface tension of the fluid decreases with increasing temperature, the hot spot would be "softer" than the colder regions of the fluid surface (Koschmieder 1993). This would be the driving force for the fluid at the surface to move and distribute itself evenly to a single temperature and surface tension (Chereminsinoff 1986). As a result, the fluid at the hot spot would be drawn away laterally from that spot pulling fluid from the bottom to the surface creating convective motion. Although Marangoni convection is caused by unstable thermal gradients much like Rayleigh-Bénard convection, it is not directly affected by buoyancy so that there does not have to be a vertical density gradient for the bottom fluid to move to the top (Koschmieder 1993).

Under microgravity conditions, the lack of gravity would enhance the effect of Marangoni convection (Glicksman et al. 1995). Similar to Rayleigh-Bénard convection, there is a critical thermal gradient for the onset of Marangoni convection. This is described by the Marangoni number, *Ma*, a non-dimensional number expressed as:

$$Ma = \frac{\partial S}{\partial T}\frac{\Delta Tl}{\rho \upsilon \kappa} \tag{2.8}$$

where $\partial S / \partial T$ is the relationship of surface tension to temperature [N/(m·K)] and $l$ is the characteristic length (Koschmieder 1993). The critical Marangoni number for the onset of convection is 79.6 (Koschmieder 1993). In non-rigid-non-rigid or rigid-non-rigid boundary conditions, Marangoni convection and Rayleigh-Bénard convection could occur simultaneously, but one would be more dominant than the other depending on the physical conditions. The relationship between Rayleigh-Bénard and Marangoni convection is expressed as:

$$\frac{Ma}{Ma_{Cr}} + \frac{Ra}{Ra_{Cr}} \cong 1 \tag{2.9}$$

where $Ra_{Cr}$ is the critical Rayleigh number and $Ma_{Cr}$ is the critical Marangoni number (Koschmieder 1993). If the Rayleigh number is close to the critical Rayleigh number, then the Marangoni number would be small and buoyancy-induced convection would dominate. Conversely, if the Marangoni number is close to the critical Marangoni number, capillary-induced convection would dominate.

## 2.2 General Aspects of Solidification

### 2.2.1 Nucleation and Crystal Growth

Solidification occurs in two steps: nucleation and crystal growth (Porter and Easterling 1992). When the temperature of the melt is below its freezing temperature, the melt is in a state of undercooling which would provide the driving force for nucleation to occur (Porter and Easterling 1992). The rate of nucleation is determined by the degree of undercooling within the melt. If the melt was contained in a mould, the mould would have many nucleation sites so that nucleation would be heterogeneous (Porter and Easterling 1992). The heterogeneous nucleation rate is expressed as:

$$N_{het} = f_1 C_1 \exp\left(-\frac{\Delta G^*_{het}}{k_B T}\right) \tag{2.10}$$

where $N_{het}$ is the nucleation rate [nuclei/(m$^3$·s)], $f_1$ is a complex function dependent on the vibration frequency of the atoms, $C_1$ is the number of atoms per unit volume, $\Delta G_{het}$* is the change in free energy due to undercooling, $k_B$ is the Boltzmann constant ($1.38\times10^{-23}$ J/K), and $T$ is the temperature of the melt [K] (Porter and Easterling 1992). During crystal growth, the liquid undergoes a reversible isothermally change in enthalpy which is an exothermic process, meaning it releases energy. The amount of energy that is released when the atomic arrangement changes from a disordered structure to an ordered structure is known as the latent heat of solidification. When the growing crystal releases energy, the energy would be absorbed by the surrounding melt which would be converted to thermal energy and cause the melt to increase in temperature. The

crystal growth rate, or solid-liquid interface velocity, is determined by the rate at which latent heat is transported away from the solid-liquid interface (Porter and Easterling 1992). If heat transport was only through thermal conduction, the solid-liquid interface velocity would be expressed as:

$$R = \frac{K_S G_S - K_L G_L}{\rho_S L} \tag{2.11}$$

where $R$ is the solid-liquid interface velocity [m/s], $K_S$ and $K_L$ are respectively the solid and liquid thermal conductivities [W/(m·K)], $G_S$ and $G_L$ are respectively the solid and liquid thermal gradients at the solid-liquid interface [K/m], $\rho_S$ is the density of the solid [kg/m$^3$]; and $L$ is the latent heat of solidification [J/kg] (Flemings 1974). By assuming the solid-liquid interface velocity is controlled by thermal conductivity only, the crystal growth rate would not depend on gravity. However, convection could occur in the melt and increase the rate of heat transport away from the interface, thereby increasing the crystal growth rate.

In the case of alloys, crystal growth also occurs by the expulsion of solute atoms so that there would be a buildup of solute atoms ahead of the solid-liquid interface, thereby creating a concentration gradient. The rate of crystal growth would be controlled by the rate at which solute atoms were transported away from the solid-liquid interface (Flemings 1974). If the solute atoms have a different density than the bulk material, then the concentration gradient would also create a density gradient which could cause buoyancy-induced convection in the melt.

### 2.2.2 Solidification and Convection

There are several ways that convection and fluid motion could occur during solidification. First, if the melt was cooled from the top, nucleation would occur at the top and crystal growth would be in the downward direction. In this scenario, the top of the melt would be colder than the bottom thereby creating an unstable density gradient so that Rayleigh-Bénard convection would occur before the onset of nucleation. Second, if the melt was cooled from the bottom, nucleation would occur at the bottom and crystal growth would be in the upward direction. In this case, there would be virtually no convection before the onset of nucleation. However after nucleation, the subsequent crystal growth would release latent heat causing a localized increase in temperature at the bottom of the melt ahead of the solid-liquid interface. If the melt ahead of the solid-liquid interface was warmer than at the top, the melt at the bottom would be less dense creating an unstable density gradient and cause Rayleigh-Bénard convection. The densities of the solid and liquid phases of the same material also differ because the atomic arrangement of a solid is different from its liquid counterpart. In most metals, a solid is heavier than its liquid counterpart with some exceptions such as Bi. Consider a third scenario where nucleation would occur in the middle of the melt instead of the bottom or the top. When crystal growth begins, the crystal becomes heavier than the melt so it would sink to the bottom of the liquid as it continued to grow. As the crystal sinks, there would be forced convection along

its surface, further increasing the transport of heat away from the solid-liquid interface. The velocity of the growing crystal in the melt will depend on gravity, buoyancy, and viscosity. When a spherical particle moves through a fluid at a constant velocity, there would be three forces exerted on it: gravity, buoyancy, and drag. The gravitational force is expressed as:

$$F_g = mg \tag{2.12}$$

where $F_g$ is the force of gravity [N], $m$ is the mass of the object [kg], and $g$ is the gravitational acceleration [m/s$^2$]. The buoyancy force is directly proportional to gravity and is expressed as:

$$F_b = -\rho_{fl} V_{sub} g \tag{2.13}$$

where $F_b$ is the force of buoyancy [N], $\rho_{fl}$ is the fluid density [kg/m$^3$], $V_{sub}$ is the volume of the object submerged in the fluid [m$^3$], and $g$ is the gravitational acceleration [m/s$^2$]. The drag force, determined by *Stokes law*, is proportional to the velocity of the particle in the melt and is expressed as:

$$F_d = 6\pi\mu r v \tag{2.14}$$

where $F_d$ is the drag force [N], $\mu$ is dynamic viscosity [kg/(m·s)], $r$ is the radius of the particle [m], and $v$ is the velocity of the particle [m/s]. Because the particle is assumed to be moving at constant velocity, the drag force must be equal and opposite to the net force of gravity and buoyancy. Therefore, the velocity of a particle of a fixed radius could be calculated for different gravitational fields using the *Stokes formula*:

$$v = \frac{2gr_{particle}^2(\rho_{particle} - \rho_{fluid})}{9\mu} \tag{2.15}$$

where $v$ is the velocity of the particle [m/s], $\mu$ is the viscosity of the fluid [kg/(m·s)], and $r_{particle}$ is the radius of the particle (Chalmers 1964). By increasing the gravitational acceleration, one could increase the velocity of the particle and hence the forced convection around it.

### 2.2.3 Solid-Liquid Interface Stability

Microstructure development is also dependent on stability of the solid-liquid interface (Flemings 1974). The solid-liquid interface, also known as the solidification front, could be planar, cellular, or dendritic, depending on its stability. In order for the solid-liquid interface to be stable and hence, planar, it must follow the Rutter-Chalmers (1953) relationship for stable solidification expressed as:

$$\frac{G_L}{R} \geq -\frac{m_L C_S^*(1-k)}{kD_L} \tag{2.16}$$

where $G_L$ is the thermal gradient of the liquid immediately ahead of the solid-liquid interface [K/m], $R$ is interface velocity [m/s], $m_L$ is the slope of the liquidus line [K/wt%], $k$ is the equilibrium partition ratio (slope of liquidus over slope of solidus), $D_L$ is the diffusion coefficient [m$^2$/s], and $C_S$* is the solute concentration

of the solid fraction (Flemings, 1974). If the term on the left, $G_L/R$, is greater than or equal to the critical value, the term on the right, then the solidification would be stable and the interface would be planar. However, if the term on the left is less than the term on the right, solidification would be unstable and the interface will be would be cellular or dendritic, depending on the difference between the ratio and critical value. The term, $C_S$*, could be changed depending on the presence of convection. When there is no convection in the melt, Equation (2.16) becomes:

$$\frac{G_L}{R} \geq -\frac{m_L C_0 (1-k)}{kD_L} \tag{2.17}$$

where $C_0$ is the initial composition of the material (Flemings 1974). Conversely, when there is perfect convection in the melt, Equation (2.16) becomes:

$$\frac{G_L}{R} \geq -\frac{m_L C_\infty (1-k)}{D_L} \tag{2.18}$$

where $C_\infty$ is the solute concentration in the bulk liquid which is equal to $C_0$ during the initial onset of solidification in the melt (Flemings 1974). With perfect convection, the critical value for stable solidification decreases. The Rutter-Chalmers relationship for stable solidification only considers stability based on thermodynamics. Under certain solidification conditions, stability can also be highly dependent on thermal conductivity. The Mullins-Sekerka (1963) relationship for stable solidification is expressed as:

$$\frac{G_L}{R} + \frac{\rho_L L}{2K_L} \geq -\frac{m_L C_\infty (1-k)}{kD_L} \frac{K_S + K_L}{2K_L} \zeta \tag{2.19}$$

where $L$ is the latent heat of solidification [J], $K_L$ and $K_S$ are the respective liquid and solid thermal conductivity [W/(m·K)], and $\zeta$ is a dimensionless stability function (Flemings 1974). When the thermal gradient is low and the interface velocity is high, $L/2K_L$ becomes important and dominates the left side (Flemings 1974).

## 2.3 Gravity and Hydrostatic Pressure

Another effect of gravity on solidification is based upon the change in the hydrostatic pressure. According to Swalin (1972), a change in hydrostatic pressure can affect the temperature of a phase transformation. Depending on whether the material contracts or expands during transformation and whether the transformation is exothermic or endothermic, increasing hydrostatic pressure could either increase or decrease the transformation temperature. The relationship between the change in hydrostatic pressure and the change in transformation temperature is known as the simplified *Clausius-Clapeyron equation* which is expressed as:

$$\Delta T = \frac{T_{trans} \Delta V \Delta P}{L} \tag{2.20}$$

where $\Delta T$ is the change in transformation temperature [K], $\Delta p$ is the change in hydrostatic pressure [Pa], $L$ is the change in enthalpy per unit mass [J/kg], $T_{trans}$ is the transformation temperature at 1 atm [K], and $\Delta V$ is the change in volume [$m^3$/kg] (Swalin 1972). The derivation of the simplified Clausius-Clapeyron equation is given in Appendix A.1. The simplified equation for hydrostatic pressure of a liquid of uniform density is expressed as:

$$P = \rho g h + p_0 \tag{2.21}$$

where $P$ is the hydrostatic pressure [Pa], $h$ is height of the fluid [m], and $p_0$ is the atmospheric pressure [Pa]. For a transformation of phase-1 to phase-2, the change in volume per unit mass is expressed as:

$$\Delta V = \frac{1}{\rho_2} - \frac{1}{\rho_1} \tag{2.22}$$

where $\Delta V$ is the change in volume per unit mass [$m^3$/kg], and $\rho_1$ and $\rho_2$ are the densities of the phases involved in the transformation [kg/$m^3$] (Swalin 1972).

In summary, the earth's gravitational field causes Rayleigh-Bénard convection to occur in a melt during solidification. Furthermore, the variance in density between a solid and liquid causes the solid to sink in the melt creating forced convection. If the gravitational field was completely absent as in outer space, there would be no Rayleigh-Bénard convection during solidification. However, other fluid transport mechanisms such as Marangoni convection could cause convection during solidification. Conversely, if the gravitational field was enhanced as done here in the laboratory, the intensity of Rayleigh-Bénard convection would be increased.

# CHAPTER 3: LITERATURE REVIEW

## 3.1 Development of Rayleigh-Bénard Convection

The first quantitative study of buoyancy-induced convection began with the experiment conducted by Henri Bénard (1900) with heated oil. There had been earlier observations on buoyancy-induced fluid convection, but these were qualitative and not conducted in a controlled, repeatable environment (Chandrasekhar 1961). Bénard's experiment consisted of a shallow layer of fluid in an open circular container with a high aspect ratio (diameter-to-height), heated from below through a metal plate (Koschmieder 1993). This would later become known as the 'Bénard configuration.' The fluid that Bénard used was molten spermaceti, a whale oil, which has a wax-like consistency at room temperature, but would become liquid at 46°C. The top surface of the oil in Bénard's experiment was not confined by a metal plate, but rather cooled by ambient air. Bénard observed a stable, steady-state, regular pattern of hexagonal convective cells on the surface of the heated oil which were made visible by placing fine particles of graphite or aluminum powder and grains of lycopodium in the oil (Koschmieder 1993). Bénard originally attributed the cell pattern to the fluid being heated from below and changes in surface tension; he never considered there would be a critical temperature difference between the top and bottom layers of the fluid (Koschmieder 1993). Although the hexagonal cells that Bénard observed had little to do with buoyancy, it was a critical step to the development of Rayleigh-Bénard convection and Marangoni convection.

Lord Rayleigh (1916) furthered Bénard's work when he viewed it as a stability problem and attempted to solve it analytically. Rayleigh considered a fluid confined within two infinitely long, parallel plates held at two different temperatures: the bottom plate being heated and the top plate being cooled. In the analysis, Rayleigh used the Euler equation and the equation of thermal expansion, and neglected the nonlinear terms and used the Boussinesq (1903) approximation (Koschmieder 1993). The Boussinesq approximation assumes that material properties such as thermal expansion, thermal diffusivity, and kinematic viscosity do not vary with temperature with the exception of density (Oertel 1983). Rayleigh also assumed the boundaries were essentially free surfaces and perfect thermal conductors and neglected surface tension gradients, thereby distinguishing his work from Bénard's because Bénard's experiment highly depended upon the surface traction caused by surface tension gradients (Koschmieder 1993). Rayleigh also considered the effect of fluid viscosity and proposed that there would be a critical thermal gradient needed to overcome the dissipation of heat by viscosity and thermal conductivity for the onset of convection (Koschmieder 1993). This would be a significant step in the development of the concepts of Rayleigh-Bénard convection. Now, convection caused by heating from below and not affected by surface tension gradients is known as the Rayleigh-Bénard problem.

The onset of Rayleigh-Bénard convection can be determined by the non-dimensional Rayleigh number, which was developed from equations of the conservation of mass, momentum, and energy (Koschmieder 1993). Jeffreys (1926 and 1928) developed a ratio between buoyancy and viscosity to characterize the effect of Rayleigh-Bénard convection with rigid-rigid and rigid-non-rigid boundary conditions (Koschmieder 1993). Pellew and Southwell (1940) provided the first review of Rayleigh-Bénard convection, explaining the mathematic principles behind the Rayleigh number and the theoretical aspects in detail, but the term "Rayleigh number" was actually first used by Sutton (1951). The hexagonal convective cell pattern observed by Bénard was not a direct result of buoyancy-induced convection, but rather surface tension gradients and Block (1956) was the first to make the distinction that Bénard's observations of the convection pattern were due to gradients in surface tension (Koschmieder 1993). Because the surface of the fluid was exposed to air, fluctuations in temperature along the surface of the heated fluid caused surface tension gradients. If the vertical cross-section of a hexagonal cell was observed, the horizontal convective rolls within the fluid could be seen. An experiment conducted by Kumar, Srinivasan, and Dutta (2006) visualized the convective loops due to Rayleigh-Bénard convection that took place during solidification by placing hollow glass beads into a liquid salt solution with the same density. The salt solution was allowed to solidify and the glass beads within the salt solution would scatter a laser beam directed at the solid.

In a monograph by Chandrasekhar (1961), a thorough review of Rayleigh-Bénard convection was provided. In it, he also described the effect of Rayleigh-Bénard convection with the influence of rotation by stirring using magnetic fields. This was reviewed by Koschmieder (1993) who also discussed supercritical and non-linear Rayleigh-Bénard convection and Rayleigh-Bénard convection in spheres. At the critical Rayleigh number, a fluid undergoes a transition from no convection to laminar convection stage. At a higher Rayleigh number, the fluid undergoes a second transition from laminar convection to turbulent convection. Oertel (1983) discussed the theoretical treatment of thermal instabilities in fluids and also provided a brief, but thorough review of Rayleigh-Bénard convection and the Bénard configuration. By using computation, Oertel was able to model the heat transport and velocity profiles that appeared in three-dimensional Rayleigh-Bénard convection in a system where the Rayleigh number was $2.3\times10^5$. The articles by Chandrasekhar, Bérge and Dubois (1984), Koschmieder (1993), and more recently Manneville (2006) have provided detailed reviews of the development and principles of the Rayleigh-Bénard convection phenomenon and the derivation of the Rayleigh number. Rayleigh-Bénard convection continues to be a significant research topic in fields including: fluid dynamics, environmental science, and solidification (Bodenschatz et al. 2000).

## 3.2 Development of Marangoni Convection

Marangoni convection which is caused by fluctuations in surface tension due to lateral thermal gradients is another type of convection that is related to a liquid's interfacial properties. In Bénard's experiment where he used a thin film of fluid, Marangoni convection was present with Rayleigh-Bénard convection. The phenomenon, as well as the non-dimensional number, is named after the Italian physicist, Carlo Marangoni, for his observations in the late 19$^{th}$ century of what is now known as the "tears of wine" phenomenon (Koschmieder 1993). The first study of capillary-induced fluid convection was made by Pearson (1958) when he used the Navier-Stokes equation of thermal conduction and the continuity equation to analyze the mechanism of Marangoni convection in the same manner as Rayleigh-Bénard convection (Koschmieder 1993). Scriven and Sternling (1964) determined that during Bénard's experiment, there was an upflow of fluid from beneath the convective cell and the relationship between Marangoni and Rayleigh-Bénard convection was made by Nield (1964) when he considered the combined effect of gravity and surface tension on a fluid heated from below (Koschmieder 1993). Although convection could occur on the surface of and inside the fluid, the onset of convection is typically caused by one type of instability. The theory of linear, non-linear, subcritical, supercritical Marangoni convection was discussed by Koschmieder (1993), where he reviewed many of the Rayleigh-Bénard convection and Marangoni convection experiments conducted up to that point. In a microgravity environment, the effect of Rayleigh-Bénard convection would be lessened significantly, but surface tension gradients would enhance the effect of Marangoni convection. In the high-gravity experiments reported in this research, the effects of Rayleigh-Bénard convection would dominate over the effects of Marangoni convection.

## 3.3 Review of Solidification in Normal Gravity

Chalmers (1964) briefly discussed the effects of gravity on a liquid melt during solidification. He described an experiment conducted by Ruddle (1957) where an ingot was cast and then cut along its vertical cross-section to observe its microstructure. Ruddle observed that the ingot had large columnar grains at the top and smaller equiaxed grains at the bottom. During columnar solidification, the rejected solute would build up ahead of the solid-liquid interface so that the solute-enriched zone would become heavier than the bulk melt. Constitutional supercooling would cause the solute-enriched zone to nucleate and grow as equiaxed crystal. Because these crystals were heavier than the melt, the crystals would sink and continue to grow until they reached the bottom of the melt. Thus, the columnar grains at the top of the mould could continue to grow resulting in large columnar grains at the top of the mould and equiaxed grains at the bottom. Chalmers (1964) also referred to several experiments where the melt was solidified with vertical rotation by magnetic stirring. Because of the increased shear forces caused by rotation, the columnar zone of the ingot could be shortened

or even eliminated. In addition, any equiaxed nuclei that formed would move toward the mould wall and impinge the columnar zone resulting in a more uniform grain structure (Chalmers 1964).

Eutectic materials are another aspect of solidification that has been widely studied. Hunt and Jackson (1966) classified most metal eutectic alloys into three categories based on the entropies of melting for the component phases. When both phases have low entropies, growth is lamellar or rodlike and when both have high entropies, both phases grow as faceted crystals (Hunt and Jackson 1966). When one phase has a high entropy of melting and the second has a low entropy of melting, the structure can be irregular or "complex regular" (Hunt and Jackson 1966). They demonstrated that these types of eutectics formed in experiments on Sn-Cd, Al-Si, Zn-$Mg_2Zn_{11}$, Zn-$MgZn_2$, and Sn-Bi binary metal eutectics and carbon-tetrabromide-hexachloroethane, succinonitrile-borneol, cyclohexane-camphene, and azobenzene-benzil binary organic eutectics. Enhanced gravity has been shown to have an effect on the lamellar eutectic microstructure in terms of the phase ratio of the eutectic spacing (Chalmers 1964). In eutectics composed of phases with varying densities, there would be an increasing percentage of the heavier phase in the lamellar structure in the direction of gravity (Chalmers 1964). Chalmers refers to an experiment done by Allen and Isserow (1957) where they "cycled" a U-Al eutectic at its eutectic temperature. They found that at high centrifugal acceleration, there was a higher percentage of U at the bottom of the crucible than at the top.

In a detailed description of solidification and casting, using the equations and relationships between thermodynamics, heat flow, and solidification morphology, Flemings (1974) reviewed the criteria for stable solidification formulated by Rutter and Chalmers (1953), and expanded on it by discussing the influence of zero-convection and perfect convection in single- and polyphase alloys. Heat and mass transfer are influenced by the intensity and type of convective flows in the melt, and have a tendency to become unsteady at higher flow intensities causing temperature fluctuations at the solid-liquid interface that in turn create striations in the solidified crystal, which are detrimental to a semiconductor's properties (Flemings 1974). Müller (1983) explored natural convection during crystal growth from melts by considering the influence of gravity. He indicated that the driving forces for convective flows included density gradients, pressure gradients, and surface tension gradients. He also reviewed several prior experiments of low high-gravity crystal growth ($1.5g_0$ to $30g_0$) using the Bridgman technique and made several important observations. Depending on the level of gravitational acceleration, buoyancy-induced thermal convection in a melt alternated from steady-state to unsteady-state, and back to steady-state. Unsteady convection created inhomogeneous crystals, primarily doping striations, which were attributed to temperature fluctuations in the melt. When conditions exceeded the second critical Rayleigh number, $Ra_{C2}$, convection became unsteady and when the conditions exceeded the third critical Rayleigh number, $Ra_{C3}$, convection reverted back to steady-state, which was termed

"relaminarization." The values of $Ra_{C2}$ and $Ra_{C3}$ were dependent on the aspect ratio of the container. It was concluded that convection could be manipulated to grow striation-free crystals, which would have better semiconductor properties (Müller 1983).

Another effect of convective instabilities is the breaking of dendrite arms during solidification. These fragments are transported away from the solid-liquid interface into the melt while continuing to grow and hence create the equiaxed zone. McCay et al. (1989) discussed the convective instabilities during directional solidification and the pluming of light fluid and freckling of dendrite arms. They used ammonium chloride and water as their model of solidification and correlated freckling to the Rayleigh number. The variation in density between solid and liquid phases could also cause buoyancy-driven fluid flow. When a dendrite forms in a melt, it either floats or sinks, depending on the density difference, and displaces fluid along its path transporting heat along the solid-liquid interface of the dendrite away resulting in increased growth rate (McCay et al. 1989). If the dendrite sinks, fluid flow would be greatest at the bottom of the dendrite and slowest at the top which would result in a faster growth rate at the bottom of the dendrite than at the top. Conversely if the dendrite floats, then fluid flow and heat transport would be greatest at the top of the dendrite and lowest at the bottom resulting in faster growth rate at the top than the bottom. This has been called forced convection for which a model has been developed by Schrage (1999). He simplified the model by studying crystal growth at the dendrite tip, constraining the dendrite to a fixed point in space, and eliminating buoyancy-induced convection. In addition, Zhao, Heinrich, and Poirier (2004) provided a more complex model of this effect by also taking into consideration factors such as solidification shrinkage and thermal and solute buoyancy effects. The phenomena seen in many types of solidification processes can be attributed to Rayleigh-Bénard or natural convection. These effects can be minimized or removed in a microgravity environment, but other effects that are masked due to gravity arise, and these effects been studied.

## 3.4 Review of Solidification in Microgravity

Since the 1950's, more advanced experiments have been conducted to observe the behaviour of materials in microgravity conditions. There have been numerous experiments that compare solidification in microgravity with normal gravity. Here, a brief review of the literature on solidification under microgravity that is relevant to this research is given. Initial studies on solidification in simulated microgravity conditions were conducted using droptowers (Feuerbacher, 1986). Droptowers are still used; the NASA-Marshall Space Flight Center has a drop tower 100 m tall to study physical phenomenon in a microgravity of $10^{-4}g_0$ sustained for 4.6 s (Naumann 1986 and Hamacher et al. 1987). Sounding rockets, where a rocket is launched into the upper atmosphere and allowed to free-fall, were used to produce microgravity conditions for up to 15 min (Feuerbacher, 1986). The Space Processing Applications Rocket (SPAR)

Program was developed by NASA and similar rocket programs have also been developed by the European and Japanese space agencies. Using the SPAR program, Johnston and Griner (1977) studied solidification of $NH_4Cl$ dendrites in water at $10^{-5}g_0$ and compared the results to $1g_0$ to study the influence of gravity on dendrite growth and the columnar-equiaxed transition during casting. They observed that in normal gravity, dendrite fragments were swept into the center of the melt creating the equiaxed zone, but in microgravity, no such fragmentation occurred and the entire casting consisted of only columnar grains. They concluded that the columnar-equiaxed transition was caused by gravity and its effect on fluid flow. Also, dendrite growth in microgravity was slower because there was no fluid flow transporting solute to and heat away from the solid-liquid interface, thereby making solidification kinetics to become diffusion-controlled (Johnston and Griner 1977).

Materials processing in microgravity possess several benefits: containerless processing reduce container interaction and hydrostatic pressure and the reduction and elimination of natural convective flows and sedimentation effects (Carruthers 1977). Carruthers (1977) discussed these advantages with respect to crystal growth in a low gravity environment and examined prior experiments performed in microgravity using methods such as the SPAR program, Apollo-Soyuz, and Skylab projects. Curruthers and Testardi (1983) provided a more in-depth discussion of materials processing in space where they explained the principles of solidification in microgravity and the phenomenon of Rayleigh-Bénard convection and reviewed many solidification experiments conducted in space up to that time. They also discussed solidification processes including dendritic growth, single crystal growth, and casting, and the effect of microgravity on these processes. It was concluded that materials processing in microgravity could have added benefits for crystal growth, but problems due to lack of understanding of the phenomena in microgravity persisted (Carruthers 1977 and Carruthers and Testardi 1983).

The development of the KC-135 aircraft allowed astronauts to experience weightlessness and scientist to and conduct microgravity experiments without having to go into space. The aircraft takes a parabolic flight path that simulates gravity levels from $10^{-2}g_0$ to $2g_0$, depending on the plane's position and trajectory (Owen 1987). Although, microgravity could be simulated for up to 30 s, the flight path could be repeated several times. Grugel (1989) explained the issues of dendritic growth during the transient stage of a parabolic flight path and indicated that the transient stage from normal to microgravity and vice versa showed different dendritic properties from microgravity steady-state. The development of the space shuttles and the International Space Station provided additional environments where scientists could have experiments conducted in a continuous microgravity environment. Experiments have been performed in microgravity in all areas of materials science including crystal growth, mass and heat transport, fluid dynamics, and containerless processing technology (Feuerbacher 1986).

More recently, interest has focused on materials processing in space, particularly for growing large, defect-free single crystals for electronic devices.

One phenomenon in microgravity materials processing that is widely studied is fluid convection in melts because lack of the buoyancy effect would enhance the effect of Marangoni convection. Schwabe and Scharmann (1988) explored the effects of Marangoni and Rayleigh-Bénard convection by using tetracosane ($H(CH_2)_{24}H$) in an open cavity container to visualize the convective loops during heating in both microgravity and normal gravity. Curreri and Stefanescu (1988) discussed the low-gravity effects on convection in planar, cellular, dendritic, and eutectic solidification. They indicated that natural convection during solidification is caused by both the solute density and thermal density gradients causing convection, the degree of which was determined by using the Prandtl number.

A significant low-gravity dendritic solidification experiment was conducted onboard the Columbia space shuttle in 1994 in a project known as the Inter-Dendritic Growth Experiment (IDGE) (Glicksman et al. 1995). The objective of IDGE was to study the growth of succinonitrile dendrites without the influence of natural convection. Glicksman et al. (1995) used succinonitrile as their model to study dendritic growth under microgravity and terrestrial gravity in terms of growth velocity and tip radius in supercooled melts. The values obtained in microgravity were compared with the results obtained in terrestrial gravity. They concluded that convection altered the relationship between the two values at low supercoolings up to 1.7 K. The Ivantsov theory for dendritic solidification (Ivantsov 1947) failed under terrestrial gravity, but held better for microgravity conditions due to a purely diffusive mode of heat transfer. The results of IDGE were also analyzed by Mack and Tensi (2000). They stated that the isothermal growth of dendrites in a supercooled melt is controlled by heat flux only and that the relationship between $r^2R=const.$ (where $r$ is radius of curvature and $R$ is velocity of the dendrite tip) held under both terrestrial and microgravity conditions.

One detrimental effect of solidification in microgravity is bubble formation. On Earth, bubbles that form due to solidification shrinkage, float and escape in the atmosphere. In space, lack of buoyancy causes the bubbles to remain relatively motionless in the melt. Grugel and Anilkumar (2004) also performed experiments using succinonitrile and injecting nitrogen into the melt during directional solidification to study the bubble motion in microgravity. In summary, solidification in microgravity has many benefits to solidification processing and materials science, but at the same time there are also detrimental effects on microstructure.

### 3.5 Review of Solidification in High-Gravity

Solidification experiments have been performed under centrifugal acceeleration to study the effects of high-gravitational fields on microstructure development and solidification morphology. The types of solidification studied

under high-gravity have included directional solidification of dendrites, eutectic growth, and single crystal growth using the Bridgman and floating zone methods. Müller, Schmidt, and Kyr (1980) studied the effects of high-gravitational fields on single-crystal growth by studying density-driven convection in melts of In and InSb and crystal growth of InSb. The onset of unsteady convection in melts was studied under accelerations equivalent to $1g_0$ to $20g_0$ and the study of increased hydrostatic pressure of the crystal growth was conducted in accelerations of $1g_0$ to $3g_0$. In their experiments, crystal growth was performed using the Bridgman technique while under centrifugal acceleration where the thermal gradient was parallel and 'antiparallel' to the direction of gravity. In a parallel configuration, the direction of centrifugal acceleration is parallel with the thermal gradient so that the temperature would *increase* with the direction of gravity. In an anti-parallel configuration, the thermal gradient is in the opposing direction of centrifugal acceleration so that the temperature would *decrease* with increasing centrifugal acceleration. It was concluded that the doping striations that occur in crystal growth could be explained by defining the Rayleigh number with a variable acceleration term, instead of a constant one (Müller et al. 1980).

High-gravity directional solidification experiments were first conducted by Johnston and Parr (1982). They studied dendritic growth and grain structure using Sn- 15 wt% Pb in both microgravity and high-gravity ranging from $10^{-4}g_0$ to $5g_0$ under three different cooling rates. The study was unique because dendritic growth in microgravity was compared with high-gravity instead of normal gravity. There was evidence of dendrite fragmentation in the high-gravity casting which were transported to the bottom of the crucible because of the enhanced gravity. The high-gravity castings exhibited a finer grain structure whereas the microgravity castings had larger grains and larger and more uniform dendrite arm spacing. They concluded that on a macroscopic scale, high-gravity would drive fluid flow and cause dendrite re-melting, fragmentation, and macrosegregation. Also, by changing the cooling rate, factors such as dendrite arm spacing and permeability to fluid flow would be affected, but the relationship to cooling rate to dendrite arm spacing deviated from the hypothesis. They attributed this to a lack of convection within the spacing between the dendrite arms, which allowed the dendrites to coarsen more slowly and uniformly.

Regel (1987) provided a detailed review and summary of many of the solidification and crystal growth experiments conducted in high-gravity simulated by centrifugal acceleration and discussed the effects of high-gravity on the segregation phenomenon during crystal growth. He suggested that when sedimentation occurs, the onset of convection would not only depend on the Rayleigh and Grashof numbers, but also on the initial solute concentrations of the melt. Regel discussed the effect of high-gravity on temperature oscillations and the segregation of impurities through the Bridgman method. Certain levels of centrifugal acceleration could result in the stabilization of convective flow and actually simulate weightlessness (Regel 1987). The influence of the Nusselt number, $Nu$, which describes the ratio between total heat flux and heat flux by

thermal conductivity, was discussed. If there is no convective flow within the melt ($Nu=1$), heat transfer would be by conduction only, but if there is convective flow ($Nu>1$), heat transfer would be by convection and conduction (Regel 1987). Regel concluded that centrifugal acceleration would amplify the effect of buoyancy and the convective flow resulting in the Nusselt number becoming greater than one in a parallel configuration.

Müller (1990) compared crystal growth under reduced and enhanced gravity. He indicated that the magnitude of gravity affected the solidified crystal by increasing the mechanical stress caused by its own weight, which could lead to increased strain fields, dislocations, and twinning. Furthermore, gravity would affect the solid-liquid interface by creating interface instabilities which would cause constitutional supercooling leading to the formation of grain boundaries and voids (Müller 1990). Most of the effects of gravity occur in the melt during solidification where factors such as sedimentation, buoyancy-induced convection, and hydrostatic pressure could cause crystal imperfections (Müller 1990). Müller listed a set of experiments previously performed in both reduced gravity and enhanced gravity conditions and concluded that a variation in gravity could provide the crystal grower with an extra degree of freedom to improve the quality of crystals. However, it could not be concluded that reduced gravity or enhanced gravity would be beneficial for all types of crystal growth (Müller 1990).

The benefits of crystal growth and materials processing in high-gravity were reviewed by Shlichta (1992). Shlichta reviewed experiments that were conducted in high-gravity from $1000g_0$ up to $600{,}000g_0$ and discussed potential commercial applications of high-gravity processing and the problems associated with them. In addition to single-crystal growth, high-gravity processing could be utilized for metals, ceramics, and polymers (Shlichta 1992). Some of the more notable advantages to high-gravity processing include the production of inclusion-free optical crystals, elimination of microvoids from slip castings, concentration of sol-gels, and production of compositionally-graded materials (Slichta 1992). Shlichta concluded that gravity should be seen as a variable rather than a constant, and that high-gravity processing still had unexplored avenues that could be studied.

Sokolowski and Glicksman (1983) explored the effects of high-gravity on eutectic solidification. They studied the Pb-Sn eutectic and Al- 50 wt% In melts centrifuged for 50 hours at high temperature while in a melt and quenched. The results at centrifugal acceleration equivalent to $120{,}000g_0$ were compared with the experiment done without centrifugal acceleration. They initially concluded that high-gravity did not cause segregation in the Pb-Sn eutectic alloys. However, later Glicksman and Sokolowski (1992) examined Pb-Sn alloys under a centrifugal acceleration of $100{,}000g_0$, and studied the solidification process by varying the compositions, rotational rates, and cooling rates. Their centrifuge device was air driven which could cast cylindrical Pb-Sn ingots 6.5 mm in length and 3.0 mm in diameter, inside a borosilicate glass container. Their results showed that at sufficient levels of high-gravity and slow cooling rates, the

components of the eutectic would seperate. As a result, there were two different primary phases on either ends of the ingot and a eutectic phase in the middle. They attributed the macrosegregation of the phases to two factors: convective mass transfer from particles that sediment and reject solute and free convection of starting plumes of buoyant fluid originating in the solute diffusion boundary layer. They concluded that primary and secondary dendrite arm spacing, as well as interphase lamellar spacing did not change significantly with high-gravity. However, when holding the temperature between the liquidus and solidus temperatures, they attained areas of fine dendrites, coarse dendrites, followed by eutectic, and finally dendrites of the opposite component.

There is also evidence to suggest that sufficient high-gravitational fields can affect the diffusion of atoms during solid-state. Mashimo (2001) used a "mega-gravity" field of over $10^6 g_0$ in which he examined the sedimentation of atoms in a Bi-Sb alloy. It should be noted that $10^6 g_0$ would be the equivalent to the gravitational field produced by a degenerate star (Mashimo 2001). The equipment developed by Mashimo was able to sustain a mega-gravitational field at temperatures of several hundred degrees Celsius for several days. In his experiment, Mashimo centrifuged Bi-Sb (70:30 mol%) at $10^6 g_0$ for 85 hours. He observed that there was a segregation of the Bi from the Sb and attributed it to the mega-gravity providing an adequate force to overcome atomic attraction. He concluded that the mega-gravity could be used to form an atomic-level graded structure in many materials.

Solidification studies at much lower levels of high-gravity were conducted by Zhao et al. (1996 and 1998). They studied the effects of high-gravity on the microstructure of Pb-Sn eutectic alloy by using the Bridgman technique to solidify the melt under centrifugal acceleration. They were able to study the effects at four different levels of gravity, based on different radii at $1g_0$, $5g_0$, $10g_0$, and $15g_0$. The results indicated that eutectic cell size in high-gravity was smaller than in normal gravity. It was shown that the cell size changed from about 29 μm in $1g_0$ up to 15 μm in $15g_0$. However, there was only 'partial' difference in eutectic spacing between normal and high-gravity, which led them to conclude that buoyancy convection did not influence solute exchange between the eutectic phases. However, they also stated that at $1g_0$ and $15g_0$, eutectic spacing was regular lamellar (Zhao et al. 1998). For $5g_0$ and $10g_0$, the morphology changed to cell-dendritic. They attributed this to the difference perturbation character of buoyancy under different magnitudes of gravity. If convection takes place, the momentum of the convection in high-gravity would have carried-over to the low-gravity areas (Zhao et al. 1998).

Battaile et al. (1994) studied dendritic solidification by directionally solidifying lead dendrites in a Pb-Sn eutectic in simulated high-gravity ranging from $1g_0$ to $15.3g_0$. The results were quantified in terms of primary and secondary dendrite arm spacing, eutectic spacing, and primary dendrite trunk diameter. It was indicated that there was no change in eutectic spacing, primary dendrite trunk diameter, or secondary dendrite arm spacing with respect to gravity

level. However, there was a decreasing trend of primary dendrite arm spacing with increasing gravity. This trend was attributed this to the increase in convection suppressing solute diffusion and/or enhanced buoyancy of the solute-rich liquid. They did not discuss the extent to which convection has an effect on solidification and did not indicate how the temperature gradient developed or the growth velocity changed.

# CHAPTER 4: EQUIPMENT AND PROCEDURE

## 4.1 Materials

Succinonitrile ($C_2H_4(CN)_2$) was purchased from Sigma-Aldrich Canada Ltd. According to the label, its purity was 99 wt%. Succinonitrile has a melting temperature of 58°C, a density of 0.985 g/cm$^3$, and a body-centered cubic crystal structure with a unit cell size of 0.637 nm. Granulated, commercially-pure Sn was also purchased from Sigma-Aldrich Canada Ltd. The average size of the granules was 4 mm and according to the label, its purity was 99.85 wt% containing 0.15 wt% of Bi, Cu, Fe, Pb, and Sb, each with a concentration between 0.01 wt% and 0.05 wt%. Shot pellets of Bi were also purchased from Sigma-Aldrich Canada Ltd. According to the label, its purity was 99.9 wt%, but the impurity composition was not indicated. The Bi-Sn alloys were produced by melting the component metals in specified proportions into a container and stirring the melt. Table 4.1 provides a list of the density, crystal structure, heat of fusion and heat capacity for Bi, β-Sn, and the Bi-Sn eutectic.

Table 4.1: Material properties of Bi, β-Sn, and Bi-Sn eutectic

| | **Bi** | **β-Sn** | **Bi-Sn eutectic** |
|---|---|---|---|
| **Melting Temperature** | 273°C | 232°C | 138°C |
| **Solid Density** | 9.78 g/cm$^3$ | 7.27 g/cm$^3$ | 8.55 g/cm$^3$ |
| **Liquid Density** | 10.05 g/cm$^3$ | 6.99 g/cm$^3$ | 8.49 g/cm$^3$ |
| **Crystal Structure** | rhombohedral | body-centered tetragonal | lamellar mix of rhombohedral and tetragonal |
| **Latent Heat of Solidification** | 54.1 J/g | 59.2 J/g | 46.5 J/g |
| **Heat Capacity** | 0.122 J/(g·K) | 0.228 J/(g·K) | 0.188 J/(g·K) |

In order to produce the $Sn_{99.7}Cu_{0.3}$ alloy, a copper pipe, commonly used for household plumbing applications, was introduced into the Sn melt. Even though the copper pipe remained solid, Cu atoms were able to diffuse into the Sn melt. The use of the pipe was eventually discontinued, but the Sn had still been contaminated with Cu. Depending on the material, the specimens were either cold mounted in epoxy resin or hot-mounted in Lucite. The Lucite powder was manufactured by Struers Corporation and the epoxy resin was purchased from Metlab Corporation.

## 4.2 Experimental Apparatus

The equipment for this experiment was designed specifically to sustain or withstand high-gravitational fields simulated by spinning the test sample thereby producing centrifugal acceleration. The experiment consisted of seven pieces of equipment: the chamber, container, buffer, capsule, centrifuge assembly, and two resistance furnaces: one for sample preparation and another for the actual experiment. A metric caliper, accurate to within ±0.0025 mm, was used to

measure the dimensions of the smaller components. The dimensions of the larger pieces of equipment were measured with measuring tape, accurate to ±0.25 cm.

4.2.1 The Chamber

The purpose of the chamber was to secure the container that held the melt during spinning. Figure 4.1 shows a photograph of the chamber.

Figure 4.1: Photograph of the chamber

The chamber was a cylindrical cup made of an aluminum alloy. It had an outer diameter of 56.1 mm, an inner diameter of 52.1 mm, a wall thickness of 2.2 mm, and a height of 102.7 mm. Threads were machined at the top end of the chamber so that it could be easily screwed onto and off of a threaded flange that was connected to the centrifuge assembly. During cooling, a digital infrared thermometer was used to measure the surface temperature of the chamber. However, because the infrared thermometer was set with a fixed emissivity, the reflective surface of chamber caused inaccurate temperature readings. Therefore, the surface of the chamber was painted with fireproof black paint so that temperature could be measured more accurately. The chamber was originally designed to hold a special glass container that held a liquid during solidification while it was spinning. In order to secure the glass container from lateral vibration during spinning, a chamber cap was placed inside the chamber on top of the glass container. The chamber cap had a diameter of 52.0 mm and a thickness of 5.5 mm. Figure 4.2 shows a photograph of the chamber cap.


Figure 4.2: Photograph of chamber cap

The purpose of the glass container was to hold materials such as water or succinonitrile during solidification and examine its crystal structure. Because metals are opaque, the microstructure could not be examined this way. In order to examine the microstructures of the solidified samples, the glass container needed to be broken each time after each use. This was not a feasible option, so disposable metal containers were used to hold the melt instead.

4.2.2 Melt Container and Buffer

Small cylindrical containers and lids made of tin-plated steel were used to hold the melt during solidification. These containers were purchased in bulk from a U.S. company. Figure 4.3 shows a photograph of a container and the lid.


Figure 4.3: Photograph of tin-coated steel container

The container had an inner diameter of 37.9 mm, a height of 12.9 mm, and a wall thickness of 0.8 mm. The tight-fitting lid had an outer diameter of 39.6 mm and a height of 7.0 mm. The container would be filled with the test material and hermetically sealed with the lid using silicone adhesive. During spinning, the container would move to the edge of the chamber because of the difference in diameters of the container and the chamber. Therefore, to secure the container in the center of the chamber during spinning, a buffer component was designed and machined specifically to hold the container in place. Figure 4.4 shows a photograph of the buffer component.


Figure 4.4: Photograph of buffer component

The buffer was cylindrical in shape and was made from an aluminum alloy. It had an outer diameter of 51.4 mm, an original inner diameter of 29.3 mm, and a height of 40.1 mm. Using a metal lathe, the inner radius of the buffer was machined so it conformed to the irregular shape of the container. The container was placed in the buffer which was placed in the chamber eliminating any lateral movement of the container.

While the components were spun to generate centrifugal acceleration, the pressure of the melt against the container wall increased. As this increase in pressure could break the silicone seal, a second aluminum cylinder was placed on top of the buffer to act as a weight in order to further secure the lid to the container. The weight had an outer diameter of 50.9 mm and a height of 40.9 mm. The chamber cap was placed on top of the weight to ensure that the container, buffer, and weight stayed in place during spinning. An illustration of the container, buffer, and weight, in the chamber is shown in Figure 4.5.

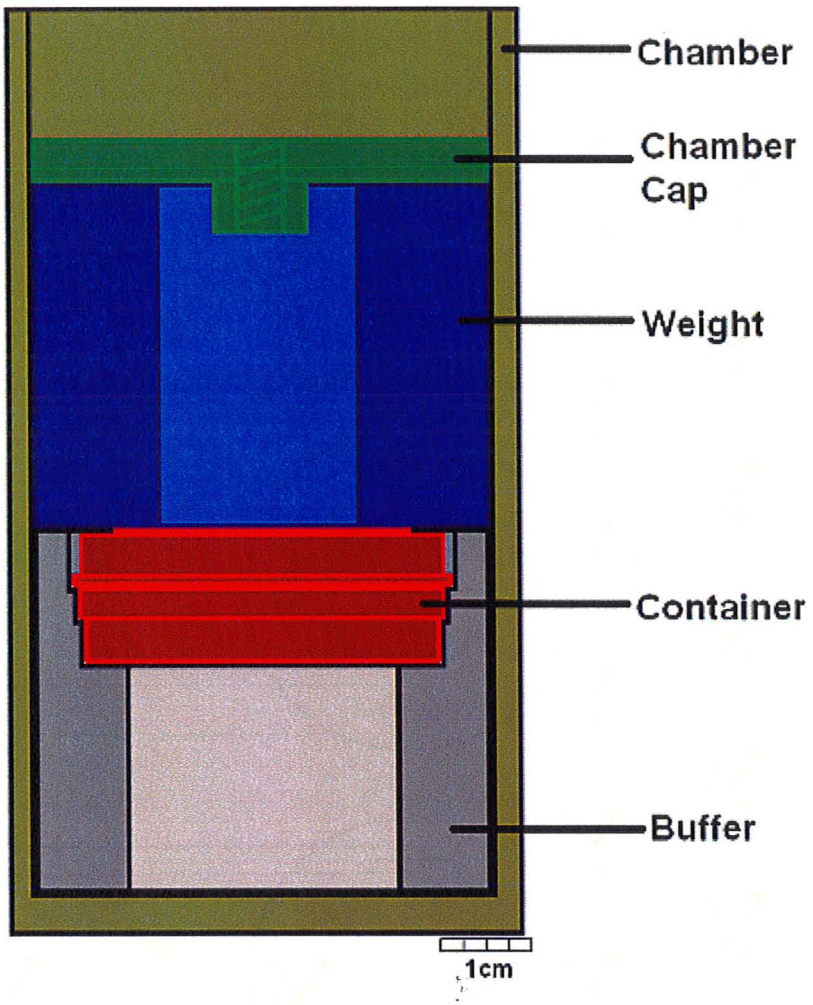


Figure 4.5: An illustration of chamber (brown), chamber cap (green), buffer (grey), weight (blue), and the container (red)

When the material for study was changed from succinonitrile and Bi-Sn alloy to Sn and Sn-Cu alloy, higher temperatures were required to melt the samples. Because the container was sealed with silicone adhesive, the experiment could only be conducted at temperatures below 200°C. Higher temperatures caused the silicone adhesive to break down resulting in the melt escaping from the container. Therefore, a capsule was specifically designed and machined to replace the container and buffer for the higher melting metals.

### 4.2.3 The Capsule

The capsule was a custom-made, cylindrical aluminum container used to hold the metal samples during melting and re-solidification. The capsule was a three-disc system used in lieu of the original tin-coated steel containers and buffer

to conduct experiments on metals with higher melting temperatures. Figure 4.6 shows a schematic diagram of the three discs of the capsule.

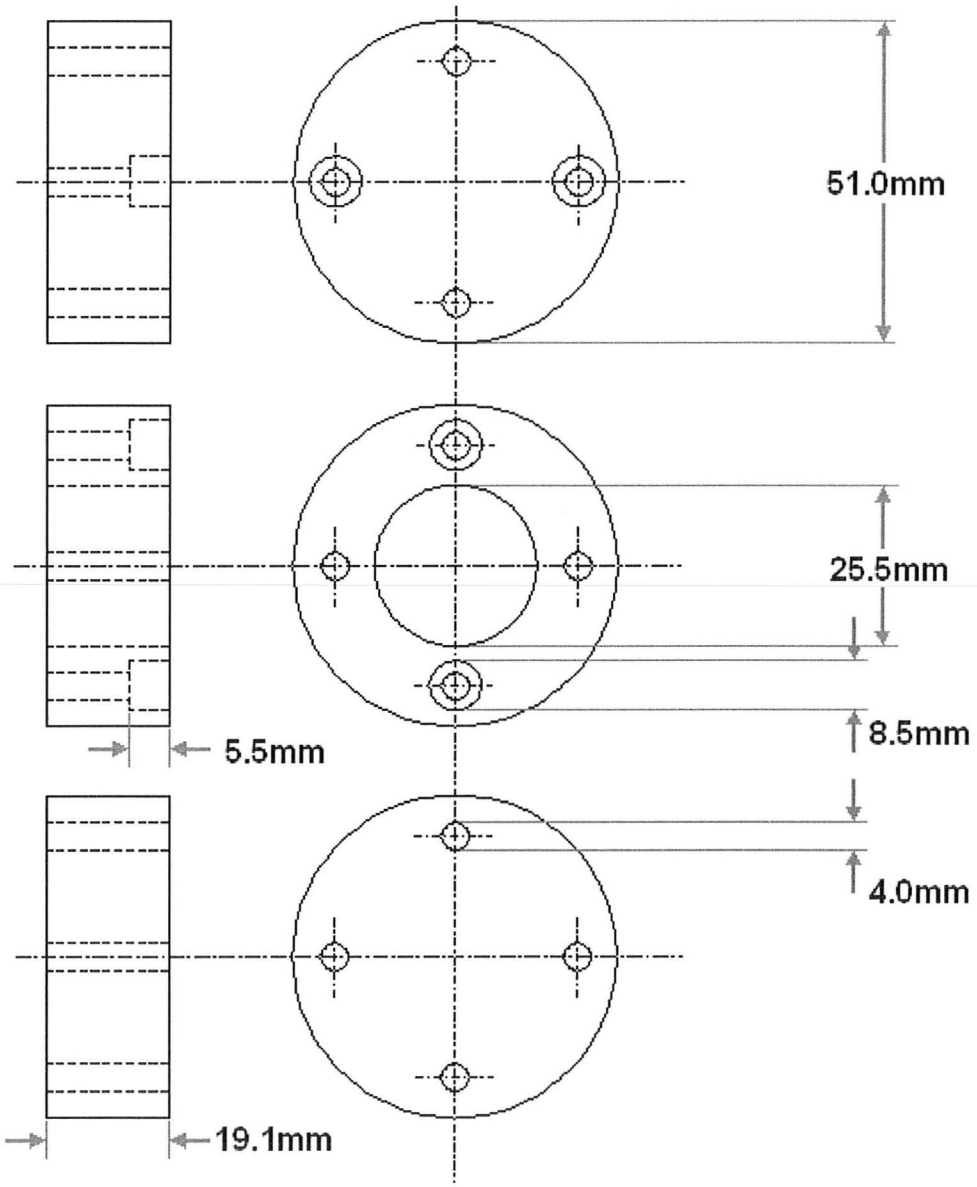


Figure 4.6: Schematic diagram of capsule discs

The three discs were each 50.9 mm in outer diameter and 19.1 mm in height. The middle disc had a 25.5 mm diameter hole drilled through its center which acted as a container for the metal during its melting and re-solidification. Each disc had four smaller holes drilled near its outer radius. The holes of all the discs were aligned together and threaded so that the discs could be fastened to each other using steel machine screws. Two screws attached the middle disc to the bottom disc and two additional screws attached the top disc to the middle disc, making the three discs one unit. To avoid leakage of the melt during spinning, the contact

surfaces of all three discs were grinded and polished flat to a near-mirror finish. This made the capsule virtually leak-proof, foregoing the need for a high-temperature gasket. A fourth disc was designed and machined to help determine the solidification conditions of the samples. Holes were drilled through the disc so that thermocouples could be placed inside the melt during cooling and solidification. Figure 4.7 shows a schematic diagram of the fourth disc and the placement of the thermocouples.

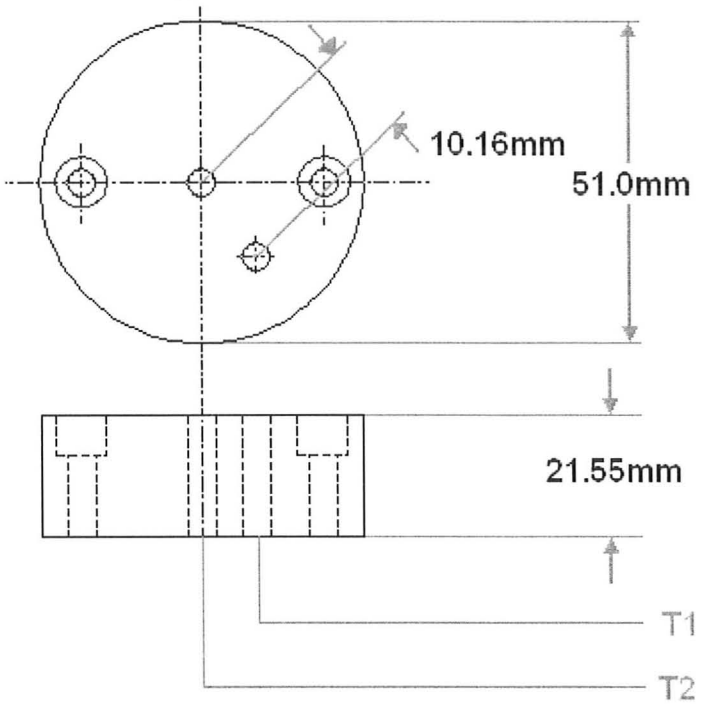


Figure 4.7: Schematic diagram of fourth capsule disc and thermocouple placement (T1, T2)

The fourth disc was made of the same aluminum alloy as the other three discs. It was 50.9 mm in diameter and 21.6 mm in height. Two holes were drilled through the disc along its outer radius to line up with the threaded holes of the middle disc so that they could be secured together with machine screws. Two additional holes, both with diameters of 3.8 mm, were drilled through the disc. The first hole was drilled in the exact center of the disc and the second hole was 10.2 mm away from the first hole. These holes would be above the cavity of the middle disc so that two thermocouples could be inserted into the melt to measure the temperature during a trial run. Two temperature-time graphs could then be used to determine the cooling rate, the velocity of the solid-liquid interface, and any unstable thermal gradients. The trial run conducted to measure temperature could only be done in static conditions without the influence of centrifugal acceleration. However, the results could be used to estimate the values of the needed quantities in during spinning conditions.

### 4.2.4 The Centrifuge Assembly for Axial Spinning and the Furnace

Centrifuges are devices typically used to separate materials of different densities or suspended particles from fluids. Although the device used in this research induced centrifugal acceleration, it did not have the same design as a typical medical centrifuge. Instead, it was designed to spin a cylindrical chamber holding a material along its cylindrical axis to simulate the effects of a high-gravitational field. For convenience here, the device used to generate centrifugal acceleration by spinning a melt along its center axis shall be referred to as the "centrifuge assembly." The centrifuge assembly was built by a technician associated with this group. The assembly was mounted on a steel frame and consisted of the motor, shaft, chamber, variable autotransformer, furnace, and its temperature regulator. Figure 4.8 shows a photograph of the centrifuge assembly and the furnace.

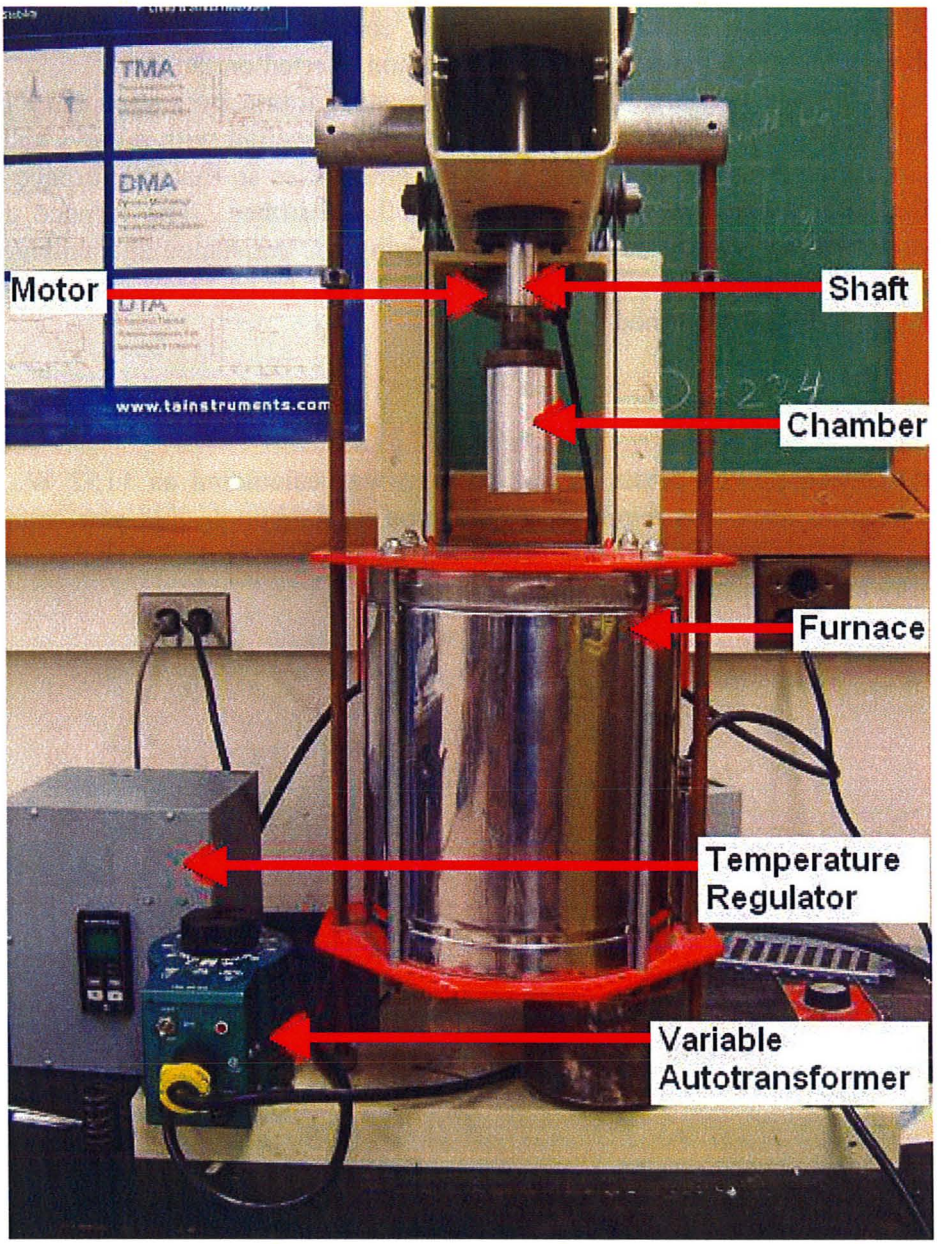


Figure 4.8: Photograph of centrifuge assembly, furnace, variable autotransformer, and temperature regulator

The entire assembly was placed on top of a sturdy wood table. The electrical motor of the assembly was attached to the frame and connected to an aluminum shaft by two pulleys and a rubber belt. The shaft was 260 mm in height and 25.0 mm in diameter. To reduce friction and vibration of the shaft during spinning, two steel bearing boxes were attached to the steel frame and held the shaft in place. The end of the shaft was connected to a threaded steel flange where the chamber was attached. The electrical motor was powered by a 120 V AC power source and its voltage was regulated by a variable autotransformer with a 10 A

fuse. The variable autotransformer would control the spinning speed of the chamber and thereby the centrifugal acceleration exerted on the melt.

A furnace was also connected to the steel frame by a secondary pulley system. The furnace was attached to a steel counterweight with pulleys and steel wires and its movement was guided by two steel poles so that the furnace could be lifted and lowered to surround and heat the chamber. The furnace used a resistance wire of 12.5 Ω for heating. Knowing the resistance and voltage, and using the equations for current [A] and power [W] listed below, the maximum power output was determined.

$$I = \frac{V}{R} \tag{4.1}$$

$$P = V \cdot I \tag{4.2}$$

The maximum power output of the furnace was calculated as 1152 W. The furnace temperature was regulated by a k-type thermocouple that was connected to a temperature regulator. Figure 4.9 shows an illustration of the centrifuge assembly and the furnace.

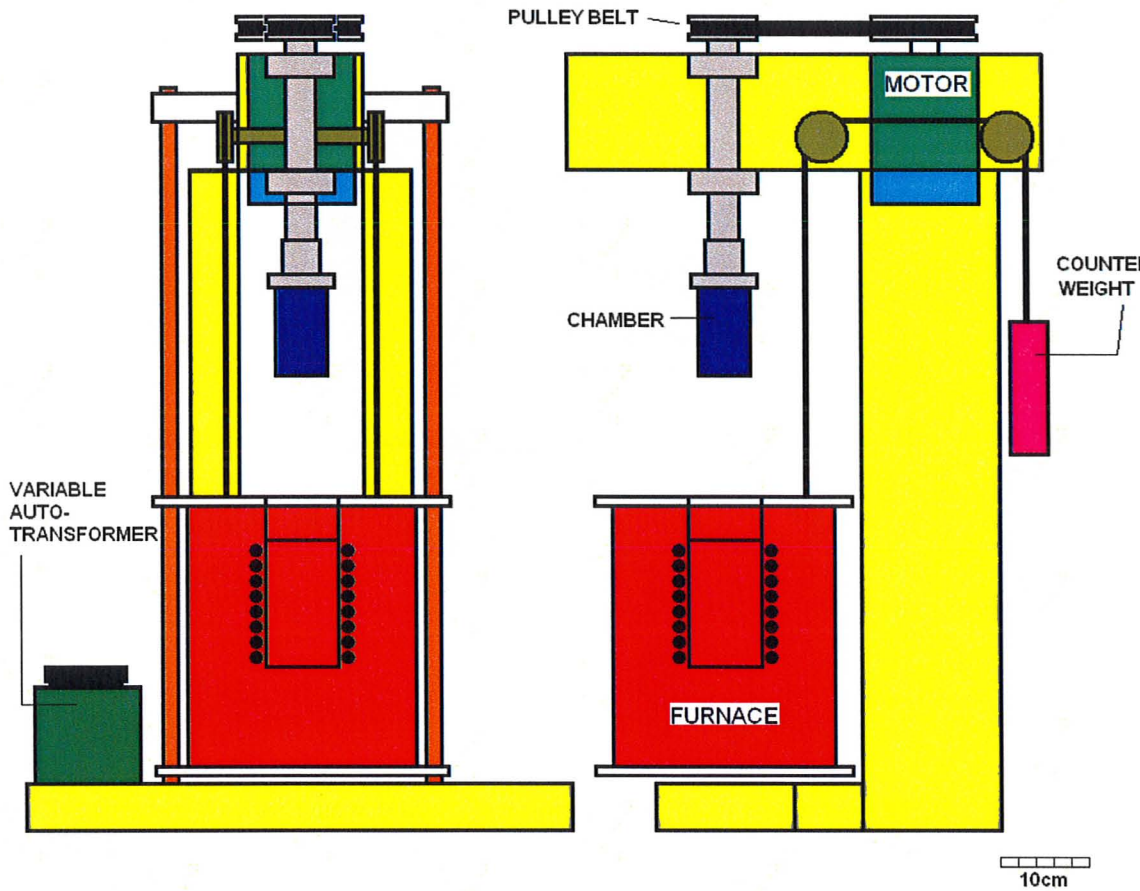


Figure 4.9: Illustration of furnace (red) and centrifuge assembly: frame (yellow), motor (light green), variable autotransformer (dark green), shaft (grey), chamber (blue), and counterweight (purple)

### 4.2.5 The Air-Shield

During solidification, the transport of heat away from the chamber's surface was caused primarily by convection. The high-gravitational field on the sample was produced by spinning the sample chamber at 4500 rpm. As a result, there was more air circulation at the chamber surface during the spinning condition than in the stationary condition. The increase in air circulation could have increased the cooling rate in the melt thereby affecting the microstructure formed on solidification. In order to make the cooling rate between the experiments with spinning the same as those conducted without spinning, an air-shield was made to limit the air circulation and heat exchange on the chamber surface. Figure 4.10 shows a photograph of the air-shield.

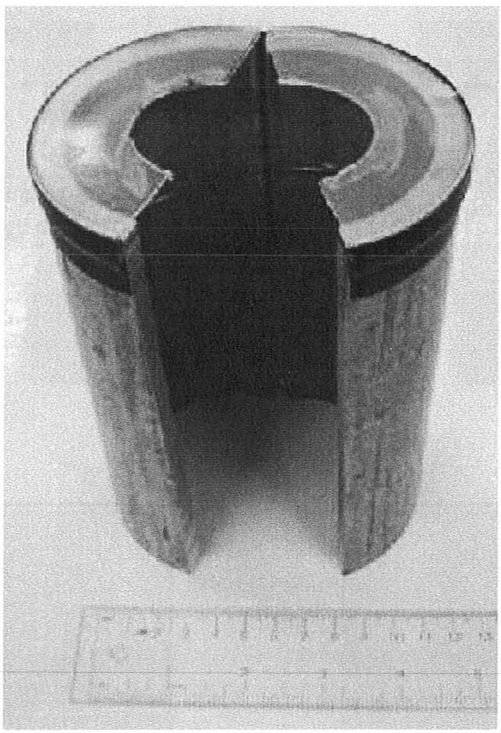

Figure 4.10: Photograph of air-shield

The air-shield was made from an aluminum pipe and was 158 mm in height, 87.6 mm in outer diameter, and 7.6 mm in wall thickness. The pipe was cut in half with a band saw and joined together at one edge with aluminum duct tape so that the air-shield could be opened and closed around the chamber while it was spinning. A circular plastic lid with the same outer diameter of the air-shield covered the top of the shield so that air could not escape through the top. A hole with a diameter slightly larger than the shaft of the centrifuge assembly was cut out of the center of the plastic lid to accommodate the flange and the shaft connected to the chamber. The lid was also cut in half so that the air shield could open and close without removing it completely.

During the experiment, the furnace was lowered and the opening of the furnace was covered with an insulating brick sandwiched between a steel plate and an aluminum plate. The air-shield was placed on top of the aluminum plate and around the chamber thereby reducing the air flow during the operation of the centrifuge assembly. A clamp was used to keep the air-shield closed. The rate of heat removal from the surface of the chamber under stationary and spinning conditions could then be assumed to be relatively equal. Figure 4.11 shows an illustration of the vertical section of the air-shield and its placement around the chamber.

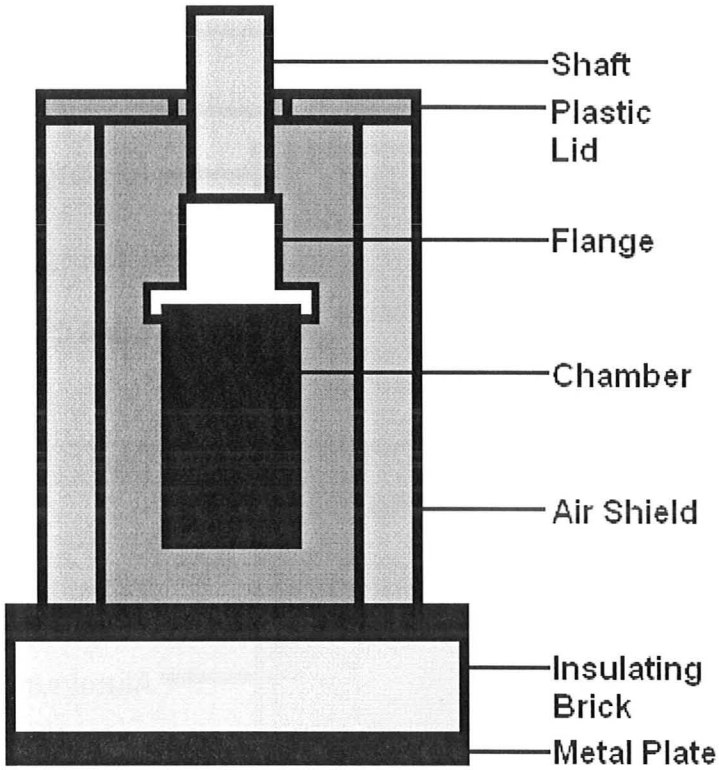


Figure 4.11: An illustration of vertical section of the air-shield

4.2.6 Furnace for Sample Preparation

Because the Sn was initially in granulated form, filling the container or capsule cavity and immediately performing the experiment was likely to have unwanted air pockets. Therefore, the granules of Sn were melted in the container in a second furnace so that more pellets could be added to minimize empty space. Figure 4.12 shows an illustration of the vertical section of the furnace used for sample preparation.

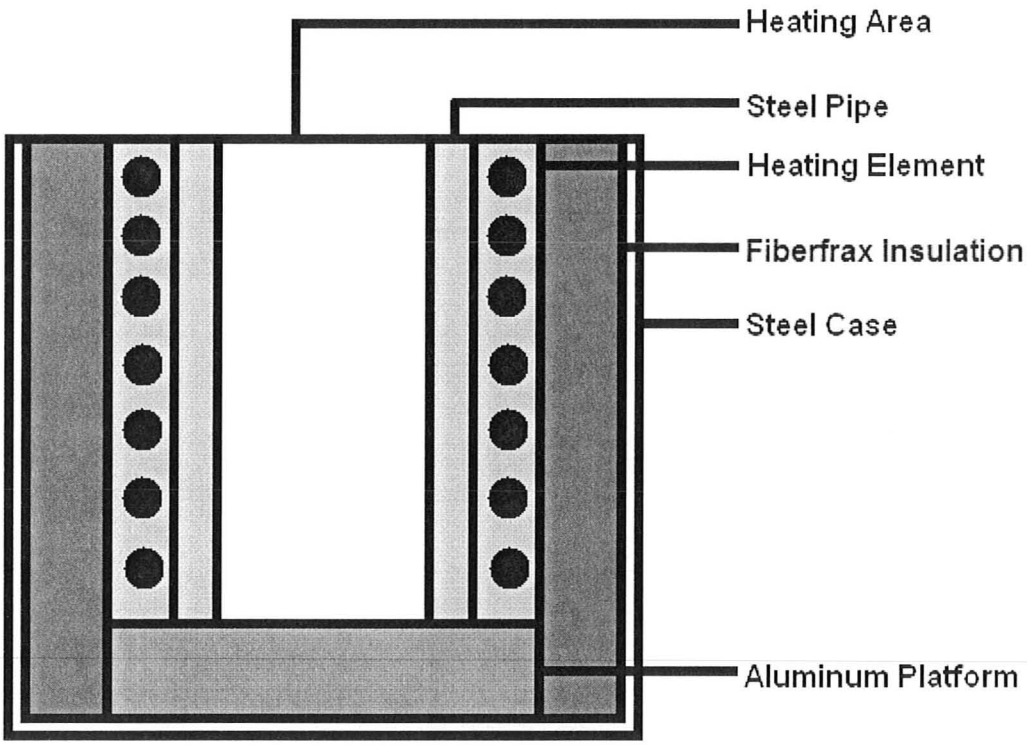


Figure 4.12: An illustration of the vertical section of the furnace for sample preparation

To make this furnace, a steel pipe with an inner diameter 63.5 mm and a height 135 mm was used as the heating chamber. The outer surface of the pipe was coated with *Duranbond-90* high-strength repair compound which acted as an electrical insulator. A *Nichrome* heating wire with a specified resistance of 1.1 to 1.3 Ω/foot was wound evenly along the surface and was coated with another coat of repair compound to electrically insulate the resistance wire from its surroundings. The heating pipe was placed on top of an aluminum platform at the bottom of a tin-coated steel can which had a diameter of 160 mm. The space between the heating pipe and the can was filled with *Fibrefrax* insulating wool and the top of the can was covered with a coat of repair compound. A digital voltmeter indicated that the total length of wire used had a resistance of approximately 14.0 Ω. Therefore, the calculated maximum power of this furnace was approximately 1028 W.

### 4.2.7 Equipment for Analysis

A k-type thermocouple connected to a temperature regulator was placed in a small hole drilled into the capsule or buffer to regulate the temperature of the furnace of the centrifuge assembly maintaining the furnace to the specified temperature. During experiments conducted in stationary conditions, the thermocouple was kept inside the capsule or buffer to measure the cooling rate. It

was removed from the capsule or buffer for the experiments in the spinning condition.

A digital infrared thermometer was used to measure the surface temperature of chamber under both stationary and spinning conditions. The thermometer was manufactured by PowerFist, a division of Princess Auto. Figure 4.13 shows a photograph of the infrared thermometer.

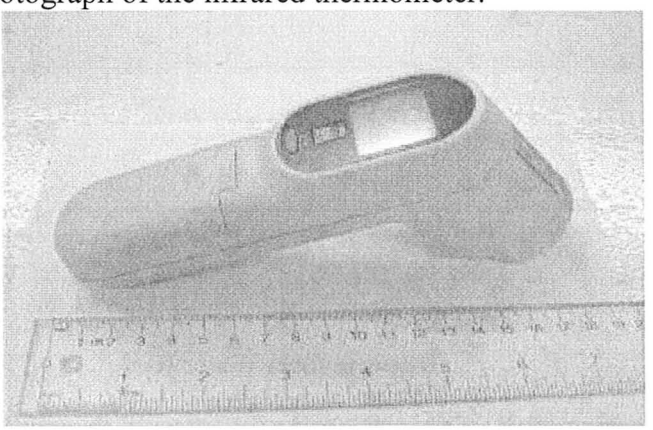

Figure 4.13: Photograph of infrared thermometer

The thermometer had a range between -60°C and 500°C and accuracy the greater of ±2 % or 2°C. It had a fixed emissivity of 0.95 and a distance to spot ratio of 12:1. The accuracy of the distance to spot ratio was confirmed by measuring the temperature of boiling water and ice-water slurry placed in beakers with a diameter of 76.0 mm. Figure 4.14 shows a graph of the displayed temperature with respect to distance from the surface of the water.

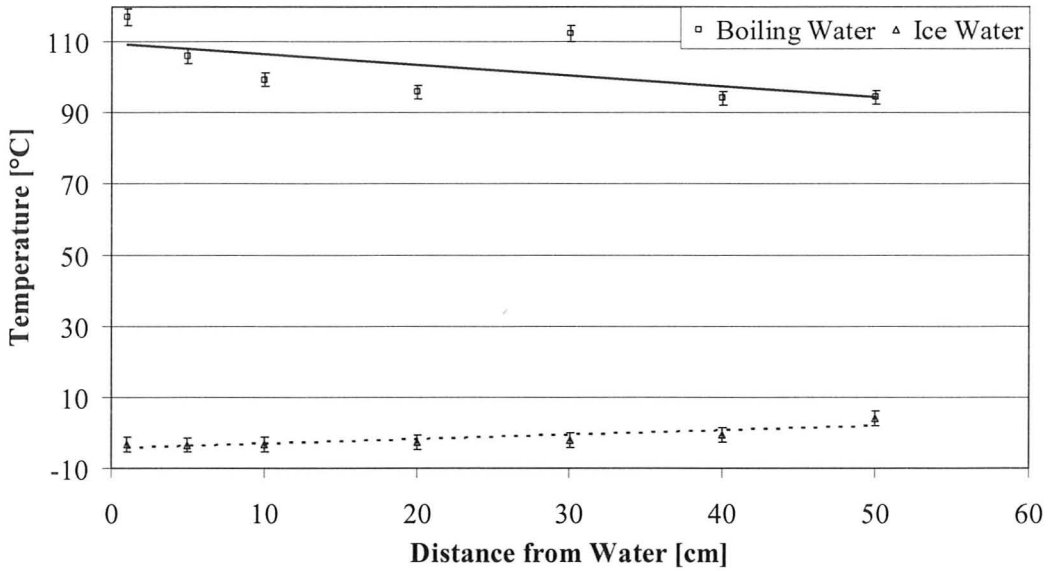


Figure 4.14: Confirmation of specifications for infrared thermometer using ice water and boiling water with respect to distance from surface

When confirming the accuracy of the thermometer with boiling water, the steam produced from the boiling process interfered with the sensor of the thermometer which caused the displayed temperature to differ from the true value. When ice-water slurry was used to confirm the specifications, the error was within the manufacturer's specifications.

Initially, the solidified samples were cut with a hacksaw, but it was later determined that the heat produced from the friction of the hacksaw caused the Sn samples to recrystallize and deform. Therefore, a cutting wheel with coolant injection and a Struers Accutom-5 precision cutter were used to cut the specimens from the solidified samples. The microstructures of the samples were examined wih a Nikon Eclipse LV100 optical microscope equipped with a ×10 ocular lens and objective lenses ranging from ×5 to ×100. It was also equipped with a polarizing lens and a quarter-length waveplate. A digital camera attached to the microscope was connected to a computer in order to capture real-time images of the microstructure and enhance them. The computer software, NIS-Elements BR 3.00 developed by Nikon, was used to analyze the microstructure details. The software also controlled the position of the stage of the microscope so that several images of concurrent position could be captured and "stitched" together to form a composite image. This feature was beneficial in determining the dependence of physical properties on the radius of the solidified sample. The microstructures of the samples were also examined with a Nikon AZ100M optical stereoscope which had a ×10 ocular lens and ×0.5, ×1, and ×5 objective lenses. The stereoscope had a secondary variable magnifying lens ranging from ×1 to ×8 so that the highest magnification of the stereoscope was ×400. Each objective lens was also equipped with a polarizing lens, but it did not possess a quarter-length waveplate.

The imaging software of the stereoscope was also NIS-Elements BR 3.00 and could be used to control the position of the stage to create composite images.

The strength of the solid formed was determined by measuring the hardness of the solidified samples. In this thesis, a *micro*hardness test used a load less than 1000 g and a *macro*hardness test used a load greater than 1000 g. The microhardness tester was manufactured by Clemex which used a diamond Vickers indenter and had a load capability that ranged from 5 g to 1000 g. Two microcalipers were used to control the position of the sample to be indented along the x- and y-axes. The computer software, Clemex CMT 5.0, was used to measure the indentations and calculate the hardness. To measure the macrohardness of the samples, a Zwick 3212 indenter was used. This device also utilized a Vickers indenter, but was capable of higher loads ranging from 0.1 kg to 15 kg. Some of the samples were tested to determine their chemical compositions using Inductively-Coupled Plasma with Optical Emission Spectroscopy (ICP). The model name of the device was Vista-Pro CCD Simultaneous ICP-OES.

For a brief period during this study, it was believed that the heat produced by the cold-mounting process could have caused the Sn samples to recrystallize. Even though the highest temperature recorded was about 35°C, the Sn samples could have still recrystallized. Furthermore, heat generated from the friction of the grinding and polishing process could have also caused recrystallization. Therefore, a special device was made to hold the specimens during grinding, polishing, and microscopy to compare the microstructures between the pre-mounted, cold-mounted, and hot-mounted specimens. Figure 4.15 shows a photograph of the specimen holder.

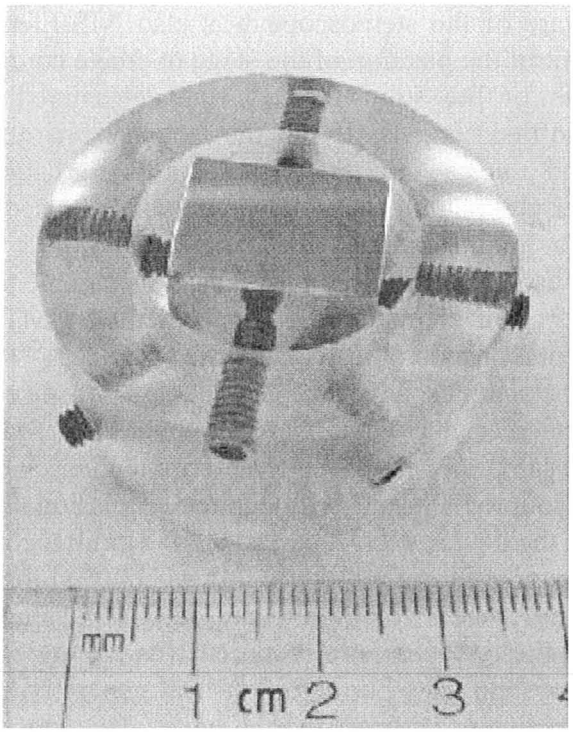


Figure 4.15: Photograph of specimen holder

This device was cylindrical in shape and made of *Plexiglas*. It had an outer diameter of 38.5 mm, an inner diameter of 23.4 mm, and a height of 17.8 mm. The device had eight holes drilled along the circumference in a staggered pattern. These holes were threaded so that up to eight set-screws could be used to hold the cut specimen in place in a specific orientation.

## 4.3 Experimental Procedure

The four materials studied were succinonitrile, Bi-Sn alloy, commercially-pure Sn, and Sn-Cu alloy. Although succinonitrile had a low melting point of 58°C and was easy to solidify, its samples were soft and therefore difficult to mount and its microstructure was difficult to quantitatively analyze. Even though succinonitrile has been used in other experiments on solidification, it was done to study dendritic growth in real-time with a transparent container and not to observe the final microstructure (Glicksman et al. 1995). Real-time observation of solidification and dendritic growth during spinning conditions was not feasible in this experimental setup. Therefore, the study of succinonitrile was discontinued and the study of solidification of metals was continued.

### 4.3.1 Part 1: Sample Preparation with the Container

To produce the Bi-Sn eutectic alloy, the component metals were mixed in the proper mass ratio to attain the lowest melting point of the eutectic. The

weight fractions of Bi and Sn at the eutectic point were 58 wt% Bi and 42 wt% Sn which were determined by the Bi-Sn binary phase diagram shown in Figure 4.16.

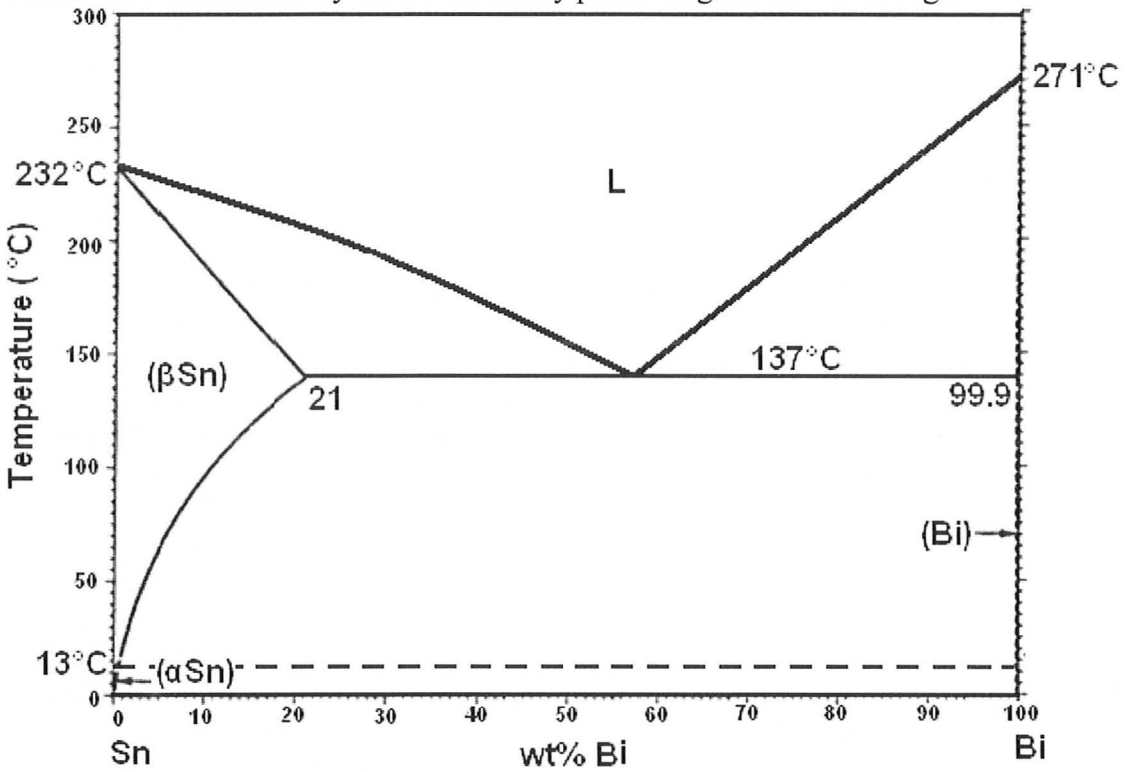


Figure 4.16: Bi-Sn binary phase diagram (Baker 1992)

According to the phase diagram in Figure 4.16, Sn undergoes a solid-solid transformation from β-Sn (white tin) to α-Sn (grey tin) at approximately 13°C. In actuality, the transformation only occurs when the Sn is pure. Furthermore, alloying elements such as Bi and Pb, added to the Sn during the manufacturing process inhibited the transformation.

The volume of the container was calculated as 16 $cm^3$ from its diameter and height. With the density of liquid Bi-Sn eutectic, the approximate mass needed to fill the container was approximately 111.4 g. Thus, for the Bi-Sn eutectic alloy, 58 % of that mass was Bi and 42 % was Sn. A digital mass balance, accurate to ±0.005 g, was used to weigh the amounts of metals to be mixed. Pellets of Bi and Sn were placed into the container and stirred. The container was placed inside the furnace for sample preparation in open atmosphere and heated. To expedite the melting of the metal, the furnace temperature was set at 300°C, well above the melting points of both Sn and Bi. After the metals had completely melted, the melt was stirred with a ceramic rod to homogenize it. The container was removed from the furnace and the melt was allowed to solidify and cool to room temperature. The lid was placed on top of the container and sealed with silicone adhesive, which was given 24 hours to fully cure. The metal in the container was then remelted and then resolidified during

spinning conditions. During the heating process, the Sn coating on the steel container would oxidize which would indicate that the Sn from the coating on the container would diffuse into the eutectic sample and increase the Sn concentration. Since Sn coatings are relatively thin, it would be unlikely to dramatically alter the microstructure of the Bi-Sn eutectic sample.

4.3.2 Part 2: Sample Preparation with the Capsule

Since the $Bi_{58}Sn_{42}$ alloy had a relatively low melting point, the container filled with the melt could be sealed with silicone adhesive and the melt would not leak during spinning conditions. However, a higher furnace temperature was required when Sn and Sn-Cu alloy were used which caused the silicone adhesive to decompose and the melt to leak from the container during spinning conditions. To avoid this occurrence, the container and buffer system were replaced with the capsule. To prepare the sample in the capsule, the middle disc was connected to the bottom disc with two machine screws, essentially making the capsule a metal crucible. By measuring the diameter and height of the cavity in the middle disc, the volume that could fill the cavity was calculated as 10.0 $cm^3$. By multiplying this volume by the liquid density of Sn, the total mass of Sn needed to fill the cavity was calculated. The capsule was placed in the furnace for sample preparation at a temperature of at least 250°C. The capsule cavity was filled with Sn granules and as the granules melted, more granules were added to the capsule cavity. This procedure was repeated until the melt level reached the top of the capsule at which point the capsule was removed from the furnace and the melt was allowed to solidify and cool to room temperature. After the capsule had cooled enough to handle manually, the surface of the capsule that exposed the Sn was grinded and polished flat so that the height of the Sn sample was flush with the capsule. The top disc was then placed on top of middle disc and secured with two more machine screws. The procedure was later modified by placing circular sheets of aluminum foil between the contact surfaces of the discs to act as high-temperature gaskets, further limiting leakage during spinning conditions. The aluminum from the discs and gaskets did not diffuse into the liquid melt because the aluminum oxide layer that immediately formed on the capsule surfaces acted as a barrier to diffusion.

The Sn-Cu alloy was produced unintentionally. It was initially believed that the hydrostatic pressure of the melt against the container wall played a significant role in the solidification morphology. A copper pipe with an outer diameter of 16.0 mm and an inner diameter of 14.0 mm was placed in the center of the capsule cavity during sample preparation and held in place with a Cu washer placed at the bottom of the capsule cavity during spinning conditions. The copper pipe was intended to act as a wall to study the effects of microstructure development under two levels of high-gravity with hydrostatic pressure taken into consideration. The capsule was then placed into the sample furnace and was filled with Sn granules. The granules melted and more granules were added until the melt level reached the height of the capsule. The capsule was then removed

from the furnace, allowed to cool to room temperature, and polished so that the capsule surface, test material, and copper pipe were all flush. The top disc was placed on top of the middle disc and secured by two machine screws so that the sample in the capsule could then be remelted and resolidified during spinning conditions.

### 4.3.3 Part 3: Chamber Preparation

The container was placed inside the buffer which was placed inside the chamber. The stabilizing weight was placed on top of the buffer and the chamber cap was placed on top of the weight. When the capsule was used instead of the container and buffer, the circumferential surface of the capsule was wrapped with a sheet of aluminum foil before being placed in the chamber. This ensured that any melt leakage from the capsule cavity was held within the capsule. Otherwise, the melt tended to solder the capsule to the inside of the chamber wall, making its removal very difficult. The stabilizing weight and the chamber cap were similarly placed on top of the capsule. The chamber was screwed onto the flange of the centrifuge assembly and the furnace was raised to surround the chamber. The temperature inside the furnace was set to ~50°C greater than the melting point of the sample inside the capsule or container. This was done to allow the sample to melt faster and to ensure that nucleation did not occur until after the chamber had started spinning. A k-type thermocouple connected to a temperature regulator to control furnace temperature was placed inside the capsule. The chamber and its contents were heated to the specified temperature and held at that temperature for up to an hour. This ensured that the sample completely liquefied before spinning had started.

### 4.3.4 Part 4: Solidifying in Normal and High-Gravity

When the chamber was being heated, the shaft and bearing boxes in contact with it became hot which increased the power that was required to run the motor of the centrifuge assembly. In some instances, this increase in power caused power surges and overloaded the fuse in the autotransformer which deactivated the motor. To resolve this issue, the shaft and bearing boxes were wiped with a sponge dipped in cold water before the motor was activated. This cooled the shaft and the bearing boxes enough to reduce the power required to start spinning and prevent any overload. After the chamber and its contents were heated inside the furnace for a sufficient time to melt the sample, the furnace was lowered, the thermocouple pulled out, and the furnace raised again. The motor was then activated while the chamber was still in the furnace. Because the shaft and bearing boxes were still relatively hot, it took several seconds for the rotational speed to stabilize. When the chamber reached a steady spinning speed, the furnace was lowered ensuring that solidification did not occur until after the chamber was steadily spinning. After the chamber was spinning and the furnace was lowered, a ceramic block sandwiched between two metal plates was placed on top of the opening of the furnace so that the hot air did not affect the cooling of

the chamber. The air-shield was also place around the spinning chamber to further reduce air circulation and convective heat transport on the chamber surface.

Figure 4.17 shows an illustration of how centrifugal acceleration is exerted on a particle to simulate gravity. From an observer's frame of reference, centripetal acceleration is exerted on the particle due to its circular motion, but from the particle's frame of reference, the particle exerts a downward force which is countered by the container wall thus simulating gravity.

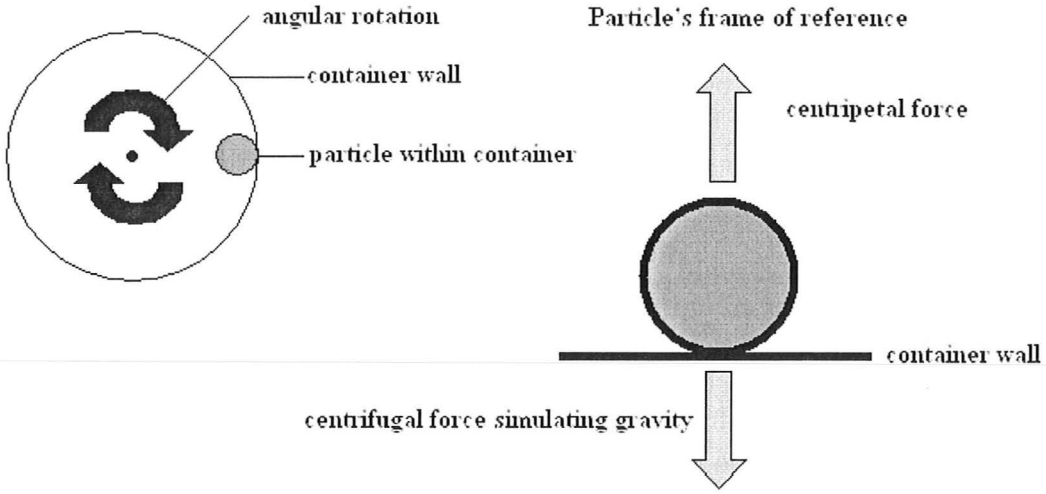


Figure 4.17: An illustration demonstrating centrifugal acceleration

To determine the magnitude of the high-gravitational field exerted on the melt during solidification, the centrifugal acceleration was calculated. The equation for centrifugal acceleration is expressed as:

$$a_{centrifugal} = \omega^2 r \tag{4.3}$$

where $a_{centrifugal}$ is the centrifugal acceleration [m/s$^2$], $r$ is the radius of the sample [m], and $\omega$ is the angular velocity [radians per second]. The equation for angular velocity is expressed as:

$$\omega = \frac{f}{60} * 2\pi \tag{4.4}$$

where $\omega$ is the angular velocity [radians per second] and $f$ is the rotational rate [rpm]. In a trial run, the average rotational rate of the spinning chamber was measured as 4500 rpm with both a handheld digital laser tachometer and a digital mechanical tachometer. Thus, the angular velocity was calculated as 471 radians per second so that the maximum centrifugal acceleration exerted at the outer radius of the melt was calculated as 2,817 m/s$^2$ equivalent to $287g_0$. However, because centrifugal acceleration depends upon the radius of the spinning object, the centrifugal acceleration is zero along the spinning axis of the melt container and increase linearly with the distance from the axis to $287g_0$ at its outer radius.

The melt was solidified by allowing the chamber to cool in air, but some samples were also solidified by quenching the chamber in a bath of cold water or ice-water slurry. When solidification was complete and the chamber was cold enough to handle manually, the chamber was removed from the flange. The capsule or container was then removed from the chamber, dismantled, and the solidified sample was removed. From here onwards, the spinning condition to produce centrifugal acceleration will be referred to as "high-gravity" and static conditions will be referred to as "normal gravity." In addition, samples solidified while spinning to produce centrifugal acceleration will be referred to as "high-gravity samples" and the samples solidified without spinning and no centrifugal acceleration will be referred to as "normal gravity samples."

## 4.4 Sample Preparation and Observation

The solidified samples inside the container were cut in half with a hacksaw. The container was then pulled apart from the sample and disposed. When the sample was held in the capsule, the middle disc of the capsule was placed on top of an aluminum cylinder that had a slightly larger diameter than the hole of the middle disc. A cylindrical metal disc, slightly smaller in diameter than the solidified sample in the middle disc, was placed over the area of the solidified sample. The three components were placed within a hydraulic lever press, which compressed the three pieces together. When the lever press was pushing down on the small disc, the disc would push the solidified sample out of the cavity of the middle disc. Figure 4.18 shows an illustration of how the solidified sample was removed from the capsule cavity.

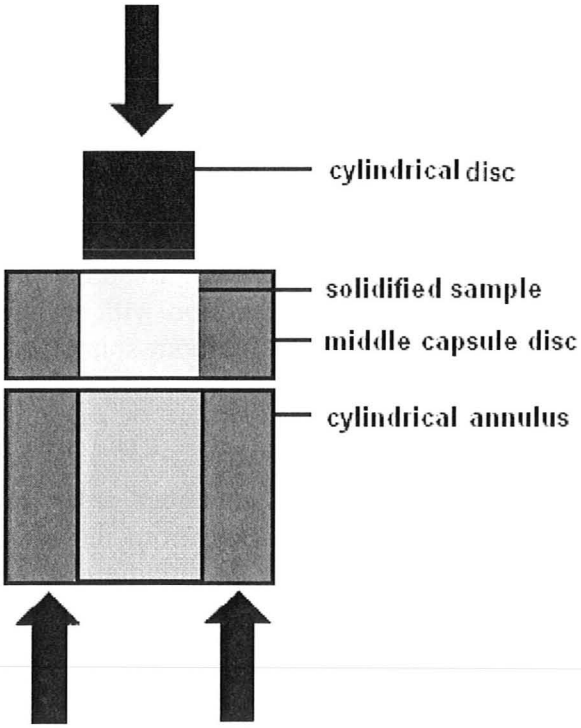


Figure 4.18: An illustration of the device used for extracting the solidified sample from the capsule disc

Specimens were cut from the solidified samples to examine the microstructures of three planes in a cylindrical-based co-ordinate system: Rθ, RZ, and Zθ. The Rθ plane was perpendicular to the axis of spin and co-planar to the direction of solidification and the RZ plane was co-planar to both the axis of spin and the direction of solidification. In principle, the Zθ plane would be the curved circumferential surface of the solidified sample so that it would be perpendicular to the solidification direction and co-planar to the axis of spin. However, it was not practical to polish and examine a curved surface so the curved surfaces of the Zθ plane of the solidified samples were cold-mounted and polished flat. Out of convenience, the flattened plane perpendicular to the solidification direction is referred to as the Zθ plane. Figure 4.19 shows an illustration of the solidified sample and the observed planes.

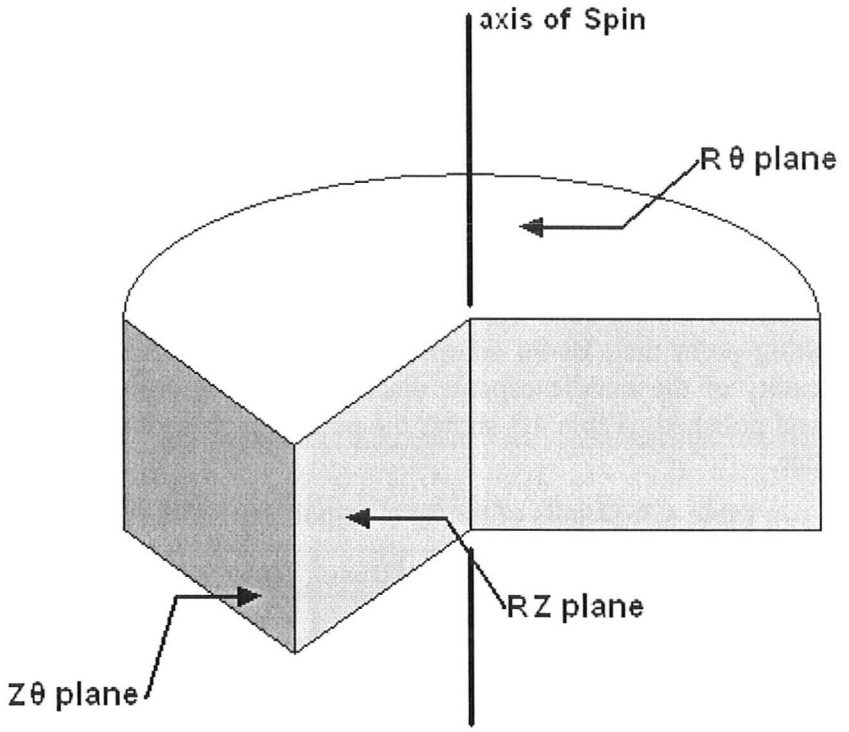


Figure 4.19: Planes of solidified sample examined

The specimens were cold-mounted in epoxy resin, polished, and etched. The low pressure and low temperature of the cold-mounting process ensured that the specimens did not melt, recrystallize, or deform during the mounting process. The mounted specimens were ground and polished using the auto-polisher. The sequence of the polishing procedure for the Bi-Sn alloy is shown in Table 4.2.

Table 4.2: Details of the Bi-Sn auto-polishing procedure

| Surface | Suspension | Dose | Lubricant | Dose | Time | Force | RPM | Direction |
|---|---|---|---|---|---|---|---|---|
| SiC | 1200 grit | - | Water | - | 1.5 min | 10 N | 300 | >> |
| MD-Plan | 9 μm | 4 | BLUE | 6 | 5 min | 15 N | 150 | >> |
| MD-Dur | 3 μm | 5 | RED | 7 | 10 min | 20 N | 150 | >< |
| MD-Chem | OP-S | 8 | - | - | 10 min | 10 N | 150 | >> |

The suspension, OP-S, is a water-based, colloidal silica solution equivalent to a suspension of 0.05 μm. The lubricant, RED, is the DP-Lubricant code: DEPPO supplied by Struers and the lubricant, BLUE, is the DP-Lubricant code: DEPTI, also supplied by Struers. The dose refers to the number of drops of suspension or lubricant being applied to the polishing surface per minute. In addition, the direction, >< refers to the samples being rotated in a counter direction with respect to the surface rotation and >> refers to sample being polished in the same direction as the surface. Between polishing steps, the mounted specimens were

cleaned with soap and water, rinsed in ethanol and blow-dried to minimize the risk of cross contamination. The Bi-Sn alloy samples were etched with a mixture of 25 mL HCl and 8 g of ferric chloride ($FeCl_3$) per 100 mL of water. In some cases, the OP-S used in the polishing procedure acted as an etchant and revealed the microstructure making further etching unnecessary. The microstructures of the high-gravity samples were examined and compared with the microstructures of the normal gravity samples using the optical microscope and stereoscope.

Preparation of the Sn samples was identical to that of the Bi-Sn alloy except the furnace temperature was set higher to 265°C because Sn has a much higher melting point than Bi-Sn eutectic. The solidified sample was removed from the cavity of the middle capsule disc, cut with the precision cutter, cold-mounted, and polished. Table 4.3 shows the polishing procedure for Sn using the auto-polisher.

Table 4.3: Details of the Sn auto-polishing procedure

| Surface | Suspension | Dose | Lubricant | Dose | Time | Force | RPM | Direction |
|---|---|---|---|---|---|---|---|---|
| SiC | 800 grit | - | Water | - | 1 min | 15 N | 300 | >> |
| SiC | 1200 grit | - | Water | - | 1 min | 15 N | 300 | >> |
| SiC | 4000 grit | - | Water | - | 1 min | 15 N | 300 | >> |
| MD-Mol | 3 μm | 4 | RED | 6 | 5 min | 15 N | 150 | >< |
| MD-Chem | OP-S | 7 | - | - | 10 min | 5 N | 150 | >< |

In the final polishing stage, the OP-S was mixed with 2% hydrogen peroxide ($H_2O_2$) and 2% ammonium hydroxide ($NH_4OH$). These chemicals helped break down the Sn-oxide layer that formed on the surface making the etching process more effective. The mounted specimens were etched in a solution of 2 % HCl and 5 % nitric acid ($HNO_3$) in ethanol.

## 4.5 Temperature Measurement

The temperature of the melt was measured during cooling of the melt to determine the rate at which solidification progressed. Initially, a k-type thermocouple placed inside the capsule or buffer during experiments was used to estimate the melt temperature in normal gravity. Later, the fourth capsule disc was used instead of the regular top capsule disc to measure the melt temperature during cooling in trial runs. Two k-type thermocouples insulated in ceramic rods were placed through the holes of the fourth disc and inside the melt. One end of each thermocouple was welded together and placed in the melt and the other end was also welded and placed in a material with a known fixed temperature (ice-water slurry at 0°C) to act as a cold junction. One of the wires at the middle of the thermocouple was cut and connected to a voltmeter which was connected to a computer which recorded the difference in voltage. A computer program developed from Visual Basic 6 by Mr. Daisman Aji of this group converted the difference in voltage to a temperature accurate to ±0.05°C. The temperature was

recorded once per second and plotted in a graph against time. From these graphs, information such as the average cooling rate, solid-liquid interface velocity, and unstable thermal gradients during solidification were determined.

To determine the average cooling rate, the change in temperature while the melt was cooling was divided by the corresponding change in time. The change in temperature was determined from the liquid phase of cooling process rather than the entire cooling process. Figure 4.20 shows an illustration of a typical temperature-time graph of the freezing process which indicates the temperatures and times used to determine the average cooling rate.

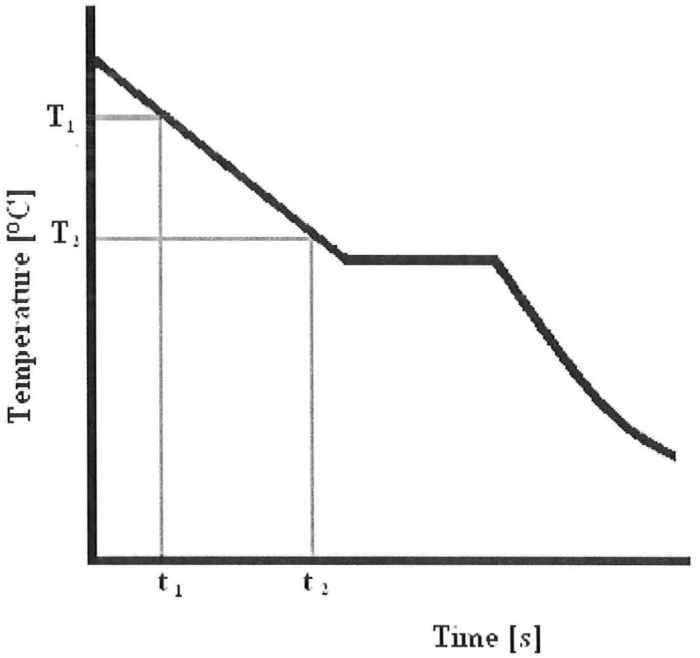


Figure 4.20: An illustration for determining the average cooling rate

Knowing the values of $T_1$, $T_2$, $t_1$, and $t_2$, the average cooling rate was calculated with the following equation:

$$\frac{dT}{dt} = \frac{T_2 - T_1}{t_2 - t_1} \tag{4.5}$$

To determine the approximate solid-liquid interface velocity, it was assumed that the melt was undercooled before nucleation and crystal growth. Therefore, the points in time when maximum undercooling occurred at each thermocouple were determined. The time when maximum undercooling occurred was measured instead of the freezing temperature because of the variance between the temperature reading of the thermocouples and the close proximity of the two thermocouples. Figure 4.21 shows an illustration of how the times of the undercooling were determined.

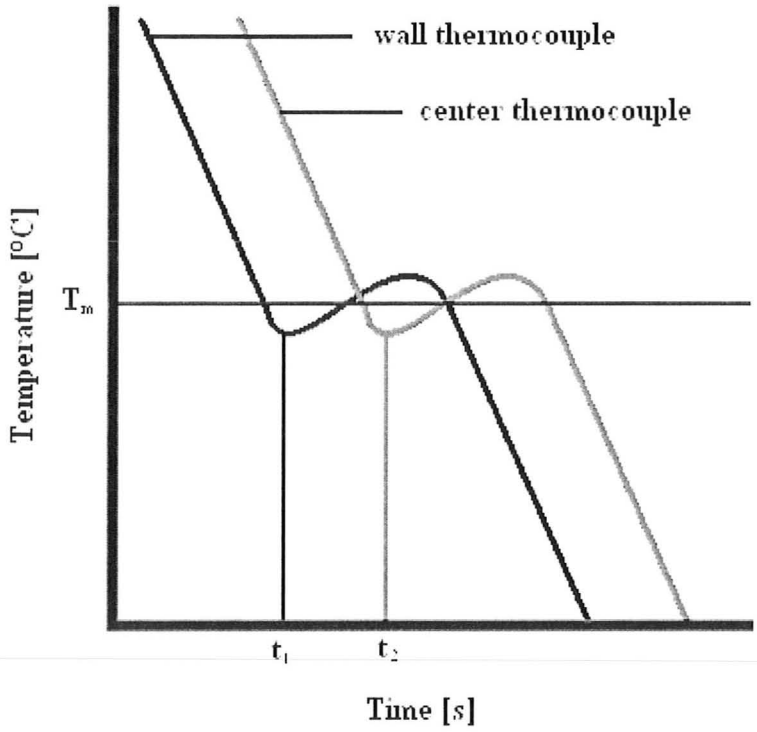


Figure 4.21: An illustration for determining the solid-liquid interface velocity

The correlated points in time when undercooling occurred were determined and with the known fixed distance between the thermocouples, 10.16 mm, the approximate velocity of the solid-liquid interface was calculated based on the following equation:

$$R = \frac{10.16}{t_2 - t_1} \tag{4.6}$$

where $R$ is the solid-liquid interface velocity [mm/s], and $t_2$ and $t_1$ are the points in time when undercooling occurred [s]. It could then be determined based on the Mullins-Sekerka criteria (Flemings 1974) if the solid-liquid interface was stable. Unstable lateral thermal gradients within the melt during solidification were measured because in high-gravity, heavier bodies of mass would move towards the outer radius of the sample. Therefore, if the temperature of the thermocouple at the outer radius was greater than that near the inner radius, there would be an unstable thermal gradient. Unstable thermal gradients that could cause convection could only occur during the liquid phase and the solidification process, not after the entire sample has solidified. With the measured difference in temperature and the known distance between the thermocouples, the unstable thermal gradient was calculated. Unsing the unstable thermal gradient, the Rayleigh number could be calculated and it could be determined if Rayleigh-Bénard convection took place to influence the melt during solidification and thereby affect the microstructure.

## 4.6 Hardness Tests

To quantify and compare the strength of the materials solidified in high-gravity with those solidified in normal gravity, Vickers hardness tests were conducted on the solidified samples because of its availability and its low-load capability. The Sn and Sn alloys tested in this experiment were soft metals, between 10 to 30 HV, so that other hardness tests such as Rockwell were not sensitive enough to measure hardness accurately. A Vickers hardness test uses a diamond indenter in the shape of a square-based pyramid with a peak angle of 106°. With a specific load, the indenter is allowed to make an indentation in the sample for a specified amount of time, the dwell time. The indenter would be removed and the two diagonals of the impression left by the indenter would be measured. The hardness was calculated with the following equation:

$$HV = \frac{1.854 \cdot m}{\bar{d}^2} \tag{4.7}$$

where $HV$ is the Vickers hardness index number [HV], $m$ is the mass of the load [kg], and $\bar{d}$ is the average length of the two diagonals of the indentation [mm] (Callister 2003).

The mounted specimens were placed in the Clemex microhardness tester which automatically indented the sample, measured the dimensions of the indentation, and calculated the hardness accurate to ±0.5 HV. After testing the mounted specimens with several loads, a load of 200 g with a dwell time of 10 s was selected for the Sn and Sn-Cu samples and a load of 25 g with a dwell time of 10 s was selected for the Bi-Sn samples. The indentations were made 1 mm apart along the length of the specimen. Many of the samples, including Bi-Sn alloy, commercially-pure Sn, and $Sn_{99.7}Cu_{0.3}$ alloy were tested. A Zwick 3212 Vickers hardness indenter was used to measure macrohardness with a load of 5 kg and a dwell time of 10 s. Because the test used a higher load, the mounting material would affect the accuracy of the hardness. Therefore, the solidified sample was removed from the capsule cavity and was cut in half along its spinning axis. The cut surface was ground and polished and placed in a mini-vice to ensure that the surface remained fixed when placed on the platform of the indenter. Metal shims were strategically placed underneath the vice to ensure that the surface of the sample was level. The indentations were spaced 3 mm apart to ensure that the indentations did not influence one another. After several indentations were made, the sample was placed under an optical stereoscope and the diagonals of the indentations were measured as well as the indentation's relative distance from the center of the solidified sample. The hardness was plotted against radius to determine if there was a correlation between the hardness and the level of centrifugal acceleration.

# CHAPTER 5: EXPERIMENTAL RESULTS

## 5.1 Studies of Crystallization of Succinonitrile

Even though the crystallization studies of succinonitrile were abandoned, its initial use helped develop the experimental procedure and components. In this study, the container was filled with solid succinonitrile and placed in the chamber with the buffer. The sample was melted and solidified by cooling when the sample contained in the chamber was spun along its vertical axis in air to room temperature (~23°C) thereby creating centrifugal acceleration and simulating the high-gravitational field. The solidified sample was cut in half and the lid was removed. Figure 5.1 shows low-magnification photographs comparing succinonitrile solidified in high-gravity with succinonitrile solidified in normal gravity.

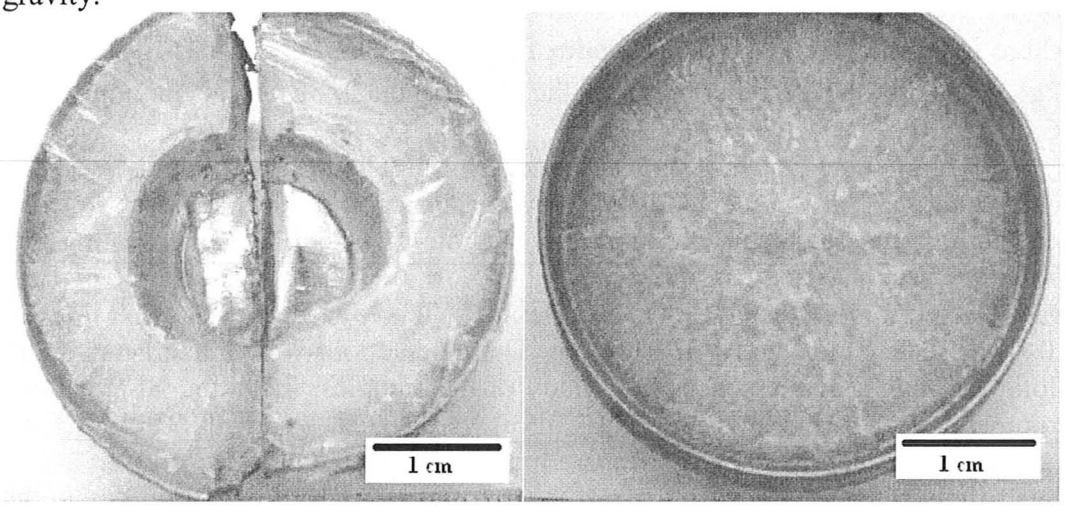


Figure 5.1: Succinonitrile solidified by cooling in air in high-gravity (left), and in normal gravity (right)

In the left image of Figure 5.1, the centrifugal acceleration caused the succinonitrile melt to push against the wall of the container during solidification. This left a void in the center of the container caused by air moving towards the center of the container. The direction of terrestrial gravity is perpendicular to the image plane and centrifugal acceleration is in the radial direction. More succinonitrile was placed in another container and melted and resolidified in the chamber in normal gravity. In the right image of Figure 5.1, there is no void in the center of the container because there was no centrifugal acceleration to push the liquid toward the container wall. The direction of gravity is perpendicular to the image plane. After the experiment had been done with succinonitrile, Bi-Sn eutectic was used.

## 5.2 Studies of the Bi-Sn Alloys

Bi-Sn alloy of hypereutectic, eutectic, and hypoeutectic compositions were examined. The Bi-Sn hypereutectic alloy of ~50 wt% Sn was solidified with two cooling rates to determine its effect on microstructure development in high-gravity. For this purpose, the melt was solidified by cooling in air to room temperature (~23°C) and by quenching in ice-water slurry (0°C). The eutectic areas of the hypereutectic alloy of both cooling conditions were examined by optical microscopy. The Bi-Sn hypoeutectic alloy of ~25 wt% Sn was solidified only by cooling in air to room temperature.

### 5.2.1 Solidification Conditions of Bi-Sn Alloy Cooled in Air

The solidification conditions for the Bi-Sn alloys solidified by cooling in air were determined by conducting a trial run. Two thermocouples were placed into the melt during solidification to measure the temperature against time. Figure 5.2 shows the temperature-time graphs for the Bi-Sn alloy cooled in air. From this procedure, the average cooling rate, solid-liquid interface velocity, and the maximum unstable thermal gradient were determined for normal gravity, and approximated for high-gravity.

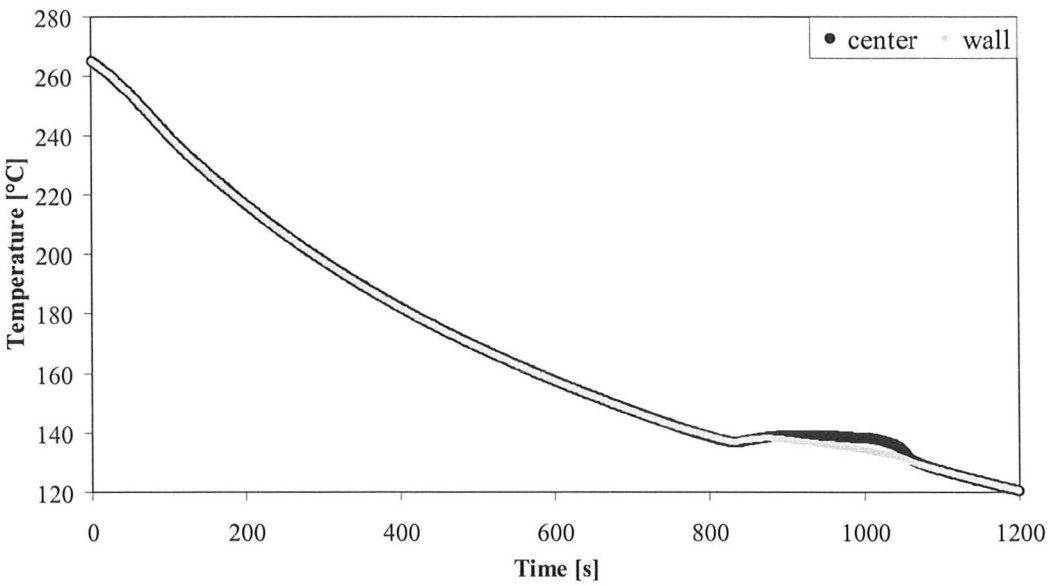


Figure 5.2: Temperature-time graphs for Bi-Sn alloy, air-cooled in normal gravity

The average cooling rate was determined by measuring the slope of the graph titled "wall" from Figure 5.2. From 232°C to 138°C, and from 132 s to 1004 s, the average cooling rate was 0.11 K/s. The solid-liquid interface velocity would be used to determine the solidification and growth rates. When a liquid's temperature increases upon crystallization in the undercooled state, a significant amount of heat is released, and this is taken as the beginning of solidification. From Figure 5.2, the maximum undercooling at the wall and center

thermocouples occurred at 836 s and 839 s, respectively. Knowing the distance between the thermocouples, it took 3 s for the solid-liquid interface to travel 10.16 mm so that the solid-liquid interface velocity was 3.39 mm/s. The maximum unstable thermal gradient would determine if Rayleigh-Bénard convection influenced solidification in high-gravity. For an unstable thermal gradient to exist, the temperature at the wall must be higher than the temperature at the center. The highest unstable temperature difference was 0.3 K and occurred at 806 s. Knowing the distance between the thermocouples, the maximum unstable thermal gradient was 0.03 K/mm.

5.2.2 Bi-Sn Eutectic Cooled in Air

After the melt had been solidified, the sample was removed from the container, cut, mounted, polished, and etched in the $HCl/FeCl_3/H_2O$ solution. Images of the microstructure were obtained with the optical microscope. Since Bi and Sn both have anisotropic crystal structures, the samples were examined in different planes to determine if there was any growth behaviour unique to the examined planes. Figure 5.3 to Figure 5.5 show the microstructures of the Bi-Sn eutectic, solidified in high-gravity by cooling in air, and viewed in the RZ, Rθ, and Zθ planes, respectively. Each figure shows two images taken from two areas from the specimen; the image on the left is from the high radius (high-gravity) area of the sample, and the image on the right is from the low radius (low-gravity) area of the sample. In these images, the dark areas are the Sn phase and the light areas are the Bi phase.

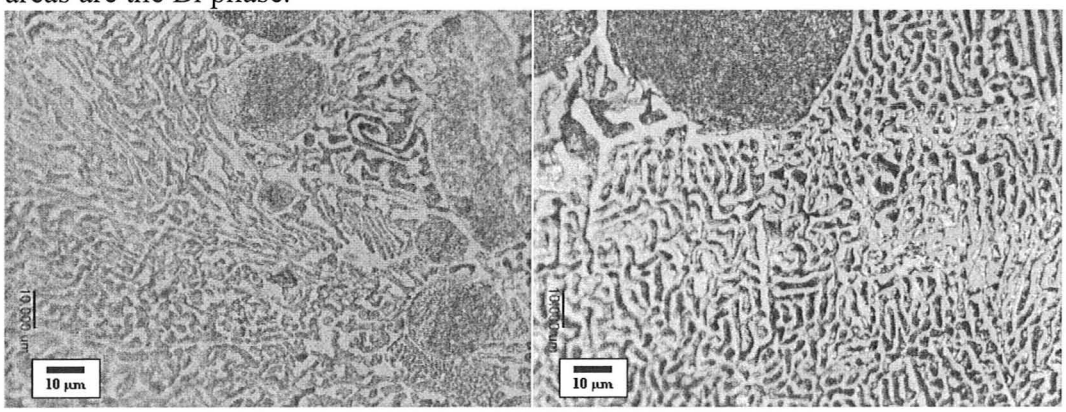


Figure 5.3: Bi-Sn eutectic, air-cooled in high-gravity, RZ plane, etched - high-radius area (left), low-radius area (right)

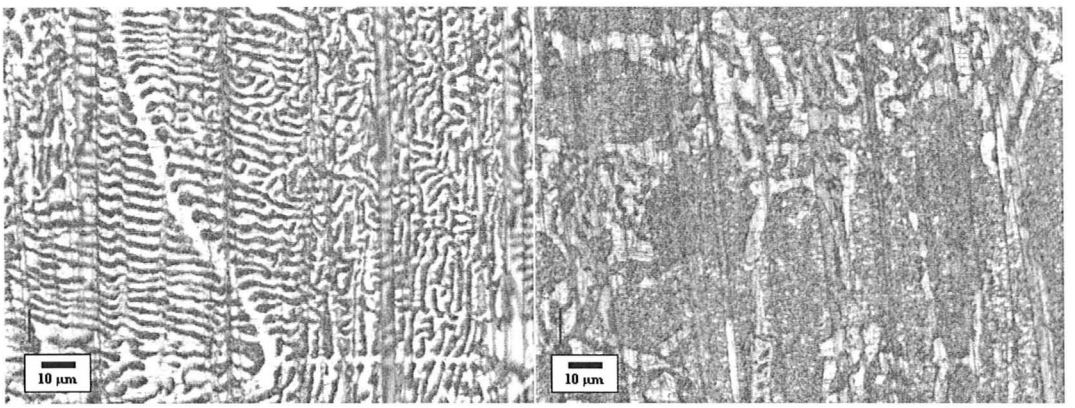


Figure 5.4: Bi-Sn eutectic, air-cooled in high-gravity, Rθ plane, etched - high-radius area (left), low-radius area (right)

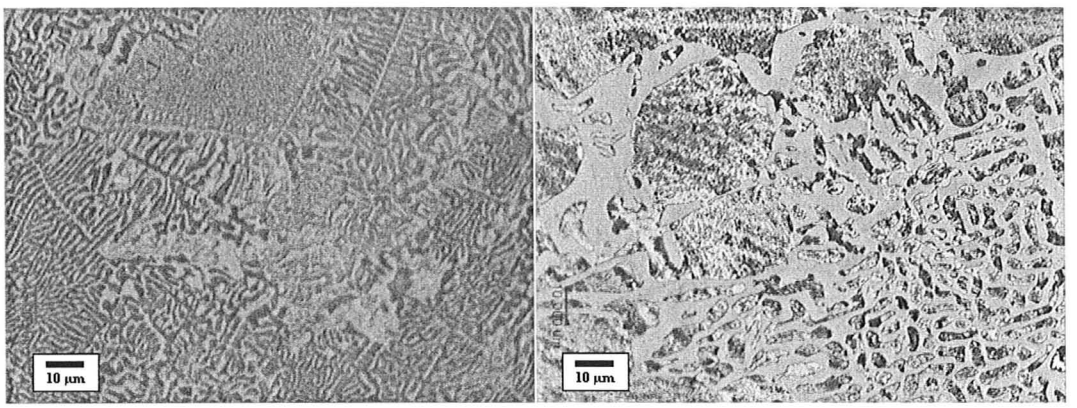


Figure 5.5: Bi-Sn eutectic, air-cooled in high-gravity, Zθ plane, etched - high-radius area (left), low radius area (right)

Figure 5.3 to Figure 5.5 show that the microstructure of Bi-Sn alloy is a lamellar eutectic. Furthermore, in Figure 5.3 and Figure 5.5, the eutectic spacing in the high radius areas appears to be finer than in the low radius areas. To compare the high-gravity samples, the Bi-Sn melt was solidified by cooling in air, but in normal gravity. Figure 5.6 to Figure 5.8 compare the microstructures taken from the normal gravity sample with those taken from the high-gravity sample viewed in the RZ, Rθ, and Zθ planes, respectively. It was assumed that the microstructure in the case of normal gravity would remain unchanged with respect to radius because there was no varying centrifugal acceleration affecting solidification. In these images, the dark areas are the Sn phase and the light areas are the Bi phase.

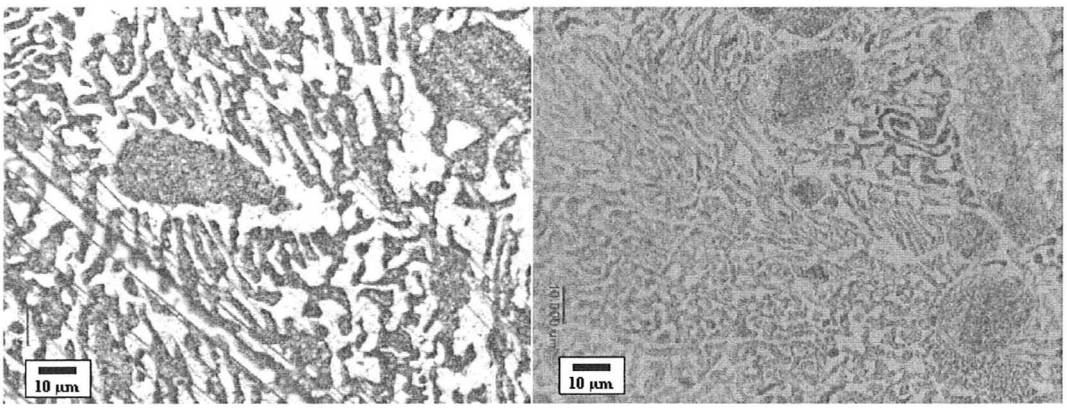


Figure 5.6: Bi-Sn eutectic, air-cooled, RZ plane, etched - normal gravity (left), high-gravity (right)

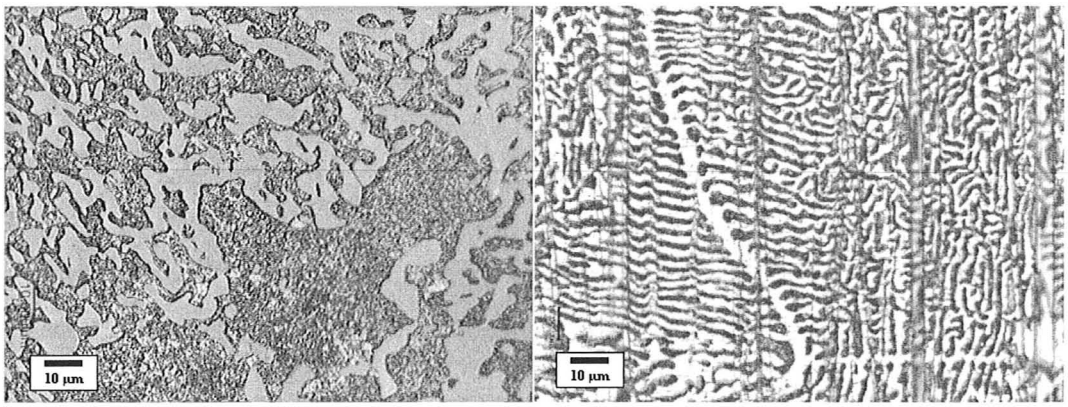


Figure 5.7: Bi-Sn eutectic, air-cooled, Rθ plane, etched - normal gravity (left), high-gravity (right)

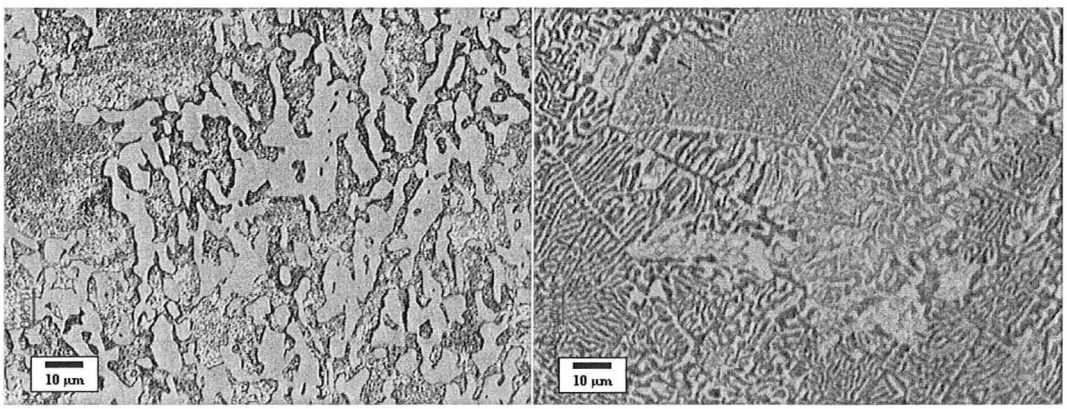


Figure 5.8: Bi-Sn eutectic, air-cooled, Zθ plane, etched - normal gravity (left), high-gravity (right)

Figure 5.6 to Figure 5.8 show that the microstructure of the Bi-Sn alloy also had a lamellar eutectic similar to the high-gravity samples. However, the eutectic

structure from the high-gravity samples appeared as "complex regular," whereas the eutectic structure from the normal gravity sample appeared as "irregular."

### 5.2.3 Bi-Sn Hypereutectic Cooled in Air

The eutectic structure was taken from a Bi-Sn alloy of a hypereutectic composition of ~50 wt% Sn. As a result, the high- and normal gravity samples had areas of primary Sn phase that existed with the eutectic microstructure which appeared as dendrites. Figure 5.9 shows the micrographs of the microstructure of the Bi-Sn hypereutectic, solidified by cooling in air in high-gravity, and viewed in the RZ plane in the high-radius and low-radius areas. The black areas are the primary Sn phase and the grey areas are the Bi-Sn eutectic.

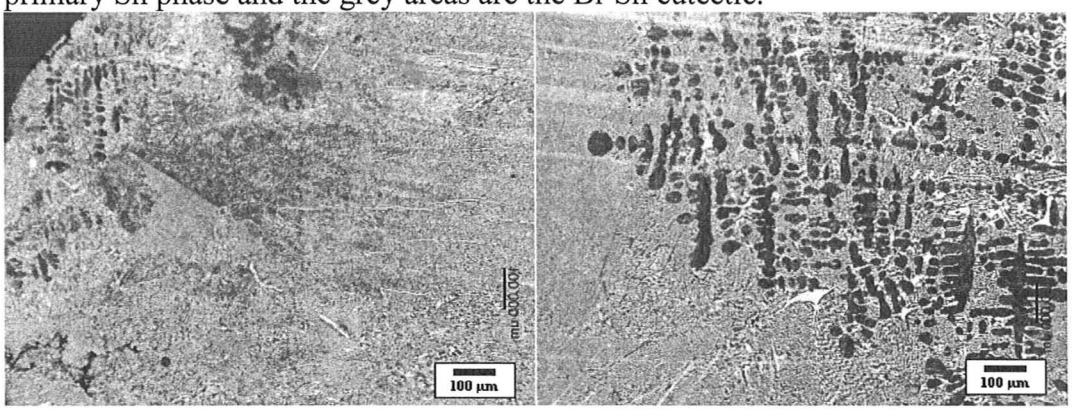


Figure 5.9: Bi-Sn hypereutectic, air-cooled in high-gravity, RZ plane, etched - high-radius (left), low-radius (right)

The image of the left shows the high-radius area of the sample and the image of the right shows the low-radius area of the sample. The Sn dendrites were localized in the low-radius area of the sample with some exceptions in the high-radius area. The Bi-Sn hypereutectic alloy was solidified again in normal gravity to compare the location of the primary phase. Figure 5.10 compares the micrographs of the Bi-Sn hypereutectic alloy solidified by cooling in air in normal gravity with that solidified in high-gravity.

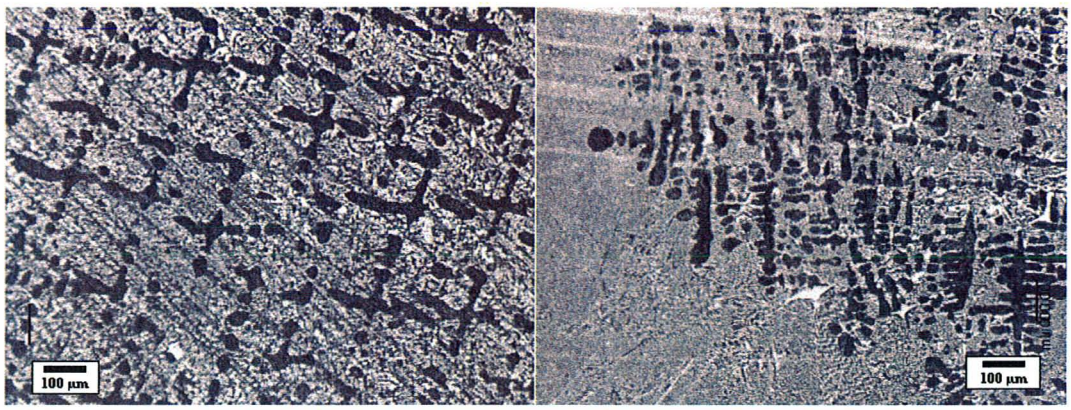


Figure 5.10: Bi-Sn hypereutectic, air-cooled, RZ plane, etched - normal gravity (left), high-gravity (right)

In the left image of Figure 5.10, the Sn dendrites are evenly distributed throughout the microstructure in normal gravity whereas the right image shows that the Sn dendrites were localized to one end of the sample in high-gravity. In order to map the morphology of primary Sn in the entire solidified sample, the Nikon AZ100M optical stereoscope with a polarizing lens was used to obtain an image of the entire Rθ surface of the solidified sample. Figure 5.11 compares the micrographs of the Bi-Sn hypereutectic alloy solidified in high-gravity with that solidified in normal gravity in the middle of the sample.


Figure 5.11: Bi-Sn hypereutectic, air-cooled, Rθ plane, unetched, viewed with polarized light - high-gravity (left), normal gravity (right)

In the left image of Figure 5.11, centrifugal acceleration is parallel with radius and terrestrial gravity is perpendicular to the image plane. The Sn dendrites are localized to the center area of the sample. The void in the center was caused by air pockets moving toward the center before solidification occurred, similar to that observed for the high-gravity experiment with succinonitrile. In the right image of Figure 5.11, there is no centrifugal acceleration and gravity is perpendicular to the image plane. The Sn dendrites are finer and more evenly distributed throughout the entire sample in normal gravity than the sample solidified in high-gravity.

### 5.2.4 Bi-Sn Hypoeutectic Cooled in Air

Bi-Sn hypoeutectic melt of composition 75 wt% Bi and 25 wt% Sn was also solidified by cooling in air. According to the Bi-Sn phase diagram shown in Figure 4.16, the melting point of the alloy at this composition is 182.5°C. It was assumed that the solidification conditions and hence the temperature-time graphs during cooling were similar to the one obtained for the hypereutectic alloy shown in Figure 5.2. Using the Nikon LV100 optical microscope and computer software, several images for microstructure of each sample specimen were obtained and "stitched" together to form a large image to compare the microstructure formed at different radius of the sample. Figure 5.12 to Figure 5.14 show the microstructures of the Bi-Sn hypoeutectic alloy solidified in high-gravity in the Rθ, RZ, and Zθ planes, respectively. The white areas show the primary Bi phase and the grey areas show the Bi-Sn eutectic. Arrows with "G" next to the scale bars denote the high-gravity vector for samples solidified with centrifugal acceleration, and those with "R" show the increasing radius of the sample solidified in normal gravity.


Figure 5.12: Bi-Sn hypoeutectic, air-cooled in high-gravity, Rθ plane, unetched

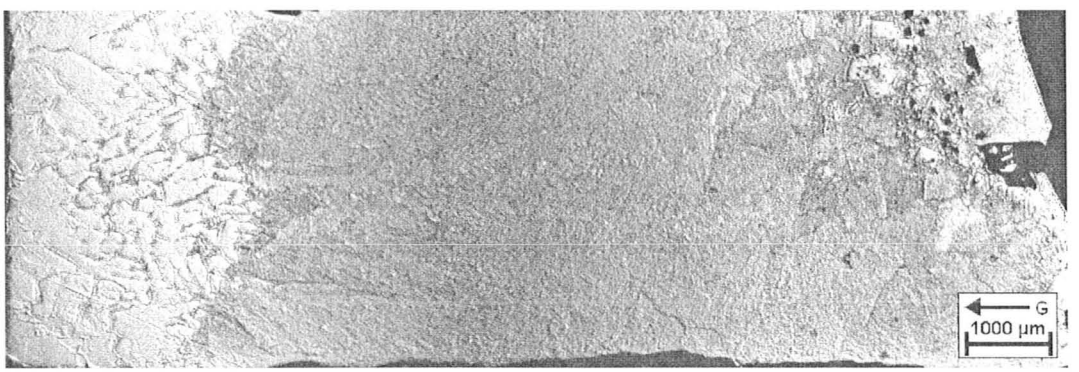


Figure 5.13: Bi-Sn hypoeutectic, air-cooled in high-gravity, RZ plane, unetched

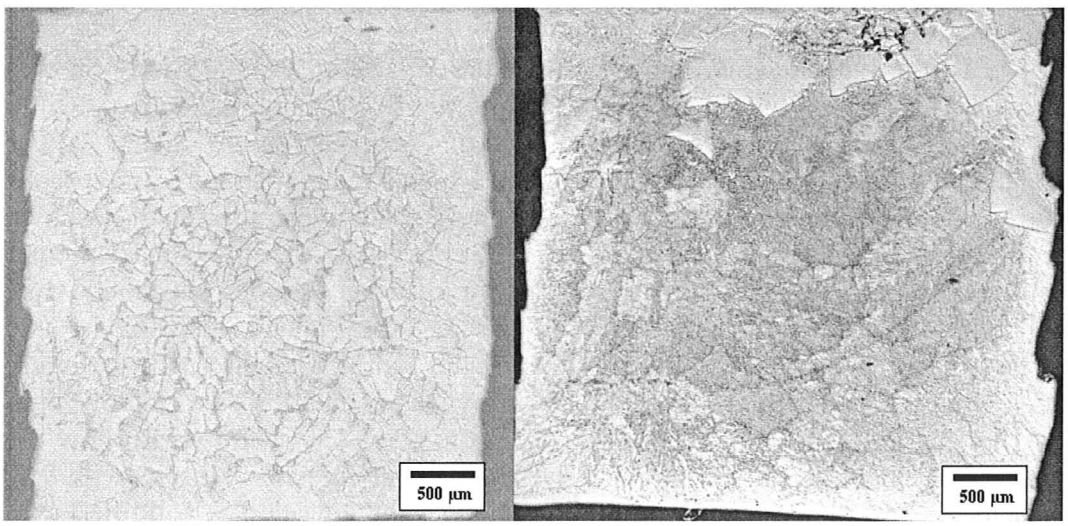


Figure 5.14: Bi-Sn hypoeutectic, air-cooled in high-gravity, Zθ plane, unetched - high-radius (left), low-radius (right)

In Figure 5.12 to Figure 5.14, the primary Bi phase nucleated and grew as faceted crystals. These crystals were localized to the high-radius area of the sample with some exceptions in the low-radius area. The separation is likely caused by the higher density of the Bi crystals relative to the Bi-Sn eutectic melt causing crystals to move to the high-radius area of the melt. In the hypereutectic alloy, the primary Sn phase was mostly localized to the low-radius area because the density of the Sn crystals was lower than the Bi-Sn eutectic. To compare high-gravity with normal gravity, the Bi-Sn hypoeutectic melt was also allowed to solidify in normal gravity. Figure 5.15 to Figure 5.17 show the microstructures of the Bi-Sn hypoeutectic alloy, solidified by cooling in air, in normal gravity, and in the Rθ, RZ, and Zθ, respectively.

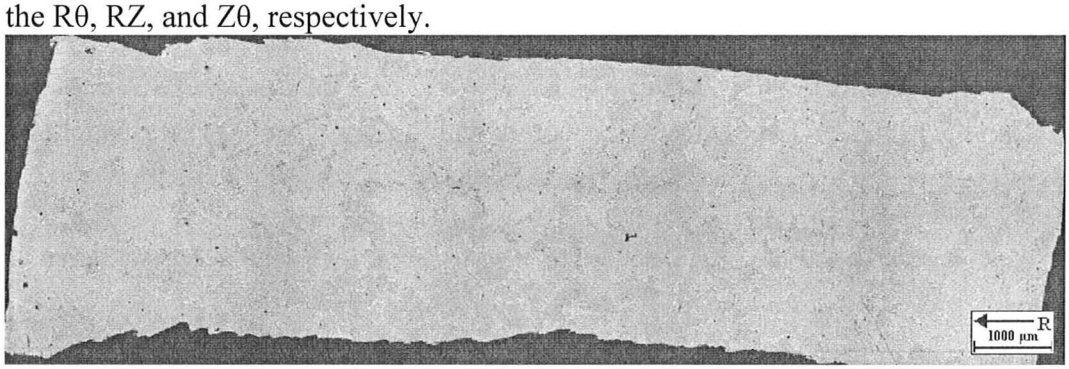


Figure 5.15: Bi-Sn hypoeutectic, air-cooled in normal gravity, Rθ plane, unetched


Figure 5.16: Bi-Sn hypoeutectic, air-cooled in normal gravity, RZ plane, unetched

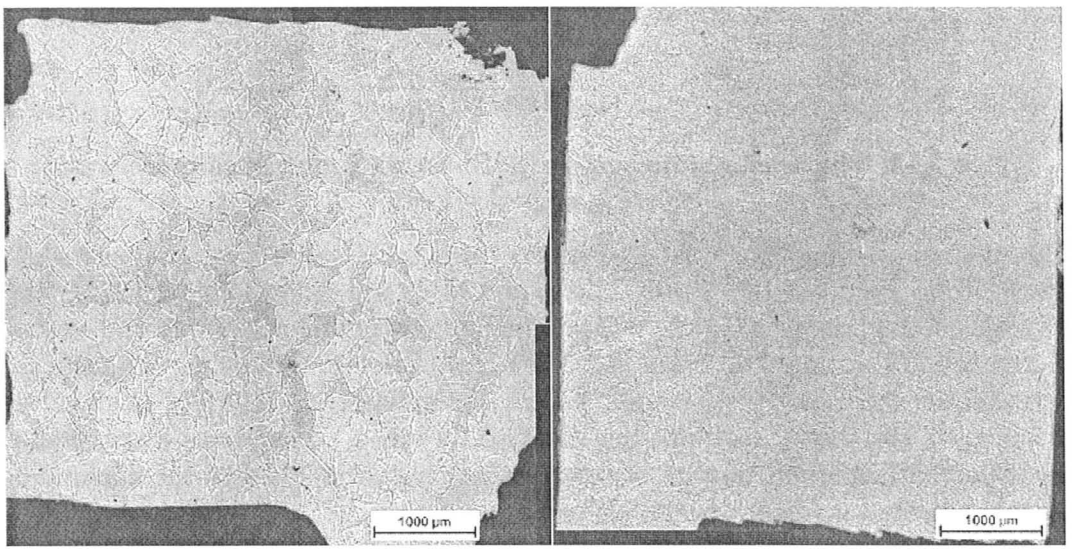


Figure 5.17: Bi-Sn hypoeutectic, air-cooled in normal gravity, Zθ plane, unetched - high-radius (left), low-radius (right)

Figure 5.15 shows that the primary Bi phase is evenly distributed throughout the specimen, and Figure 5.16 shows that the primary Bi phase is localized to the outer radius and bottom of the sample which would indicate that the hypoeutectic is affected by terrestrial gravity. In Figure 5.17, the concentration of primary Bi phase is higher in the high-radius area than the low-radius area.

### 5.2.5 Solidification Conditions of Bi-Sn Alloy Quenched in Ice-Water Slurry

To examine the effect of cooling rate on microstructure development in high-gravity, the Bi-Sn alloy melt was solidified also by quenching the chamber in ice-water slurry at 0°C. As before, this was done in a trial run by placing two thermocouples into the melt during solidification to measure the temperature. Figure 5.18 shows the plotted graphs of temperature against time during solidification.

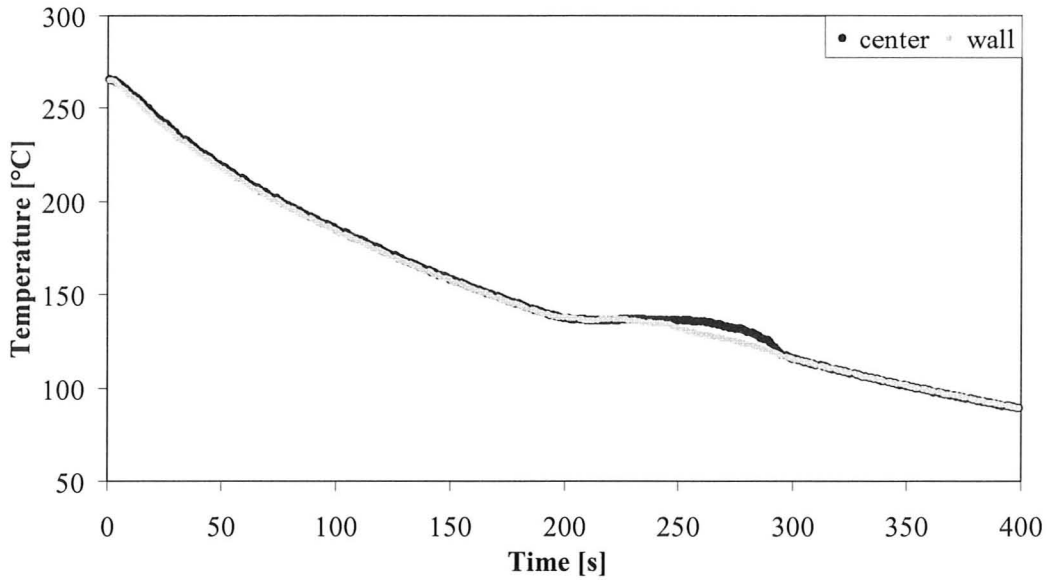


Figure 5.18: Temperature-time graphs for Bi-Sn alloy, quenched in ice-water slurry in normal gravity

The average cooling rate was determined from the slope of the graph labeled "wall" from Figure 5.18. From 232°C to 138°C and from 35 s to 197 s, the average cooling rate was 0.58 K/s. Maximum undercooling at the wall and center thermocouples occurred at 211 s and 213 s, respectively. Knowing the distance between the thermocouples, it took 2 s for the solid-liquid interface to travel a distance of 10.16 mm, making its velocity 5.08 mm/s. There was a maximum unstable temperature difference of 0.5 K that occurred at 202 s so the maximum unstable thermal gradient was 0.05 K/mm.

### 5.2.6 Bi-Sn Eutectic Quenched in Ice-Water Slurry

After the sample was solidified in high-gravity, it was removed from the capsule, cut, mounted, and polished. The specimens were not etched with the specified etchant because during the polishing process, the colloidal silica solution had lightly etched the surface enough to reveal their microstructure. The microstructure of the high-gravity sample was examined and compared with that taken from the normal gravity sample. Figure 5.19 to Figure 5.21 compare the micrographs of the high-gravity sample with those of the normal gravity sample viewed in the Rθ, RZ, and Zθ planes, respectively. The light areas show the Sn phase and the dark areas show the Bi phase.

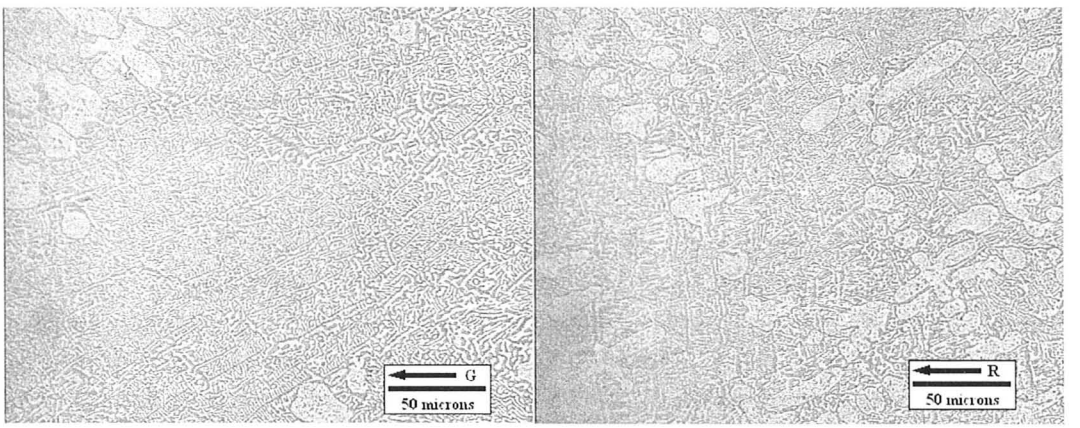


Figure 5.19: Bi-Sn eutectic, ice-water quenched, Rθ plane, unetched - high-gravity (left), normal gravity (right)

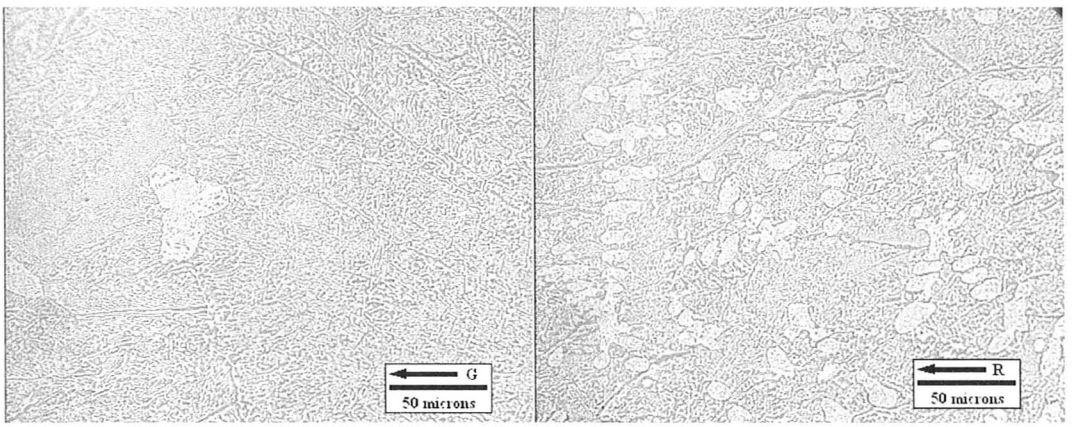


Figure 5.20: Bi-Sn eutectic, ice-water quenched, RZ plane, unetched – high-gravity (left) normal gravity (right)

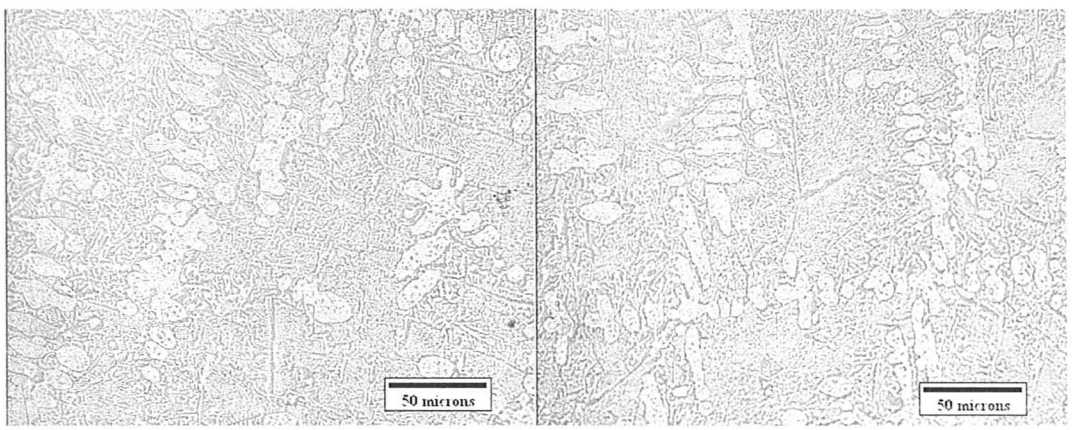


Figure 5.21: Bi-Sn eutectic, ice-water quenched, Zθ plane, unetched – high-gravity (left) normal gravity (right)

Figure 5.19 to Figure 5.21 indicate that the eutectic structure is lamellar in both the high- and normal gravity samples. There appears to be no qualitative difference between the lamellar eutectic phase formed in the high-gravity sample and that formed from the normal gravity sample as both exhibit complex regular microstructures.

### 5.2.7 Bi-Sn Hypereutectic Quenched in Ice-Water Slurry

Bi-Sn hypereutectic melt was also solidified by quenching in ice-water slurry. The high-gravity sample was cut, mounted, polished, and etched only with the colloidal silica solution. Figure 5.22 to Figure 5.24 show the micrographs of the high-gravity sample in the high- and low-radius areas viewed in the Rθ, RZ, and Zθ planes, respectively. The white areas show the primary Sn phase and the grey areas show the eutectic phase.

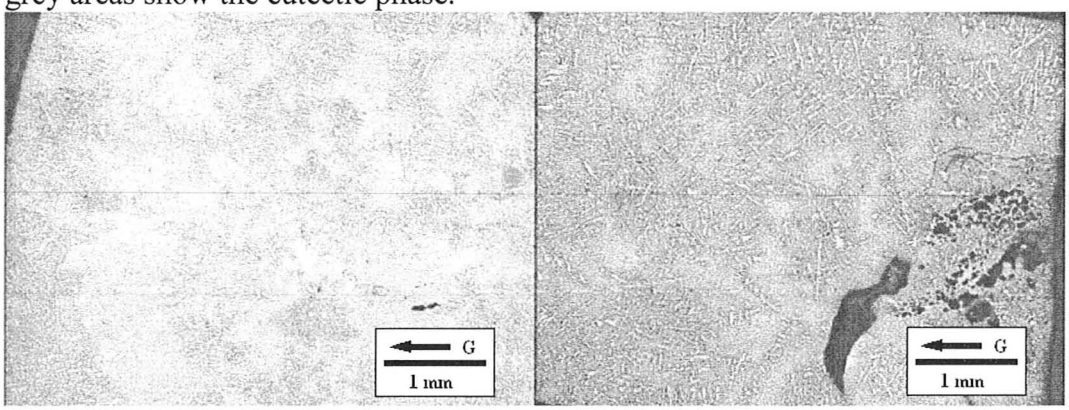


Figure 5.22: Bi-Sn hypereutectic, ice-water quenched in high-gravity, Rθ plane - high-radius (left), low-radius (right)

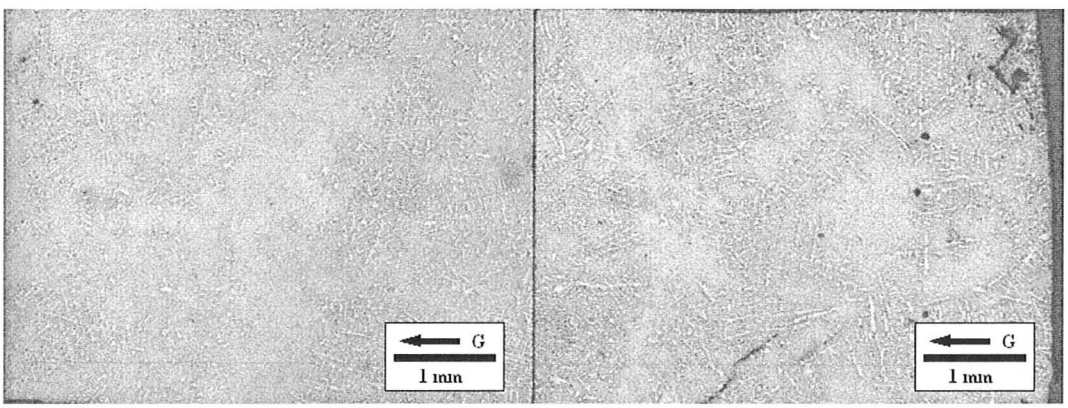


Figure 5.23: Bi-Sn hypereutectic, ice-water quenched in high-gravity, RZ plane - high-radius (left), low radius (right)

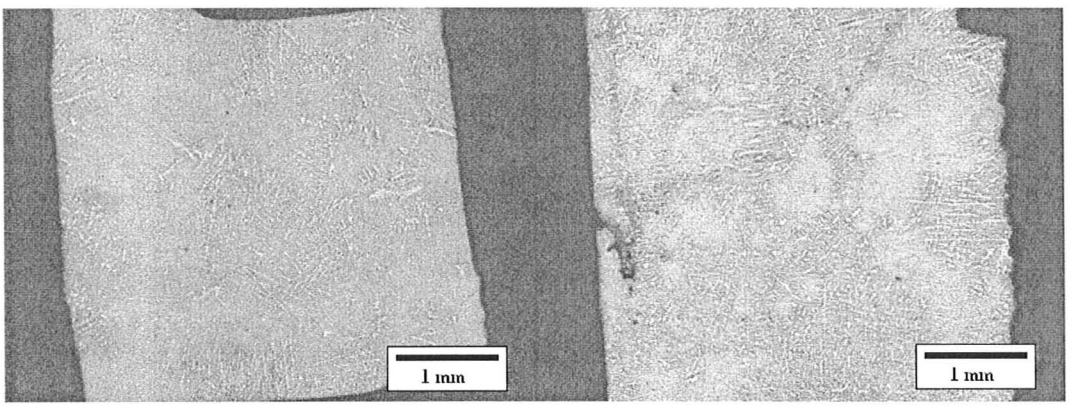


Figure 5.24: Bi-Sn hypereutectic, ice-water quenched in high-gravity, Zθ plane - high-radius (left), low-radius (right)

In Figure 5.22 to Figure 5.24, Sn dendrites appear in both the high- and low-radius areas of the sample, but there are more Sn dendrites in the low-radius area when compared to the high-radius area. Furthermore, the Sn dendrites in the high-gravity sample are more evenly distributed throughout the entire sample rather than being isolated to the low-radius area when solidified by quenching in ice-water slurry compared to cooling in air. The hypereutectic melt was also solidified by quenching in ice-water slurry in normal gravity. Figure 5.25 to Figure 5.27 show the normal gravity sample viewed in the Rθ, RZ, and Zθ planes, respectively.

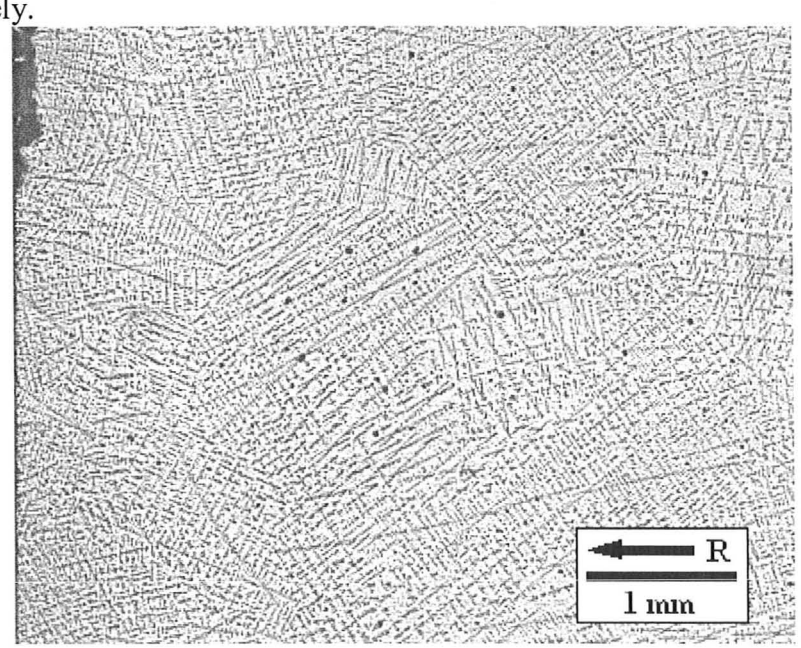


Figure 5.25: Bi-Sn hypereutectic, ice-water quenched in normal gravity, Rθ plane, unetched

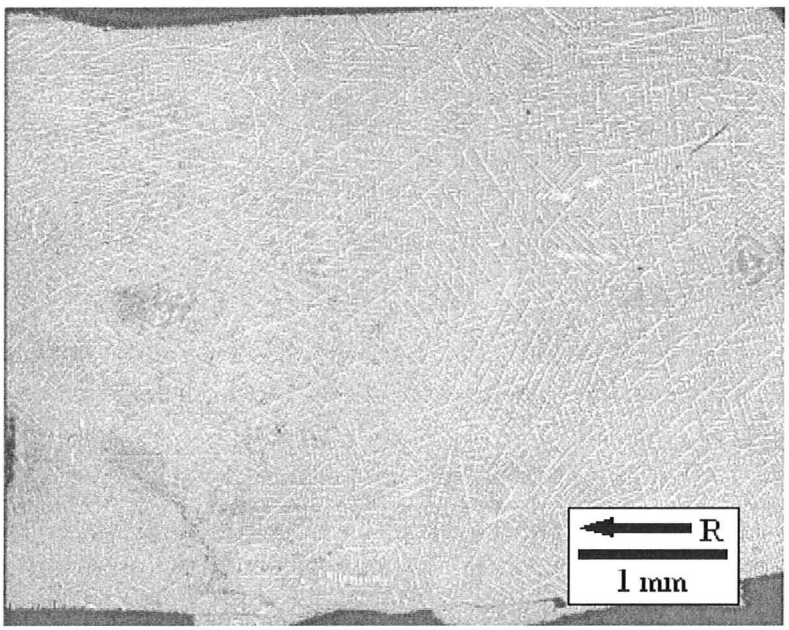


Figure 5.26: Bi-Sn hypereutectic, ice-water quenched in normal gravity, RZ plane, unetched

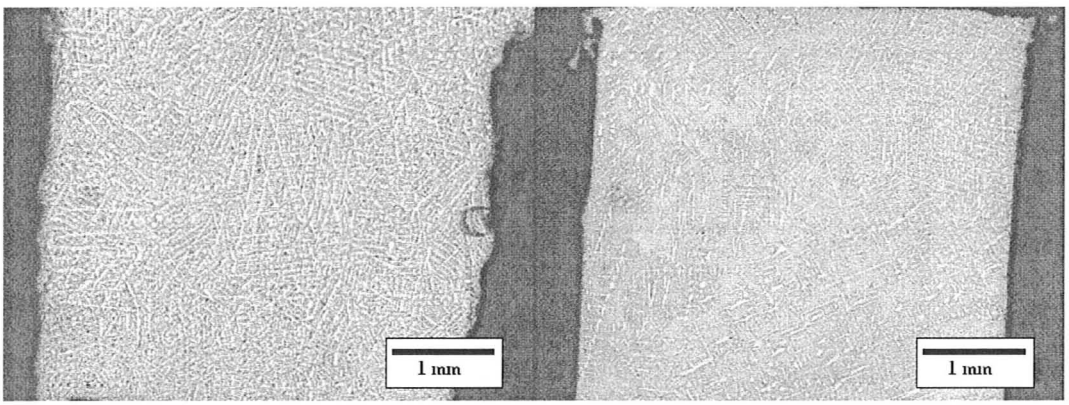


Figure 5.27: Bi-Sn hypereutectic, ice-water quenched in normal gravity, Zθ plane, unetched - high-radius (left) and low-radius (right)

Figure 5.25 to Figure 5.27 show that there are more Sn dendrites in the normal gravity sample than in the high-gravity sample. The normal gravity samples have larger dendrite grains when compared to the high-gravity samples. Figure 5.28 compares the micrographs of the quenched normal gravity sample and the air-cooled normal gravity sample.

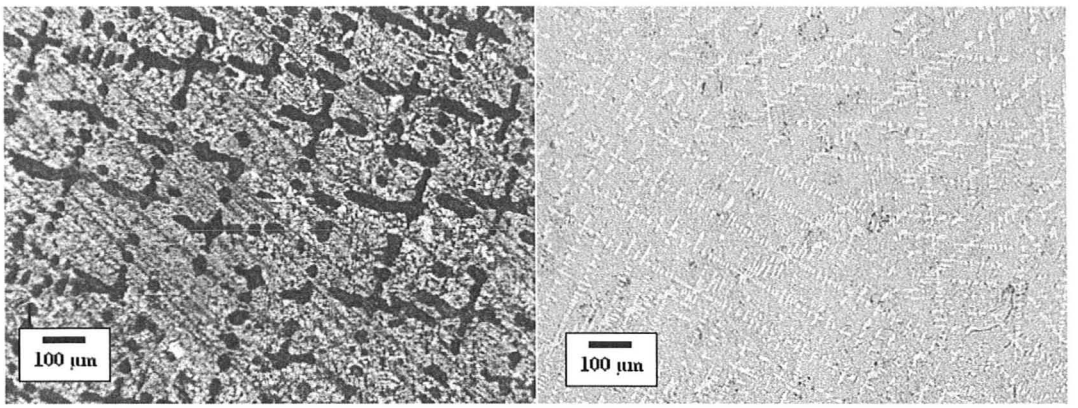


Figure 5.28: Comparison of different cooling rates for Bi-Sn hypereutectic in normal gravity - air-cooled (left), ice-water slurry quenched (right)

Because the micrograph on the left was originally ×32 and the one on the right was ×50, the images were resized to match the scale, but the aspect ratio of the images was kept constant. The quenched normal gravity sample exhibits finer dendrite grains and smaller arm spacing than the air-cooled sample. This was due to the increased cooling rate of the quenched sample.

### 5.2.8 Grain Size Analysis of Bi-Sn Alloy

Etching the Bi-Sn specimens revealed the lamellar structure of the eutectic, but defining the grain boundaries proved to be more challenging. Typically, a polarizing lens could be used with the optical microscope to examine the grain structure of the sample. Grains of different crystal orientations would reflect or scatter different wavelengths of light, thus revealing the grains in the microstructure. Figure 5.29 shows the microstructure of the Bi-Sn melt solidified by cooling in air in high-gravity viewed in polarized light using the Nikon LV100 optical microscope.

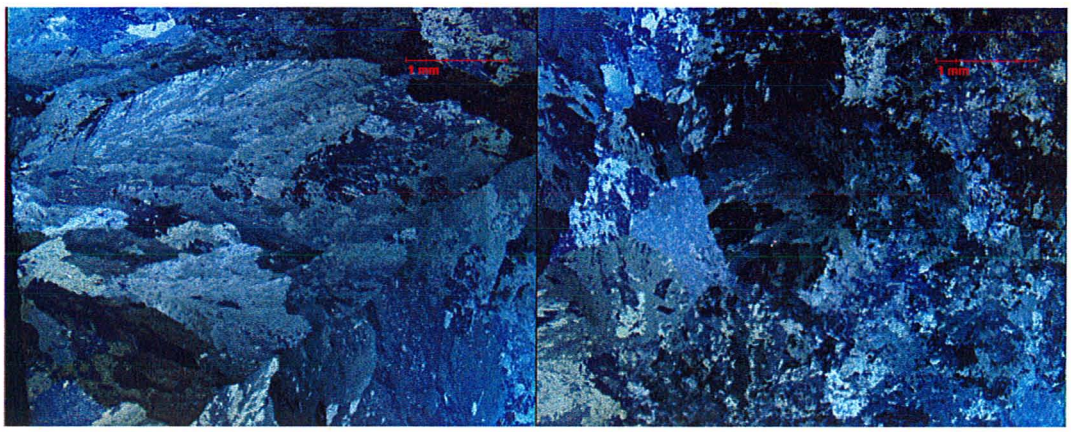

Figure 5.29: Bi-Sn eutectic, air-cooled in high-gravity, RZ plane, viewed with polarized light, high-radius (left) low-radius (right)

Since the microstructure of the Bi-Sn eutectic is lamellar, it has two different crystal structures: tetragonal and rhombohedral. Unfortunately, there were too many fluctuations in light intensity to distinguish a single grain. Qualitatively speaking, the microstructure shown in the left image of Figure 5.29 appears to be columnar whereas that shown in the right appears to be more equiaxed. Figure 5.30 shows the microstructure of the normal gravity Bi-Sn sample viewed with polarized light.

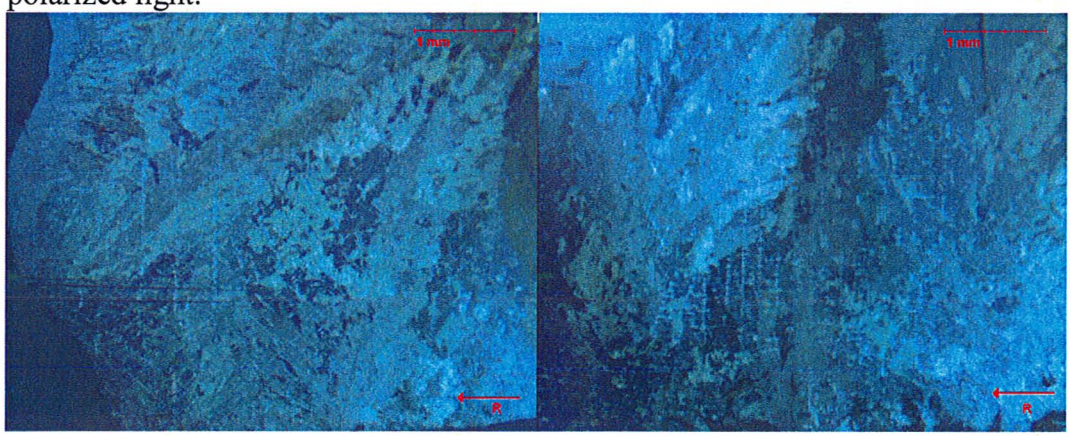

Figure 5.30: Bi-Sn eutectic, air cooled in normal gravity, RZ plane, viewed with polarized light - high-radius (left) low-radius (right)

The normal gravity sample seen in Figure 5.30 is even more difficult to quantify in terms of grain properties. Therefore, the grain properties were studied on the commercially-pure Sn and the Sn-Cu samples instead.

## 5.3 Studies of Commercially-Pure Sn

### 5.3.1 Solidification Conditions of Sn Cooled in Air

Before the fourth capsule disc was made, another procedure was used to estimate the cooling rate of the sample during solidification. This was done by leaving the thermocouple in the capsule during cooling in normal gravity, and measuring the temperature at 30 s intervals. Simultaneously, the surface temperature of the chamber was measured with the infrared thermometer, also at 30 s intervals. During spinning, the thermocouple was removed from the capsule, and the temperature of the chamber surface was measured by using the infrared thermometer. The temperature-time graphs for the capsule and for the chamber surface in normal gravity, and for the chamber surface in high-gravity, are shown in Figure 5.31.

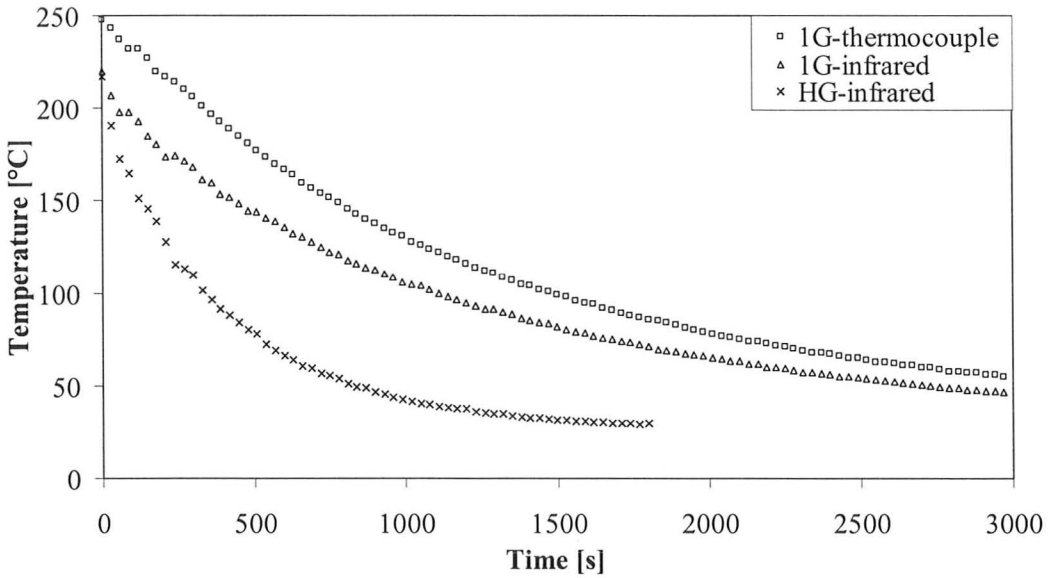


Figure 5.31: Temperature-time graphs for air-cooled Sn, on the chamber surface in high-gravity (HG), and inside the capsule and on the chamber surface in normal gravity (1G)

A correlation was deduced between the chamber surface temperature and the difference in temperature between the chamber surface and the capsule during in normal gravity. This correlation was used to determine the temperature of the chamber surface during spinning and thus to estimate the melt temperature in high-gravity. Figure 5.32 shows a graph correlating the temperature of the chamber surface, $T_S$, to the difference in temperature between the chamber surface and the capsule, $\Delta T$, during solidification in normal gravity.

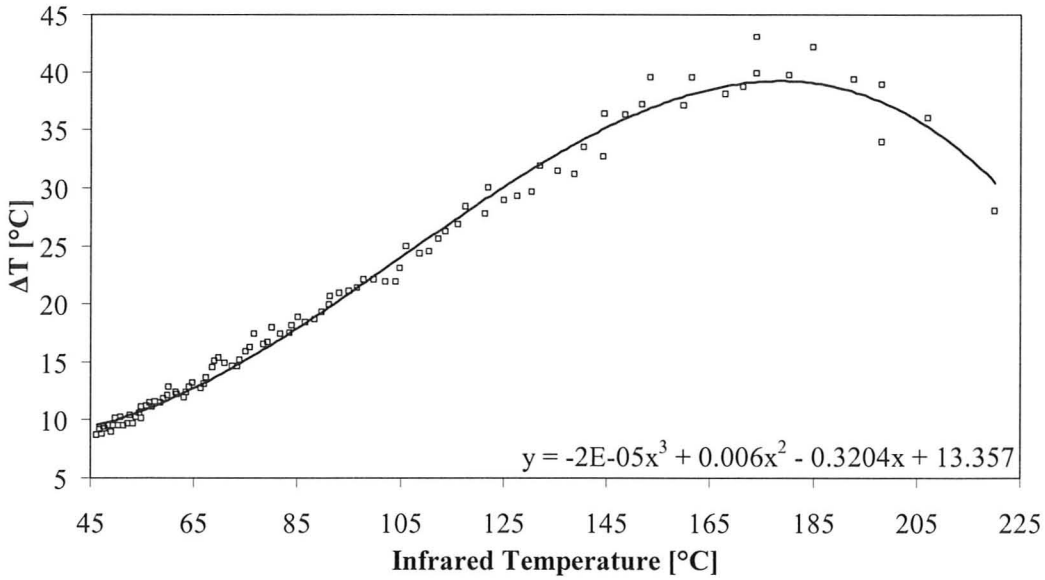


Figure 5.32: Calibration curve to correlate temperature of chamber surface to temperature of capsule

By using Microsoft Excel, a trend line with a cubic function was drawn through the data points to develop a fitting function given below:

$$\Delta T = -(2\times10^{-5})T_S^3 + (0.006)T_S^2 - 0.3204T_S + 13.357 \qquad (5.1)$$

where $\Delta T$ is the difference in temperature between the chamber surface and the capsule [°C] and $T_S$ is the temperature of the chamber surface [°C]. Figure 5.33 provides a comparison between the real temperature-time plot shown in Figure 5.31 and a theoretical temperature-time graph for estimating the capsule temperature in high-gravity.

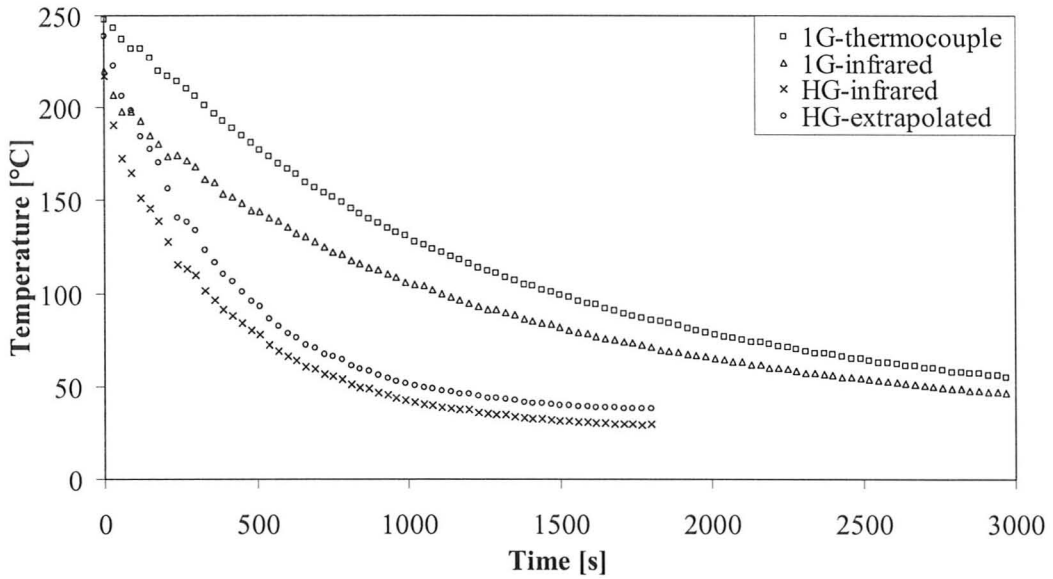


Figure 5.33: Temperature-time graphs of chamber surface and capsule during solidification in normal and high-gravity

The average cooling rate was determined from the slopes of the graphs from Figure 5.33 during normal and high-gravity between 0 s and 90 s. The slope was calculated from 232°C and 248°C for normal gravity, and from 199°C and 239°C for high-gravity. Therefore, the average cooling rate for the capsule was 0.13 K/s in high-gravity and 0.44 K/s in normal gravity indicating the melt had cooled faster in high-gravity compared to normal gravity. The faster cooling rate in high-gravity was due to the rapid motion of the spinning chamber surface increasing the heat transfer between the chamber surface and the surrounding air. This would be equivalent to increasing the air flow rate around the surface of the chamber which would increase the heat removal rate from the melt and thereby increase the crystal growth rate. To equalize the cooling rate of the high- and normal gravity samples, the air-shield was placed around the chamber to limit the heat transfer with the air in both conditions. The main disadvantage was that the surface temperature of the chamber could no longer be measured with the infrared thermometer.

By using the air-shield and the fourth capsule disc, two thermocouples were placed in the melt during solidification in normal gravity to measure temperature as a function of time. The results are shown in Figure 5.34.

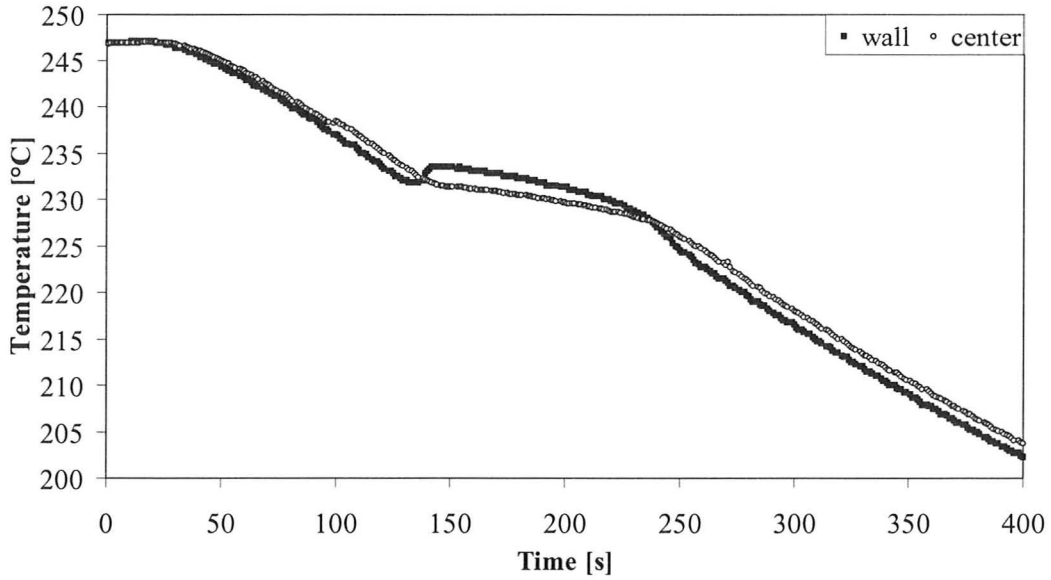


Figure 5.34: Temperature-time graphs for Sn, air-cooled in normal gravity

The average cooling rate was determined from the slope of the graph of the wall thermocouple in Figure 5.34. The slope was determined from 245°C and 235°C, and 44 s and 111 s, making the average cooling rate 0.15 K/s. Nucleation at the wall occurred at 132 s, and at the center thermocouple at 146 s. Therefore, it took 14 s for the solid-liquid interface to travel 10.16 mm, thus yielding a solid-liquid interface velocity of 0.72 mm/s. There was a maximum unstable temperature difference of 2°C between the two thermocouples at 146 s, making the maximum unstable thermal gradient 0.20 K/mm.

### 5.3.2 Sn Cooled in Air

After solidification, the high-gravity sample was cut, mounted, polished, and etched in the $HCl/HNO_3$/ethanol solution. The microstructure was examined with optical microscope (Nikon LV100) with polarized light and sensitive tint. Figure 5.35 to Figure 5.37 show the microstructure of the high-gravity Sn sample viewed in the Rθ, RZ, and Zθ planes, respectively.

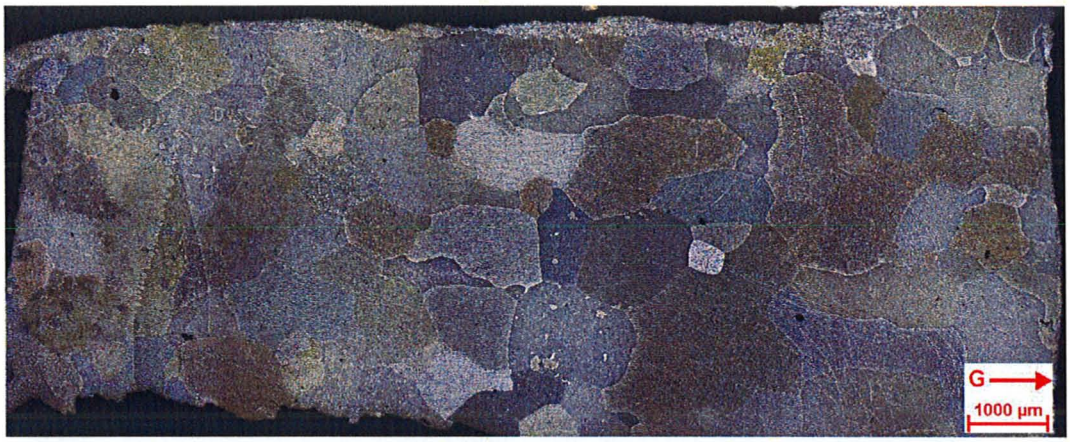


Figure 5.35: Sn, air-cooled in high-gravity, Rθ plane, etched, viewed with polarized light and sensitive tint


Figure 5.36: Sn, air-cooled in high gravity, RZ plane, etched, viewed with polarized light and sensitive tint

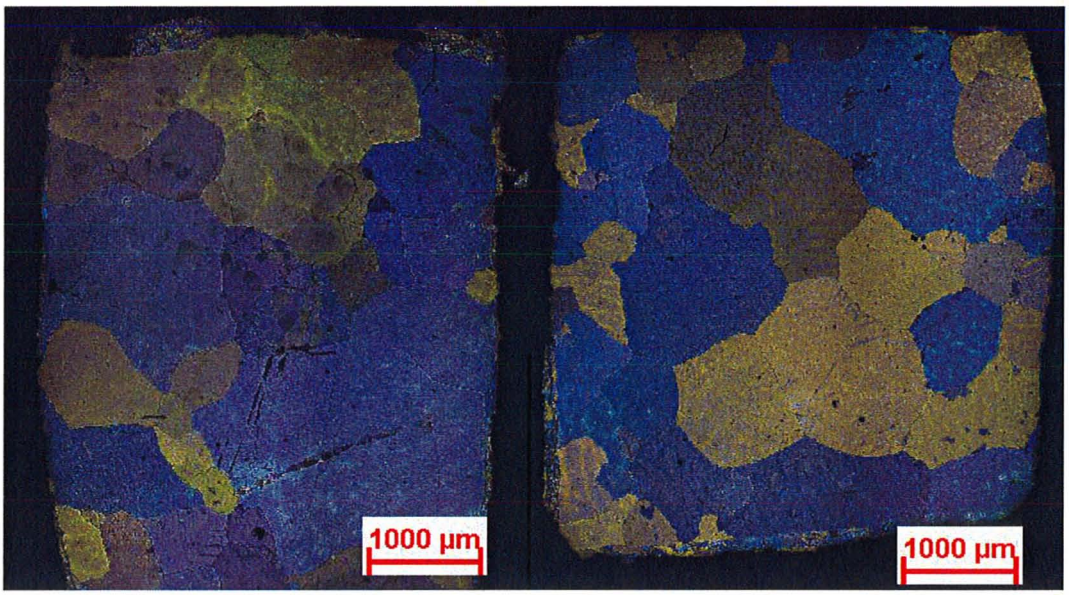


Figure 5.37: Sn, air-cooled in high-gravity, Zθ plane, etched, viewed with polarized light and sensitive tint - high-radius (left) and low-radius (right)

The high-gravity sample exhibits an equiaxed microstructure. The lack of a columnar zone indicates that convection occurred inhibiting the growth of columnar grains. Sn was also solidified in normal gravity to be compared with the high-gravity sample. Figure 5.38 to Figure 5.40 show microstructure of the sample obtained, and as viewed in the Rθ, RZ, and Zθ planes, respectively.


Figure 5.38: Sn, air-cooled in normal gravity, Rθ plane, etched, viewed with polarized light and sensitive tint

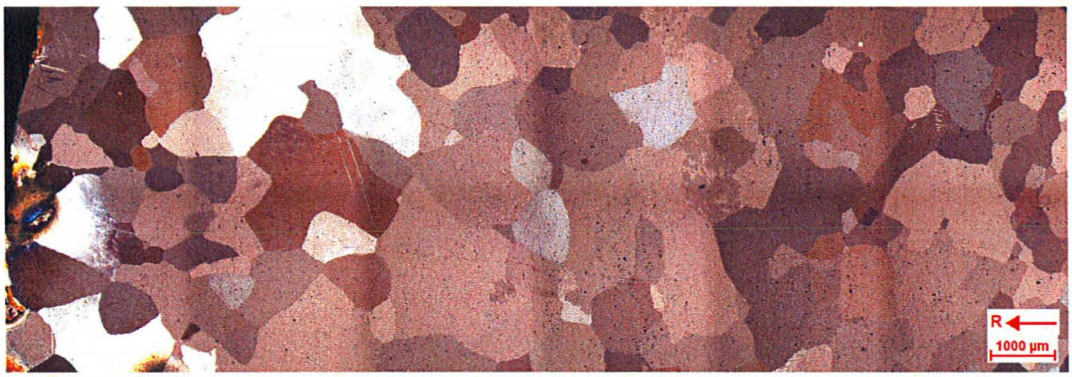


Figure 5.39: Sn, air-cooled in normal gravity, RZ plane, etched, viewed with polarized light and sensitive tint

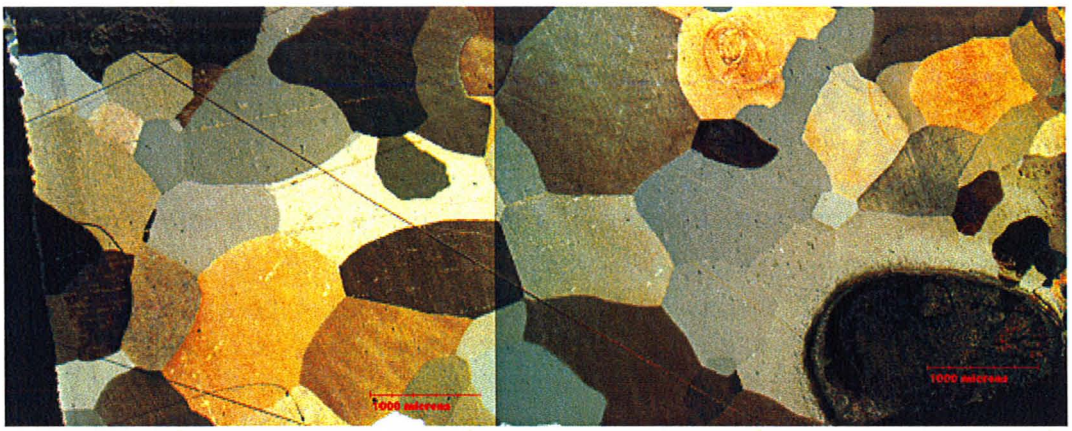

Figure 5.40: Sn, air-cooled in normal gravity, Zθ plane, etched, viewed with polarized light and sensitive tint

The microstructure of the normal gravity sample also consists of equiaxed grains. Since the Sn samples obtained by both high- and normal gravity solidification were hot-mounted, it is believed that the heat and the pressure from the hot-mounting process may have recrystallized the mounted specimens so that the columnar grains may have recrystallized into equiaxed grains. Evidence to support this theory is provided in Section 5.5.

### 5.3.3 Solidification Conditions of Sn Quenched in Water

Sn was also solidified by quenching the chamber containing the melt in cold water at ~15°C to increase the cooling rate of the melt. The temperature of the water increased which resulted in a cooling rate slower than quenching in ice-water, but faster than being cooled in air. Two thermocouples were placed in the melt during solidification to measure temperature against time. Figure 5.41 shows the temperature-time graphs of Sn being solidified by quenching in water in normal gravity.

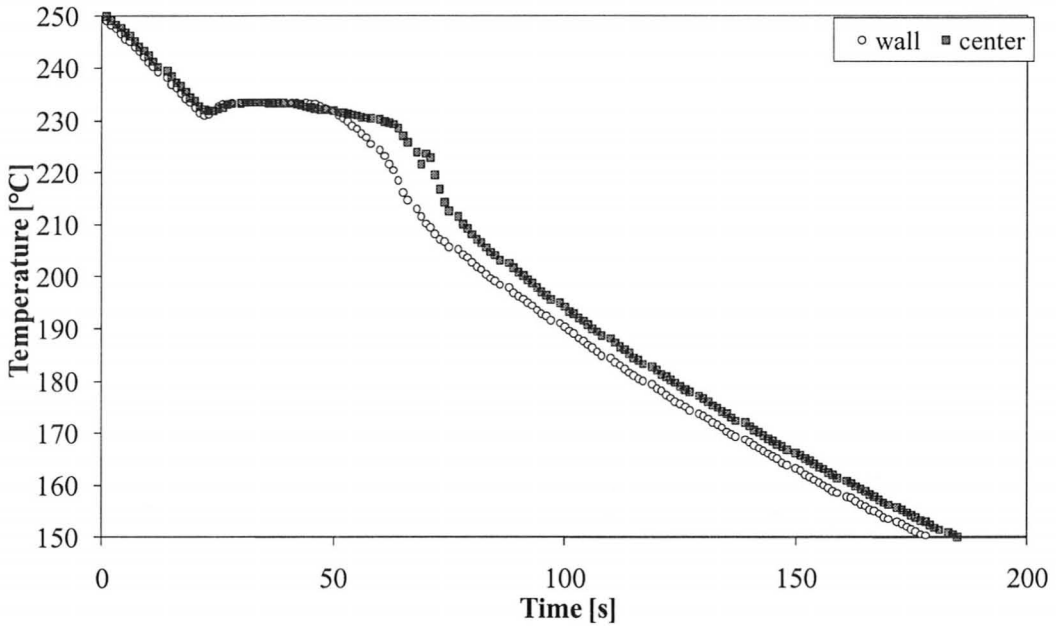


Figure 5.41: Temperature-time graphs of Sn, water-quenched in normal gravity

The average cooling rate was determined from the slope of the temperature-time graph from the wall thermocouple in Figure 5.41, taken between 250°C and 235°C and 0 s and 19 s, giving an average cooling rate of 0.82 K/s. Maximum undercooling occurred at the wall and center thermocouples at 22 s and 23 s, respectively so that the solid-liquid interface velocity of 10.16 mm/s. There was a maximum unstable temperature difference of 0.5 K at 25 s, giving a maximum unstable thermal gradient of 0.05 K/mm. As this unstable temperature difference was found at a time close to the completion of solidification, there may have been no Rayleigh-Bénard convection, but other types of convection and fluid motion may be present.

### 5.3.4 Sn Quenched in Water

Sn was placed into the capsule, melted, and resolidified under centrifugal acceleration. After spinning had stabilized, a bath of cold water at ~15°C was lifted to surround the chamber and quench it. The high-gravity sample was extracted, cut, cold-mounted, polished, and examined through an optical microscope with polarized light. Figure 5.42 to Figure 5.44 show the images for the high-gravity Sn sample, as seen in the Rθ, RZ, and Zθ planes, respectively.

Figure 5.42: Sn, water-quenched in high-gravity, Rθ plane, and viewed with polarized light

Figure 5.43: Sn, water-quenched in high-gravity, RZ plane, viewed with polarized light

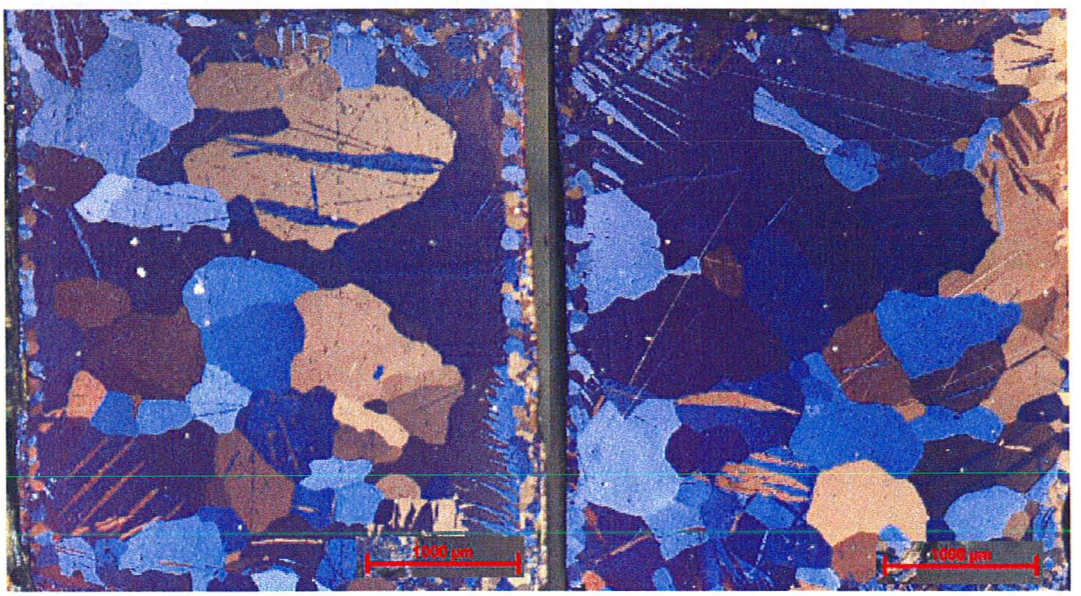

Figure 5.44: Sn, water-quenched in high-gravity, Zθ plane, viewed with polarized light - high-radius (left), low-radius (right)

The high-gravity sample appears to have large equiaxed grains with no presence of a columnar zone. This suggests that convection in the melt existed during quenching due to the increased gravity and impinged the growth of columnar grains. Sn was then solidified in normal gravity and the microstructures of the high- and normal gravity samples were compared. Figure 5.45 to Figure 5.47 show images for the normal gravity samples quenched in water viewed in the Rθ, RZ, and Zθ planes, respectively.

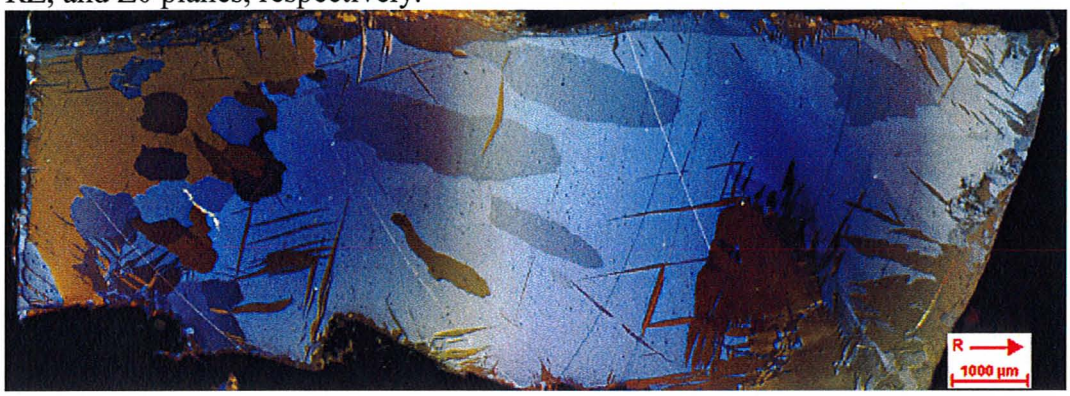


Figure 5.45: Sn, water-quenched in normal gravity, Rθ plane, unetched, viewed with polarized light

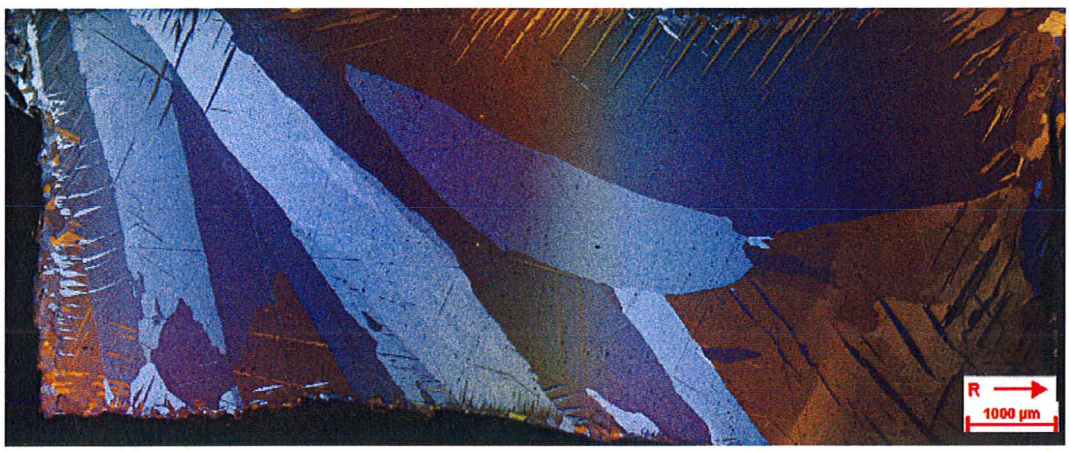


Figure 5.46: Sn, water-quenched in normal gravity, RZ plane, unetched, viewed with polarized light

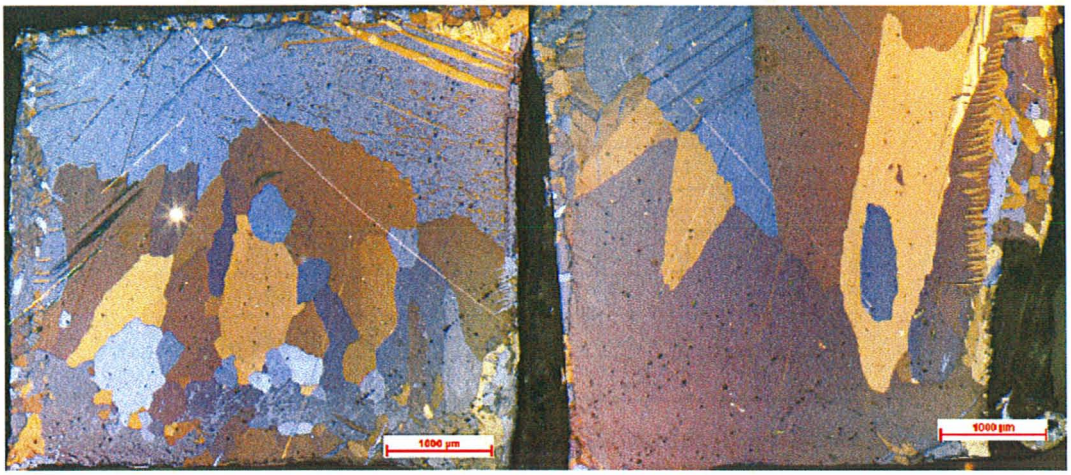


Figure 5.47: Sn, water-quenched in normal gravity, Zθ plane, viewed with polarized light - low-radius (left), high-radius (right)

The figures show that the microstructure of the normal gravity sample is very different from the microstructure of the high-gravity sample. The high-radius areas show large and columnar grains and the low-radius areas smaller, equiaxed grains seen in typical solidification castings.

## 5.4 Studies of the Sn-Cu Alloys

During the course of this study, and after two experiments on solidification with the copper pipe, it was determined that the microstructure was changing due to the Cu content of the sample. As a result, the solidification of the $Sn_{99.7}Cu_{0.3}$ alloy was done unintentionally.

### 5.4.1 Chemical Composition Analysis

The chemical composition of the sample was determined by using ICP analysis. The composition of the Sn, as received from the supplier, is listed in Table 5.1. The composition of sample after several experiments without the copper pipe is shown in Table 5.2. Finally, the composition of the sample after several experiments with the copper pipe is listed in Table 5.3.

Table 5.1: ICP analysis Sn, as received from supplier

| Element | PPM | Dilution Factor | Sample Weight | Weight % |
|---|---|---|---|---|
| Al | 0.0062 | 100.00 | 0.1054 | **0.001** |
| Bi | 0.0367 | 100.00 | 0.1054 | **0.003** |
| Cu | 0.0742 | 100.00 | 0.1054 | **0.007** |
| Fe | 0.1142 | 100.00 | 0.1054 | **0.011** |
| Pb | 0.4316 | 100.00 | 0.1054 | **0.041** |
| Sb | 0.1154 | 100.00 | 0.1054 | **0.011** |

Table 5.2: ICP analysis of Sn after several experiments without the copper pipe

| Element | PPM | Dilution Factor | Sample Weight | Weight % |
|---|---|---|---|---|
| Al | 0.0083 | 100.00 | 0.1107 | **0.001** |
| Bi | 0.0492 | 100.00 | 0.1107 | **0.004** |
| Cu | 0.0515 | 100.00 | 0.1107 | **0.005** |
| Fe | 0.0558 | 100.00 | 0.1107 | **0.005** |
| Pb | 0.4407 | 100.00 | 0.1107 | **0.040** |
| Sb | 0.2871 | 100.00 | 0.1107 | **0.026** |

Table 5.3: ICP analysis of sample after several experiments with the copper pipe

| Element | Sample 1 [wt%] | Sample 2 [wt%] | Sample 3 [wt%] | Sample 4 [wt%] |
|---|---|---|---|---|
| **Cu** | 0.323 | 0.33 | 0.332 | 0.337 |
| **Fe** | 0.01 | 0.01 | 0.001 | 0.001 |
| **Pb** | 0.008 | 0.009 | 0.011 | 0.012 |
| **Zn** | 0.009 | 0.005 | 0.004 | 0.01 |

The ICP analyses confirm that there was an increase in concentration of Cu in the Sn sample. In addition, the Al concentration of the sample did not increase with respect to the as-received sample. This confirms that the aluminum-oxide layer was able to prevent diffusion of Al into the sample.

### 5.4.2 Sn with Dissolved Cu from the Cu Pipe

A copper pipe was placed in the center of the capsule cavity. The capsule was then filled with Sn melt and solidified by quenching in water in both high- and normal gravity. Because the sample was still primarily composed of Sn, it was assumed that the solidification conditions were similar to those determined by Figure 5.41. The samples were removed from capsule, cut, hot-mounted, and polished. Figure 5.48 and Figure 5.49 show the microstructures of Sn samples solidified with a copper pipe in the Rθ plane, in high- and normal gravity, respectively.


Figure 5.48: Sn with Cu wall, water-quenched in high-gravity, Rθ plane, viewed with polarized light and sensitive tint


Figure 5.49: Sn with Cu wall, water-quenched in normal gravity, Rθ plane, viewed with polarized light and sensitive tint

The microstructure from Figure 5.48 shows a course dendritic structure whereas the one shown in Figure 5.49 exhibits a fine dendritic structure. Grains of the normal gravity sample are also larger than those of the high-gravity sample. The copper pipe divided the container two parts, the high-radius part and the low-radius part. In the high-gravity samples, there are two distinct levels of centrifugal acceleration, but the presence of the copper pipe does not seem to have affected the microstructure in terms of grain size within the sample.

### 5.4.3 $Sn_{99.7}Cu_{0.3}$ Alloy Water-Quenched

After discovering the unexpected influence of the dissolution of Cu from the copper pipe into the Sn melt, its use was discontinued. However, the metal was reused, not knowing that the material had been contaminated. The sample was solidified by quenching the chamber in cold water at ~15°C so that the cooling conditions would be similar to those shown in Figure 5.41. Figure 5.50 to Figure 5.52 show micrographs of the high-gravity sample in the high- and low-radius areas viewed in the Rθ, RZ, and Zθ planes, respectively.

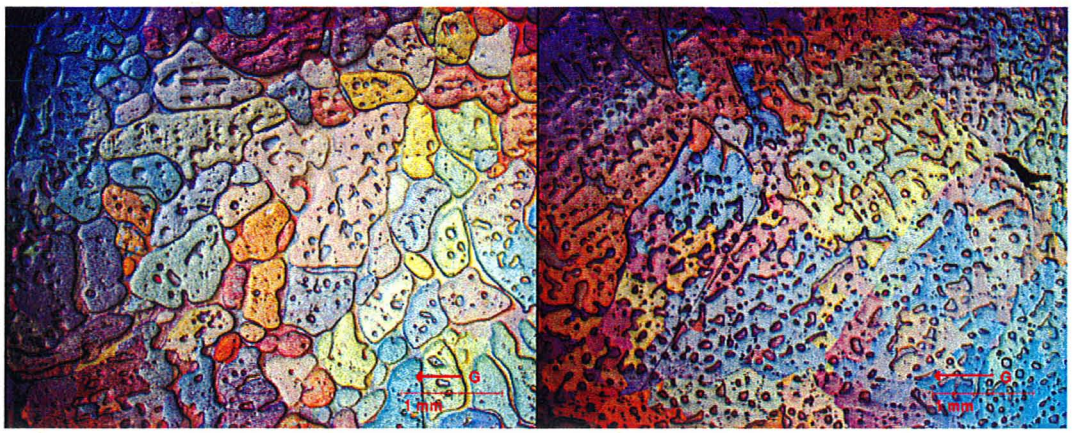

Figure 5.50: $Sn_{99.7}Cu_{0.3}$, water-quenched in high-gravity, Rθ plane, unetched, viewed with polarized light and sensitive tint - high-radius (left), low-radius (right)

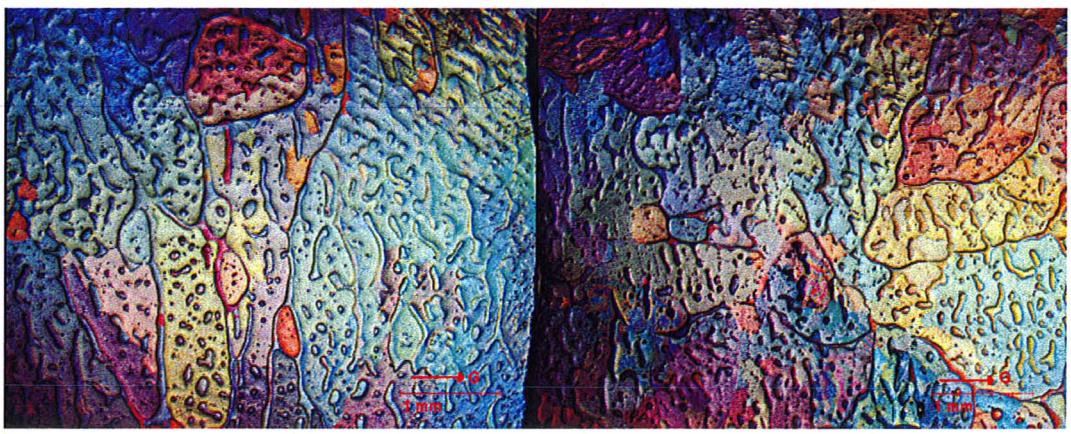

Figure 5.51: $Sn_{99.7}Cu_{0.3}$, water-quenched in high-gravity, RZ plane, unetched, viewed with polarized light and sensitive tint - high-radius (left), low-radius (right)

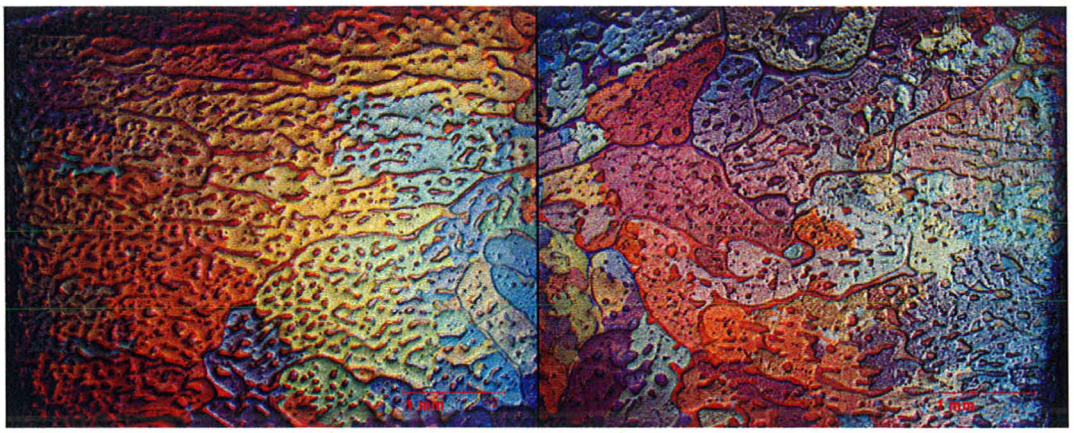

Figure 5.52: $Sn_{99.7}Cu_{0.3}$, water-quenched in high-gravity, Zθ plane, unetched, viewed with polarized light and sensitive tint - high-radius (left), low-radius (right)

The high-gravity sample appears to have a cellular microstructure with evidence of entrapped liquid during solidification. Figure 5.53 to Figure 5.55 show the micrographs from the normal gravity $Sn_{99.7}Cu_{0.3}$ sample in the high- and low-radius areas viewed in the Rθ, RZ, and Zθ planes, respectively.

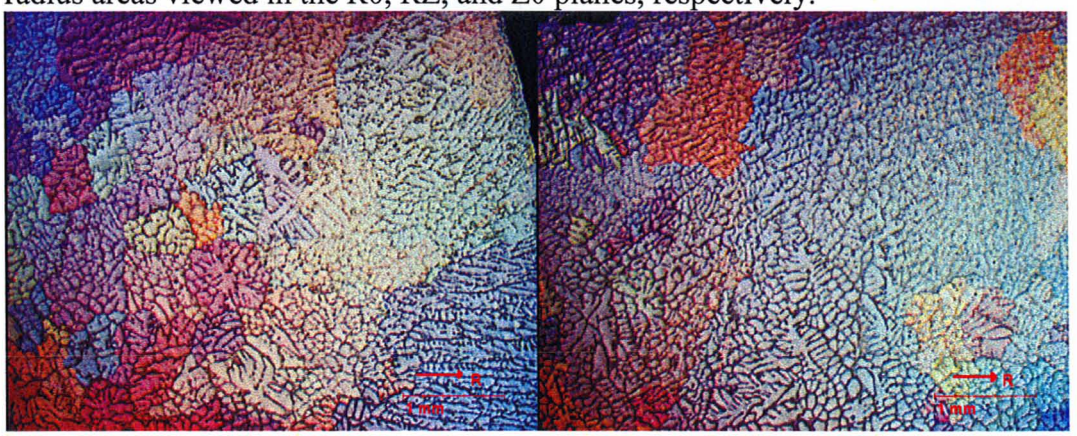

Figure 5.53: $Sn_{99.7}Cu_{0.3}$, water-quenched in normal gravity, Rθ plane, unetched, viewed with polarized light and sensitive tint - high-radius (left), low-radius (right)

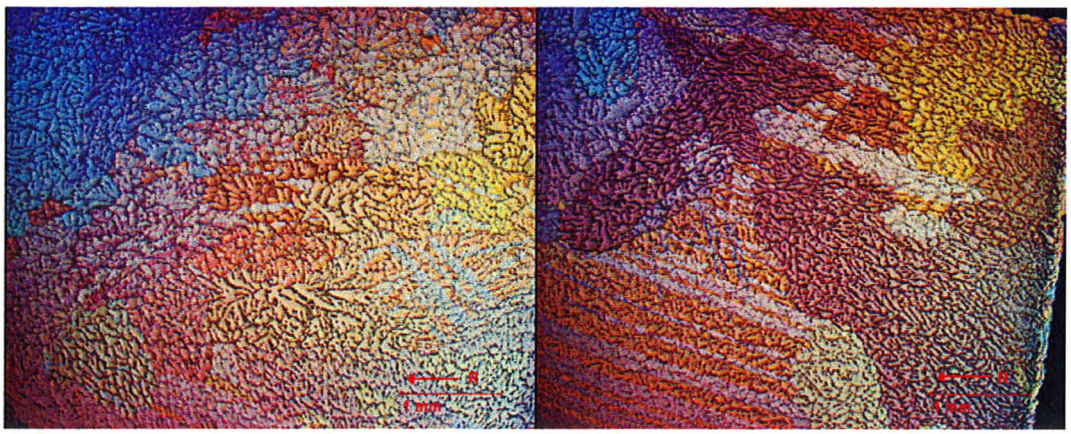

Figure 5.54: $Sn_{99.7}Cu_{0.3}$, water-quenched in normal gravity, RZ plane, unetched, viewed with polarized light and sensitive tint - high-radius (left), low-radius (right)

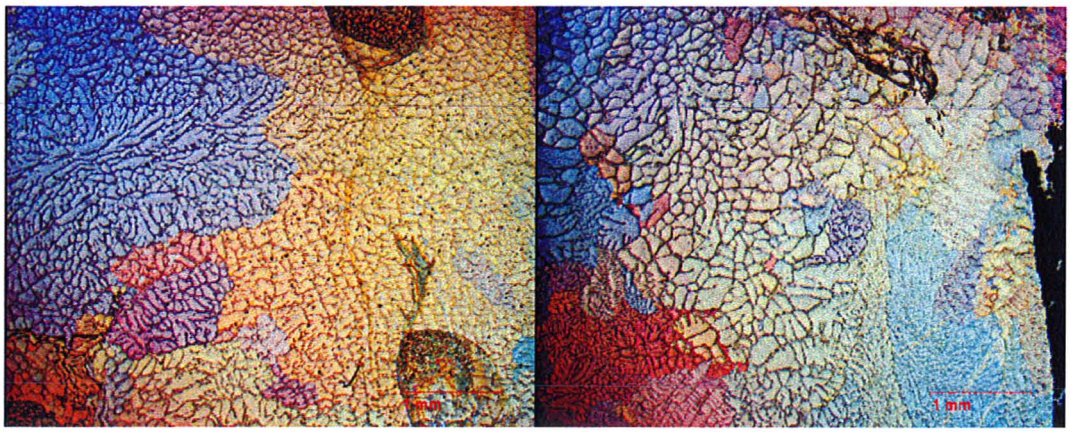

Figure 5.55: $Sn_{99.7}Cu_{0.3}$, water-quenched in normal gravity, Zθ plane, unetched, viewed with polarized light and sensitive tint - high-radius (left), low-radius (right)

Figure 5.53 to Figure 5.55 show that the normal gravity sample appears to have a dendritic microstructure. There is no evidence of entrapped liquid and the grains are larger than in the high-gravity sample.

## 5.5 Recrystallization of Sn

Before it was realized that the recrystallization temperature of Sn was relatively low, the Sn specimens were hot-mounted by heating each specimen in Lucite powder at 180°C at a pressure of 3000 psi for 12 min and then cooled for 5 min. Generally a material's recrystallization temperature is between 0.4 and 0.7 of its absolute melting temperature. Therefore, the recrystallization temperature of Sn would be between 25°C and 80°C, but alloying elements appear to increase the recrystallization temperature. The Sn specimens were therefore cold-mounted, but this still produced some heat, as a thermocouple placed in the epoxy

resin during the cold mounting process indicated that in the mixing process of the epoxy resin, the temperature reached as high as 35°C and remained so for several minutes. To ensure that the cold-mounting process did not recrystallize the specimens, three specimens taken from the same high-gravity sample were carefully cut with the precision cutter. One specimen was hot-mounted, one cold-mounted, and one held in place by using the specimen holder described Section 4.2.7. To ensure that the heat generated by the friction of the polishing process did not recrystallize the specimens, the specimens were polished at the lowest possible force setting. Figure 5.56 shows a comparison of the microstructure of the Sn sample solidified by cooling in air in high-gravity, hot-mounted, cold-mounted, and pre-mounted.

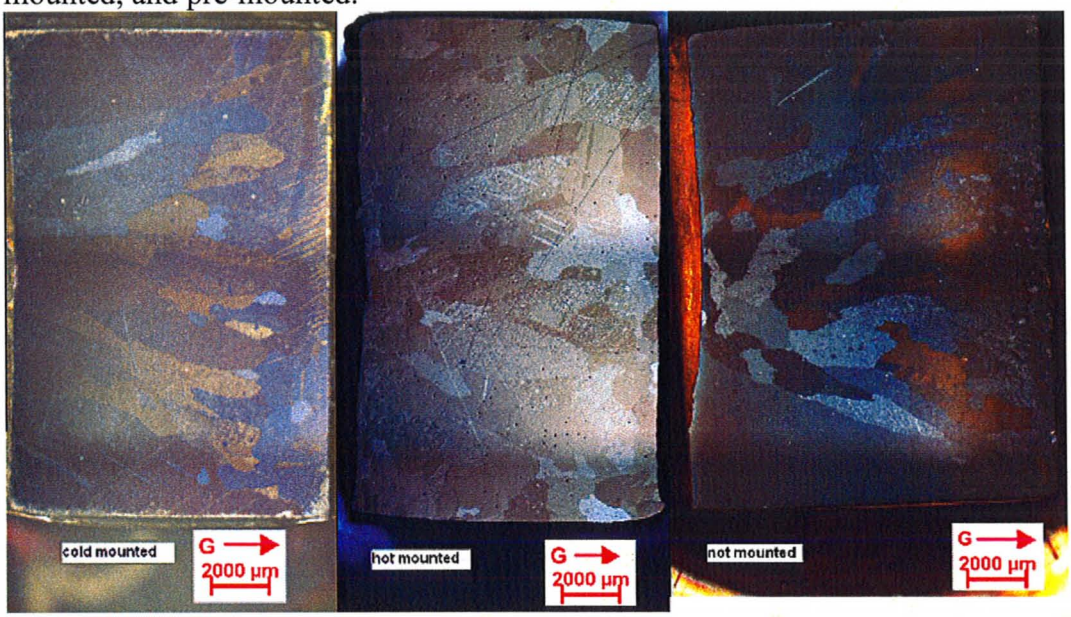


Figure 5.56: Comparison of Sn microstructure, air-cooled in high-gravity, cold-mounted (left), hot-mounted (center), and pre-mounted (right)

The microstructures of the cold-mounted and pre-mounted specimens are similar and both have large columnar grains. In contrast, the hot-mounted specimen has smaller equiaxed grains. Therefore, it does not appear that the cold-mounting process did not raise the temperature of the specimen enough to recrystallize it and thereby alter its microstructure.

# CHAPTER 6: ANALYSIS

## 6.1 Microstructure Analysis

### 6.1.1 Eutectic Spacing of the Bi-Sn Alloys

By using the Nikon LV100 optical microscope at ×1000 magnification, several images of each specimen were obtained in the Rθ and RZ planes along its radius. The eutectic spacing at five random points was measured for each image and plotted against the radius. Therefore, it could be determined if there was any correlation between eutectic spacing and radius and hence the level of centrifugal acceleration. Figure 6.1 shows a plot of the eutectic spacing against the radius for the high-gravity sample in the Rθ and RZ planes.

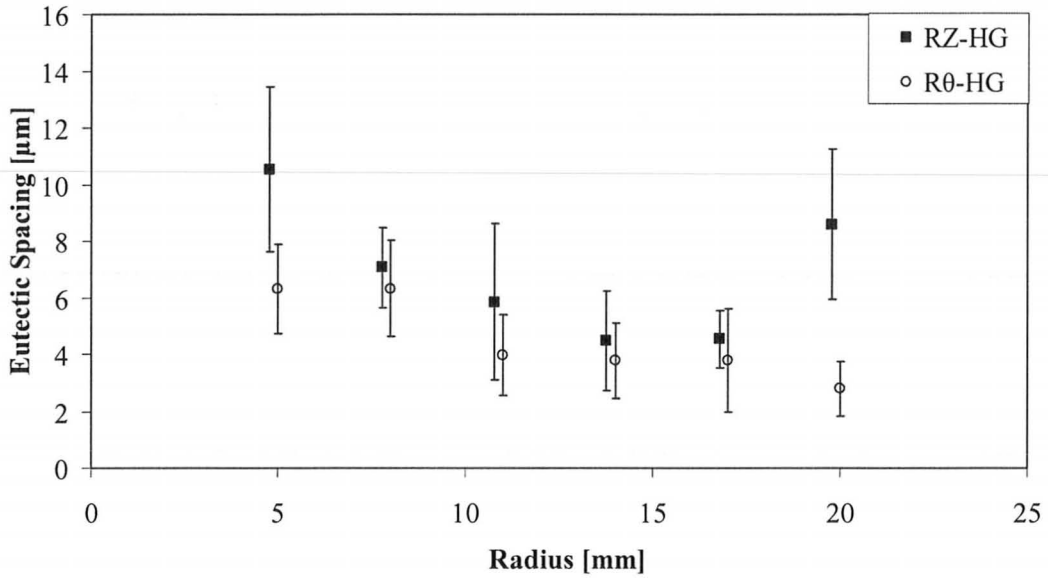


Figure 6.1: Plot of the eutectic spacing against radius for Bi-Sn eutectic, air-cooled in high-gravity

In Figure 6.1, the eutectic spacing of the high-gravity sample appears to be decreasing with respect to radius in the Rθ plane as well as for the RZ plane up until 20 mm. However, it cannot be conclusively stated that this trend would continue for higher levels of radii. The average eutectic spacing was determined to be 5.60 ± 2.70 µm. Figure 6.2 shows a plot of the eutectic spacing against the radius for the normal gravity sample.

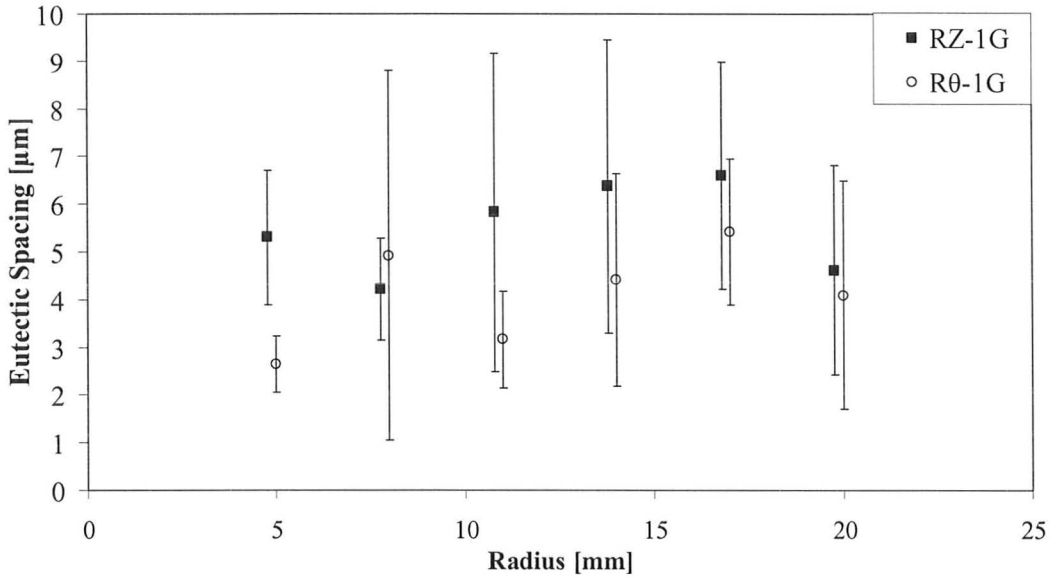


Figure 6.2: Plot of the eutectic spacing against radius for Bi-Sn eutectic, air-cooled in normal gravity

In Figure 6.2, the eutectic spacing in the normal gravity sample does not appear to be affected by the radius. The average eutectic spacing was determined to be 4.82 ± 2.37 μm. The eutectic spacing was also measured for the samples solidified by quenching in ice-water slurry. Ten random points in each image along the sample's radius were measured. Figure 6.3 shows a plot of the eutectic spacing against the radius for the high-gravity sample.

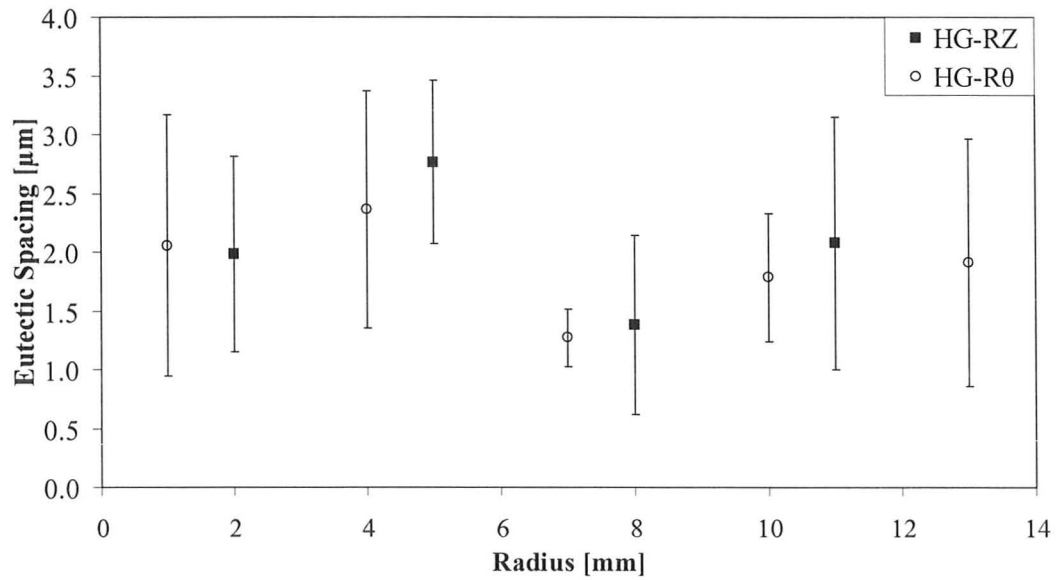


Figure 6.3: Plot of the eutectic spacing against radius for Bi-Sn eutectic, ice-water quenched in high-gravity

In Figure 6.3, the eutectic spacing of the ice-water quenched high-gravity sample does not appear to be affected by the radius. The average eutectic spacing was determined to be 1.95 ± 0.93 μm. Figure 6.4 shows a plot of the eutectic spacing against the radius of the normal gravity sample.

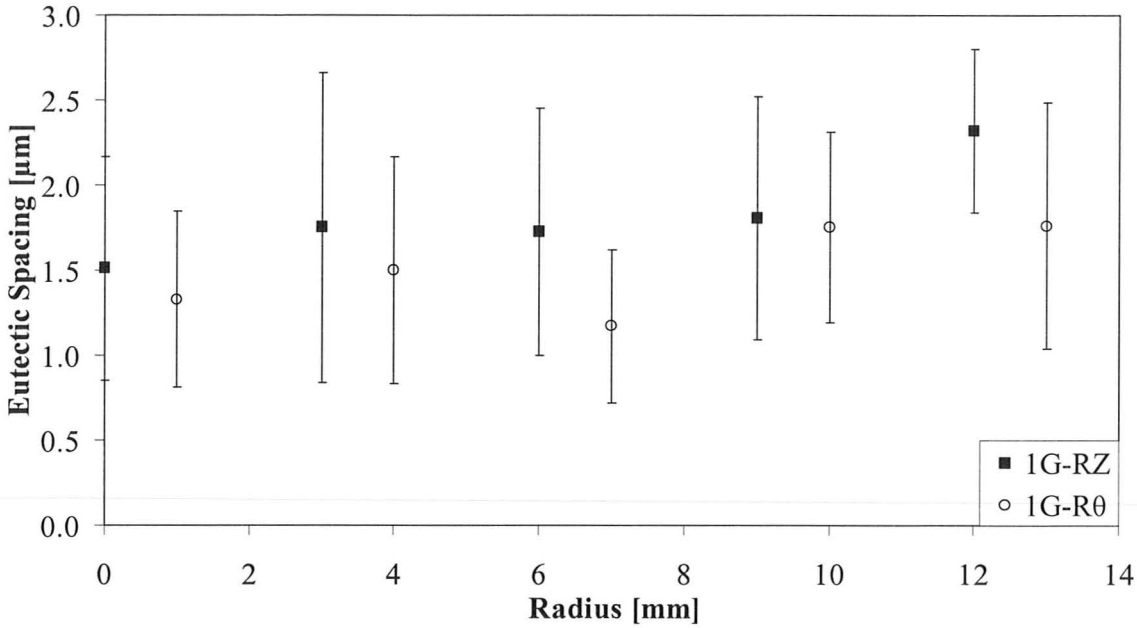


Figure 6.4: Plot of the eutectic spacing against radius for Bi-Sn eutectic, ice-water quenched in normal gravity

The eutectic spacing in the ice-water quenched normal gravity sample does not appear to be dependent on the radius of the sample. The average eutectic spacing was determined to be 1.66 ± 0.69 μm.

6.1.2 Grain Size Analysis of Air-Cooled Sn

The grain size of each grain in the Sn specimens was measured in terms of the grain length as opposed to grain area. The grain lengths, parallel to the direction of heat flow, were measured for each Sn specimen and plotted as histograms. Figure 6.5 and Figure 6.6 show the histograms that compare the grain sizes of high- and normal gravity samples in the Rθ and RZ planes, respectively. The histograms show the percentage rather than absolute number because the sample size taken from each specimen differed. The percentage was obtained by dividing the number of grains of a size-range by the total number of grains in the sample in that plane.

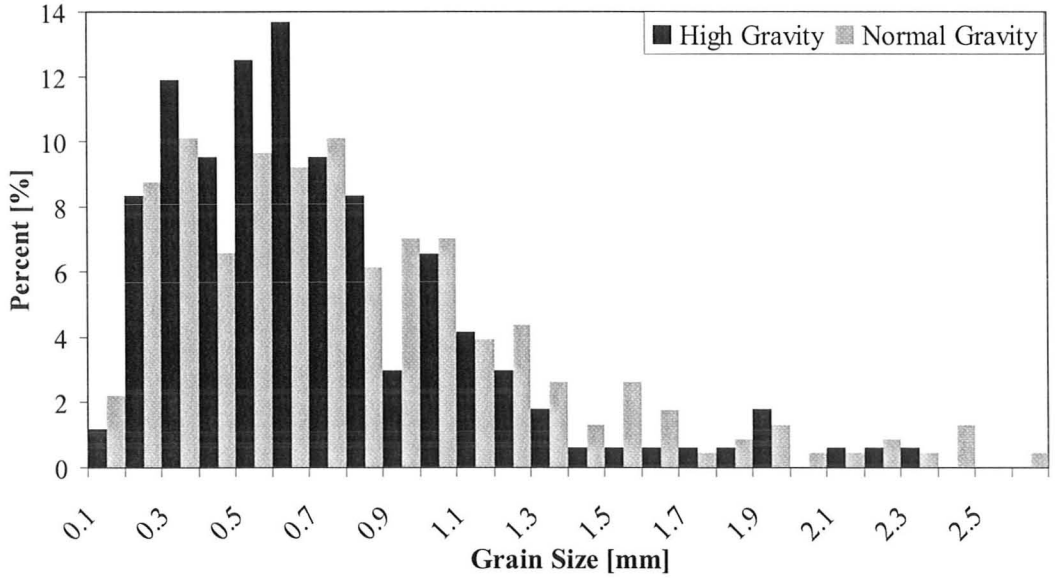


Figure 6.5: Grain size histogram of air-cooled Sn in the Rθ plane

Figure 6.5 shows a normal distribution of grain size with a mean length of about 0.6 mm. The high-gravity sample has a higher percentage of grains that is equal or less than the mean length than the normal gravity sample.

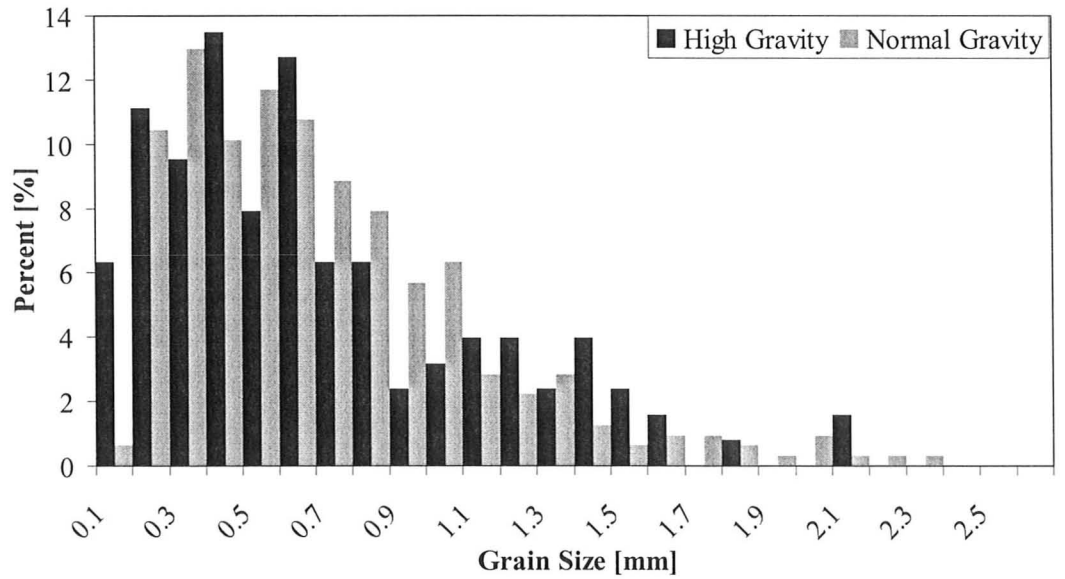


Figure 6.6: Grain size histogram of air-cooled Sn in the RZ plane

Figure 6.6 also shows a relatively normal distribution with a mean length of 0.4 mm. The high-gravity sample shows a higher percentage of grains that are equal to or smaller than the mean grain length. The grain lengths for the high- and normal gravity samples were also measured for the microstructure in the Zθ plane.

Since the direction of heat extraction is perpendicular to the image plane, the horizontal length of the grain was measured instead. Figure 6.3 shows the histogram for high- and normal gravity sample in the Zθ plane.

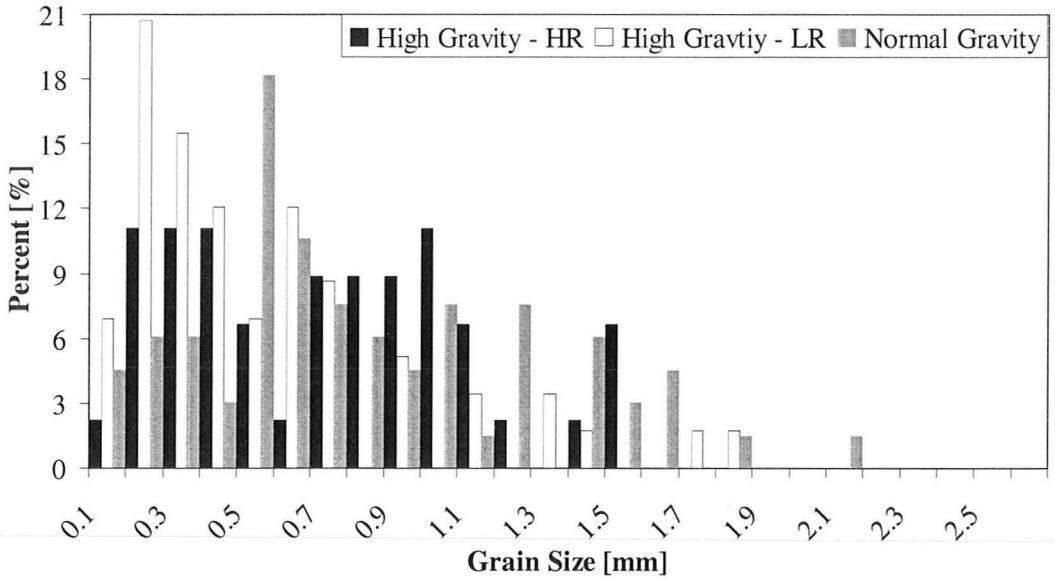


Figure 6.7: Grain size histogram of air-cooled Sn in the Zθ plane

In Figure 6.7, the high-gravity sample in both the high-radius (HR) and low-radius (LR) areas of the Zθ plane shows a higher percentage of grains smaller than 0.4 mm compared to the normal gravity sample. However, when comparing the high-radius area to the low-radius area, the low-radius area shows a higher number of small grains than the high-radius zone. The microstructure was also analyzed by counting the number of grains in a micrograph image and plotting the number of grains per unit area against the radius. Figure 6.8 shows the graph of number of grains per unit area plotted against the radius for air-cooled Sn in the Rθ plane.

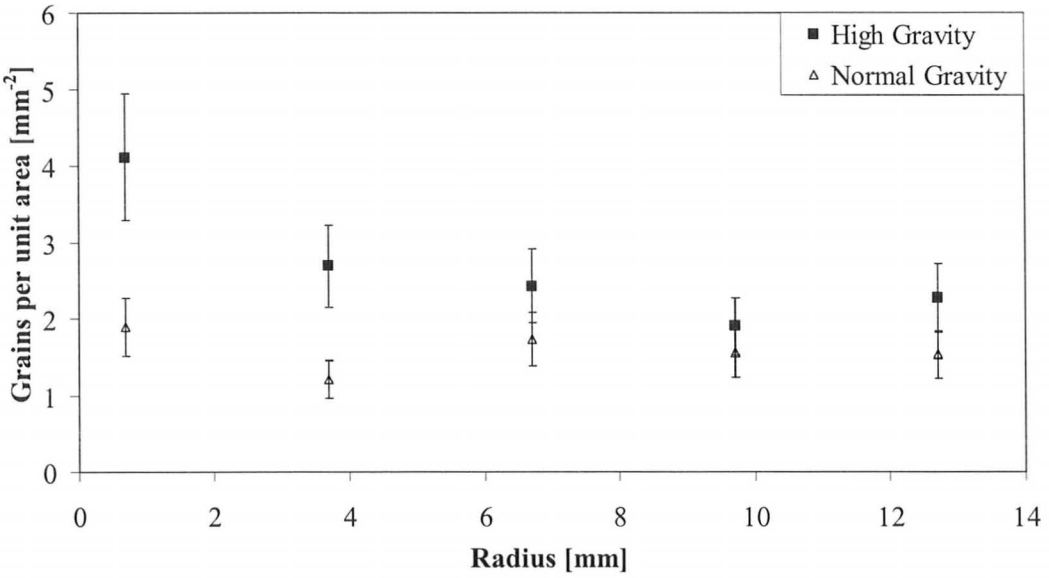


Figure 6.8: Plot of the grains per unit area against the radius for air-cooled Sn in the Rθ plane

Figure 6.8 shows that the high-gravity sample has more grains per unit area than the normal gravity sample. In addition, the high-gravity sample shows that there are more grains per unit area in the low-radius area than the high-radius area. The number of grains was counted for the RZ plane as well and the results are shown in Figure 6.9.

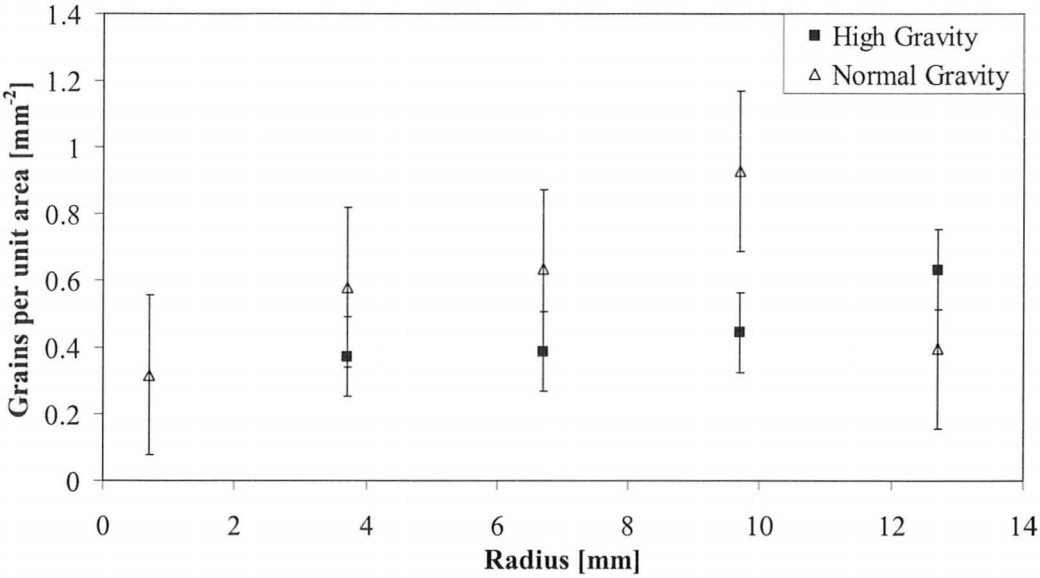


Figure 6.9: Plot of the grains per unit area against radius in the RZ plane for air-cooled Sn

Counter to the data from the histogram in the RZ plane, the normal gravity sample has a higher number of grains per unit area than the high-gravity sample, except for in the high-radius area.

### 6.1.3 Grain Size Analysis of Water-Quenched Sn

The grain lengths of the microstructure formed in the high- and normal gravity samples in the Rθ plane for water-quenched Sn was measured in the direction parallel to the heat flow. Figure 6.10 shows the histogram of grain length in the Rθ plane.

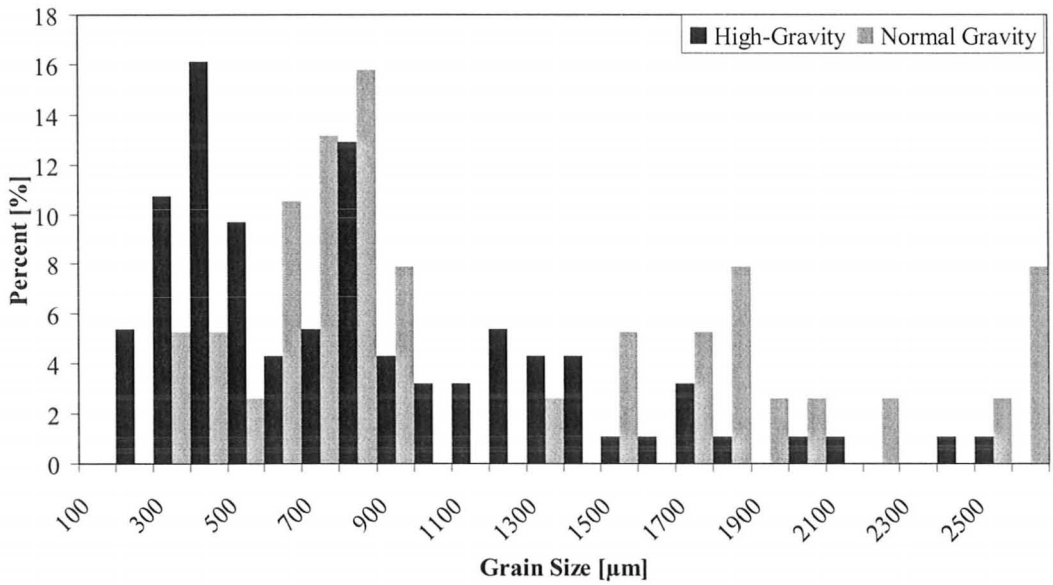


Figure 6.10: Grain size histogram of water-quenched Sn in Rθ plane

From Figure 6.10, the mean grain size was 400 μm for the high-gravity sample and 800 μm for the normal gravity sample. The high-gravity sample had a higher percentage of small grains less than 500 μm compared with the normal gravity sample in the Rθ plane. To analyze the samples in the RZ plane, the number of grains per unit area were determined for each sample and plotted as a function of radius. Figure 6.11 shows the number of grains per unit area plotted against the radius for the RZ plane.

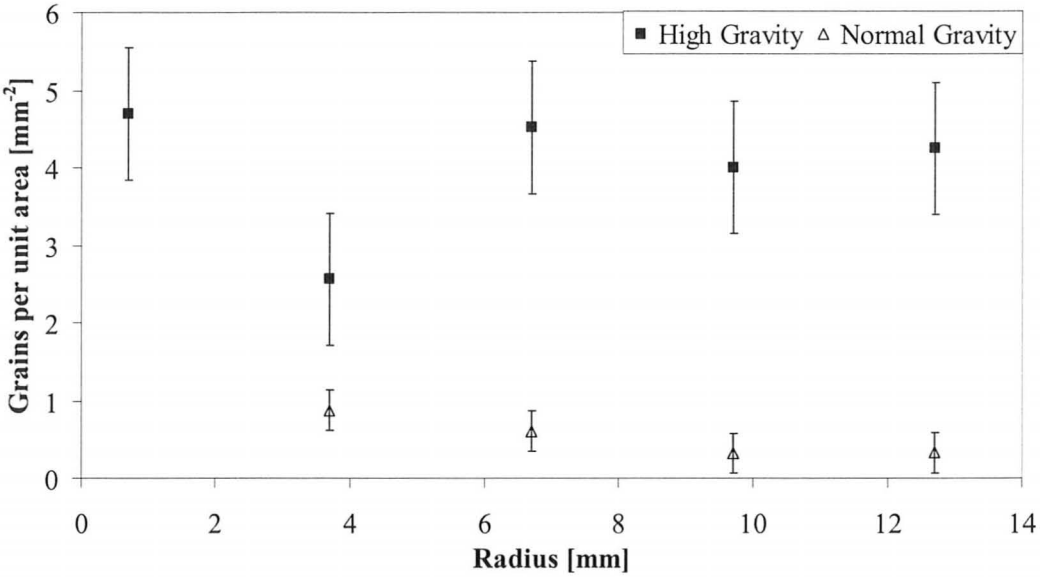


Figure 6.11: Plot of the grains per unit area against radius for water-quenched Sn in the RZ plane

From Figure 6.11, the number of grains per unit area in the high-gravity sample exceeds that of the normal gravity sample. This suggests that the grains formed in the high-gravity sample are smaller than those formed in the normal gravity sample. This is the opposite when compared to the RZ plane in the air-cooled Sn samples.

### 6.1.4 Grain Size Analysis of $Sn_{99.7}Cu_{0.3}$

The grains from the microstructures of the $Sn_{99.7}Cu_{0.3}$ samples were also measured. Figure 6.12 to Figure 6.14 show the comparative histograms of the high- and normal gravity Sn-Cu samples in the Rθ, RZ, and Zθ planes, respectively. For the Rθ and RZ planes, the grain length was measured in the direction parallel to heat flow. In the Zθ plane, the grain length was measured horizontally.

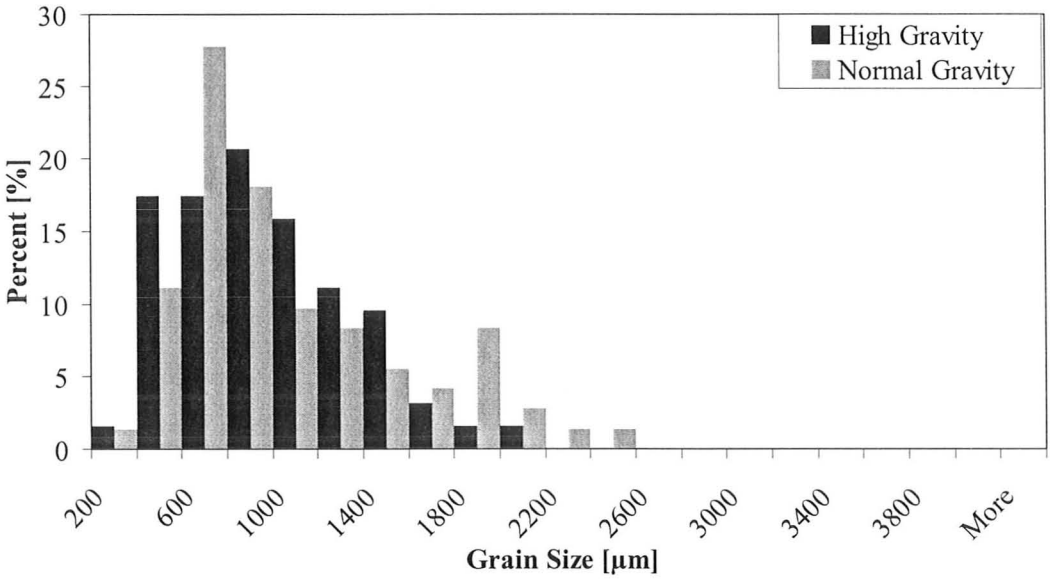


Figure 6.12: Grain size histogram of water-quenched $Sn_{99.7}Cu_{0.3}$ in the Rθ plane

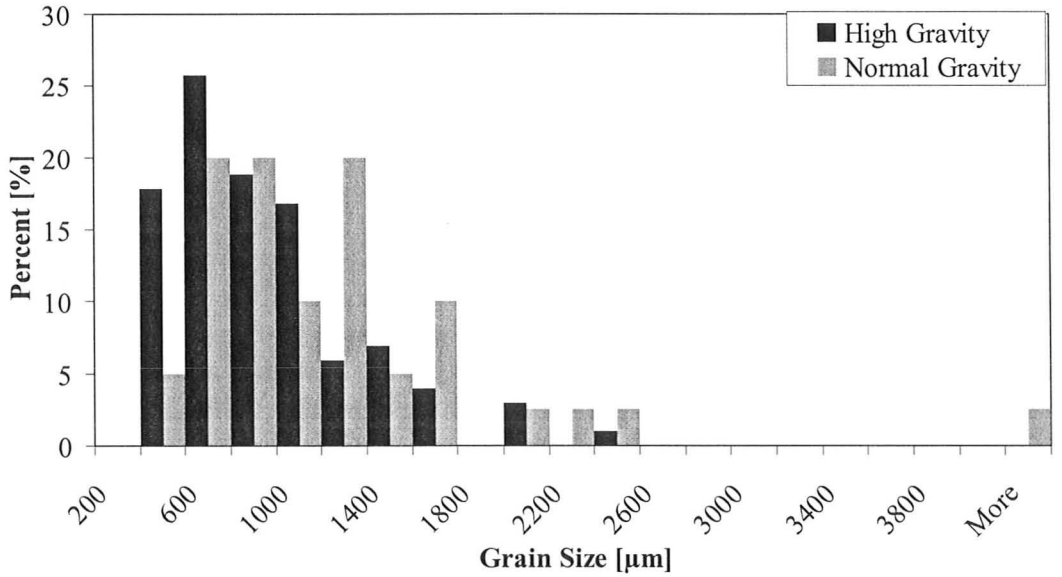


Figure 6.13: Grain size histogram of water-quenched $Sn_{99.7}Cu_{0.3}$ in the RZ plane

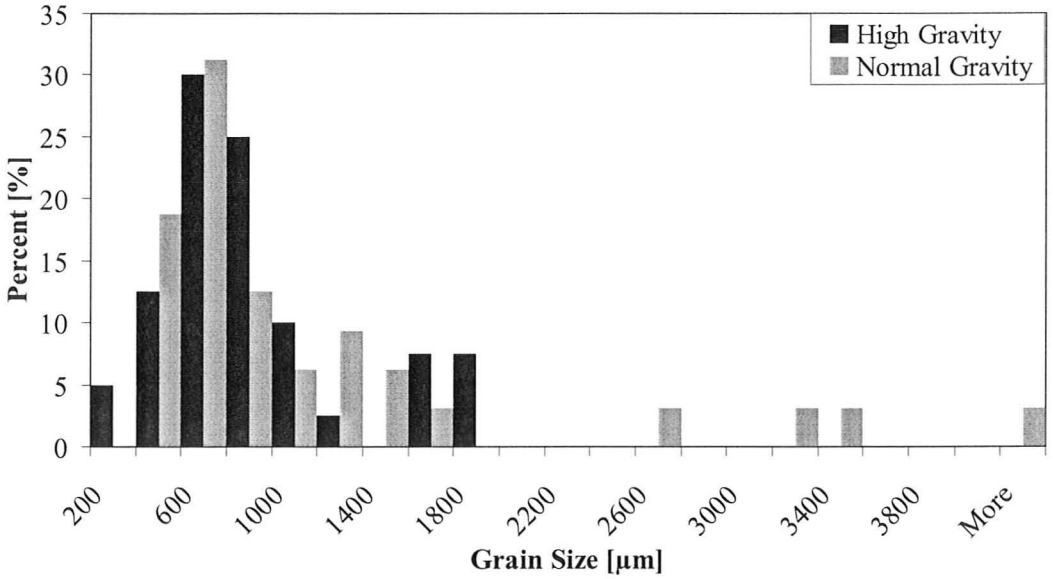


Figure 6.14: Grain size histogram of water-quenched $Sn_{99.7}Cu_{0.3}$ in the Zθ plane

The histograms show that the high-gravity sample has a more narrow distribution curve compared to the normal gravity sample. The normal gravity sample in the Zθ plane has larger grains of length greater than 2 mm than the normal gravity sample. In contrast, the high-gravity sample has a higher percentage of small grains.

## 6.2 Hardness Tests

### 6.2.1 Microhardness of Air-Cooled Bi-Sn

With the Clemex microindenter, microhardness was measured against the radius of the sample. For this purpose, a load of 25 g and a dwell time of 10 s were used. Figure 6.15 shows the microhardness of the Bi-Sn hypereutectic sample against the radius in the Rθ plane.

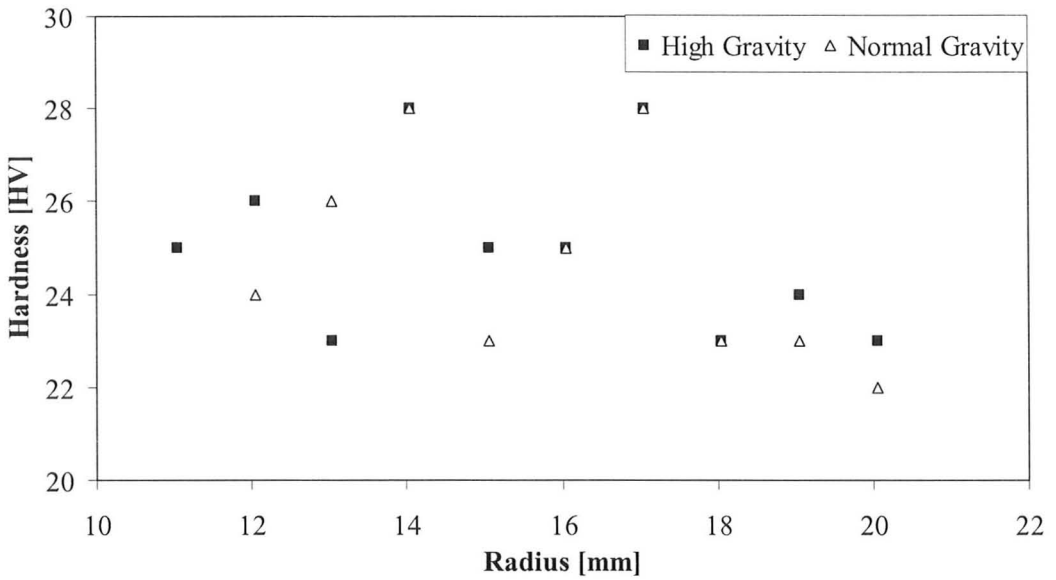


Figure 6.15: Plot of microhardness against radius for the air-cooled Bi-Sn hypereutectic in Rθ plane

From Figure 6.15, the average microhardness was 25.0 ± 1.9 HV for the high-gravity sample and 24.7 ± 2.2 HV for the normal gravity sample. There does not appear to be any correlation between the hardness of the sample with the radius. Figure 6.16 shows a plot of the microhardness against the radius of the Bi-Sn hypereutectic samples in the RZ plane.

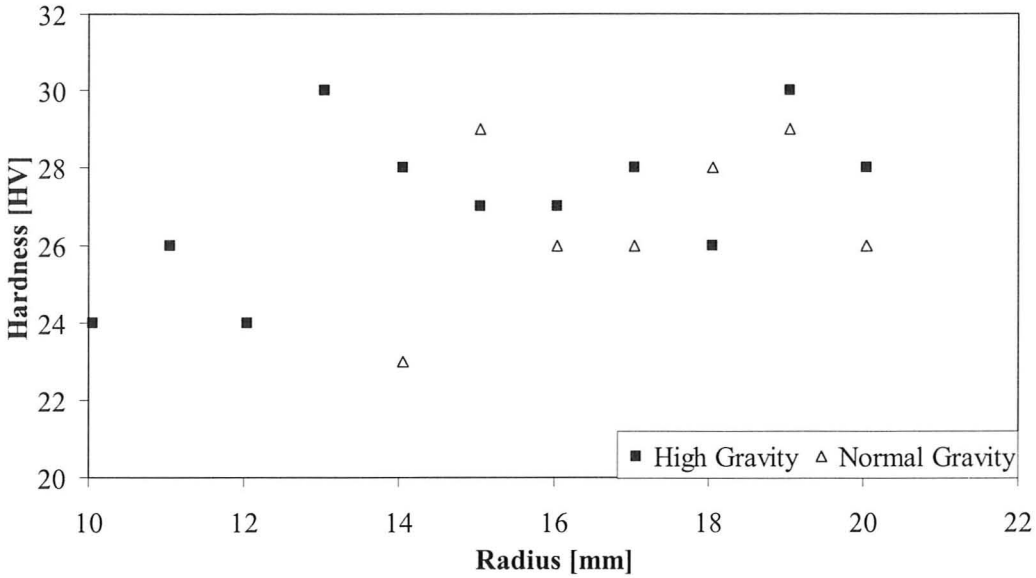


Figure 6.16: Plot of microhardness against radius for the air-cooled Bi-Sn hypereutectic in RZ plane

From Figure 6.16, the average microhardness was 27.7 ± 2.0 HV for the high-gravity sample and 26.7 ± 2.1 HV for the normal gravity sample. The plots do not show any correlation between hardness and radius.

6.2.2 Microhardness of Air-Cooled Sn

The microhardness of the air-cooled Sn samples was also measured with a load of 200 g and a dwell time of 10 s. Figure 6.17 shows the microhardness plotted against the radius of the Sn sample in the Rθ plane.

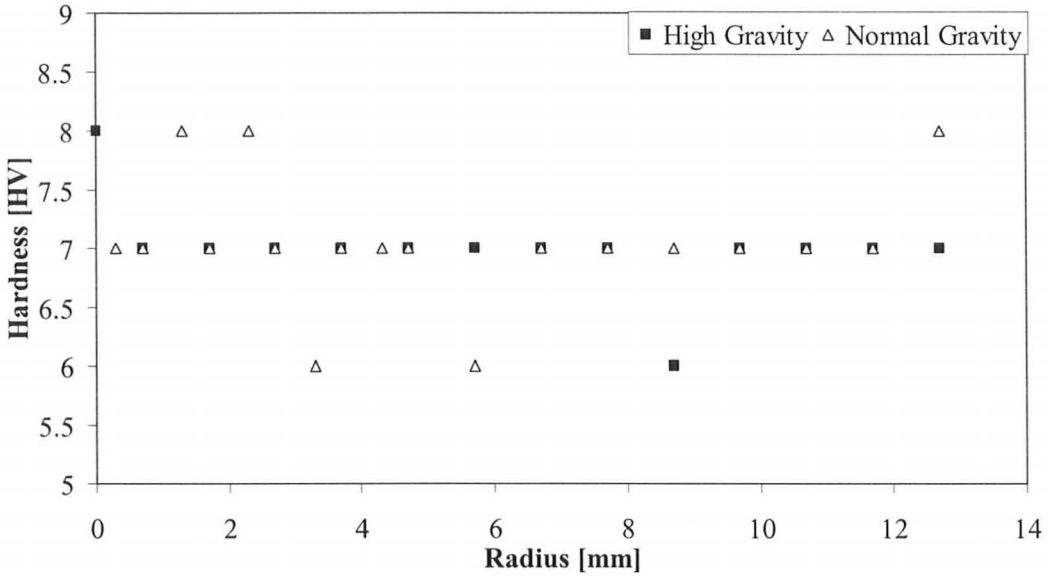


Figure 6.17: Plot of microhardness against radius for air-cooled Sn in Rθ plane

From Figure 6.17, the average hardness was 7.0 ± 0.4 HV for the high-gravity sample and 7.1 ± 0.5 HV for the normal gravity sample. There does not appear to be any correlation between the hardness of the sample with the radius. Figure 6.18 shows the microhardness plotted against the radius of the Sn specimen in the RZ plane.

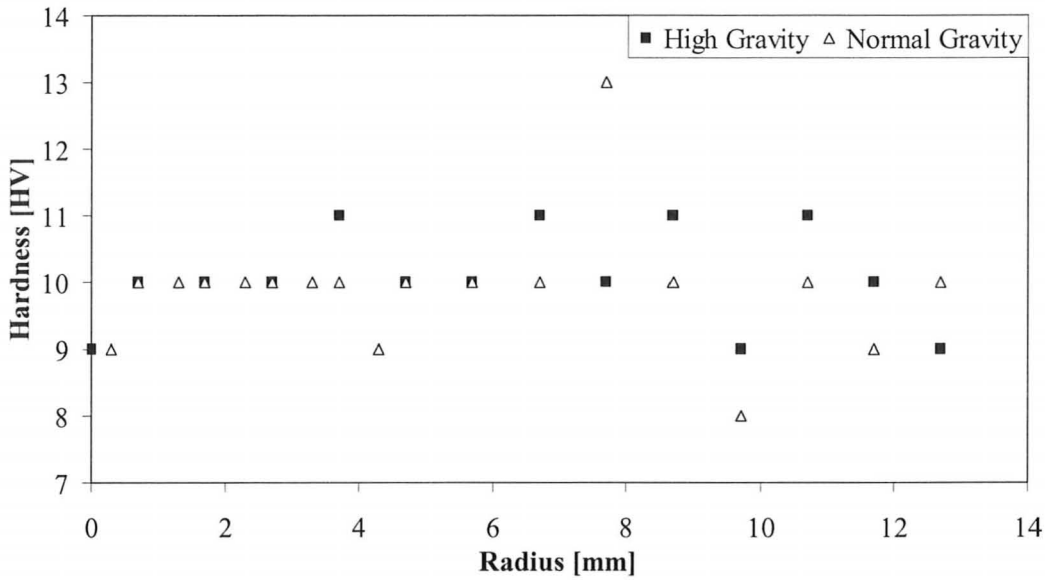


Figure 6.18: Plot of microhardness against radius for air-cooled Sn in RZ Plane

From Figure 6.18, the average hardness was 10.1 ± 0.7 HV for the high-gravity sample and 9.9 ± 1.0 HV for the normal gravity sample. There is no indication of any trend between the microhardness and the radius of the sample.

### 6.2.3 Microhardness of $Sn_{99.7}Cu_{0.3}$

Microhardness was also measured for the $Sn_{99.7}Cu_{0.3}$ samples with a load of 50 g and a 10 s dwell time. Figure 6.19 shows the plot of hardness against the radius for the $Sn_{99.7}Cu_{0.3}$ sample in the Rθ plane.

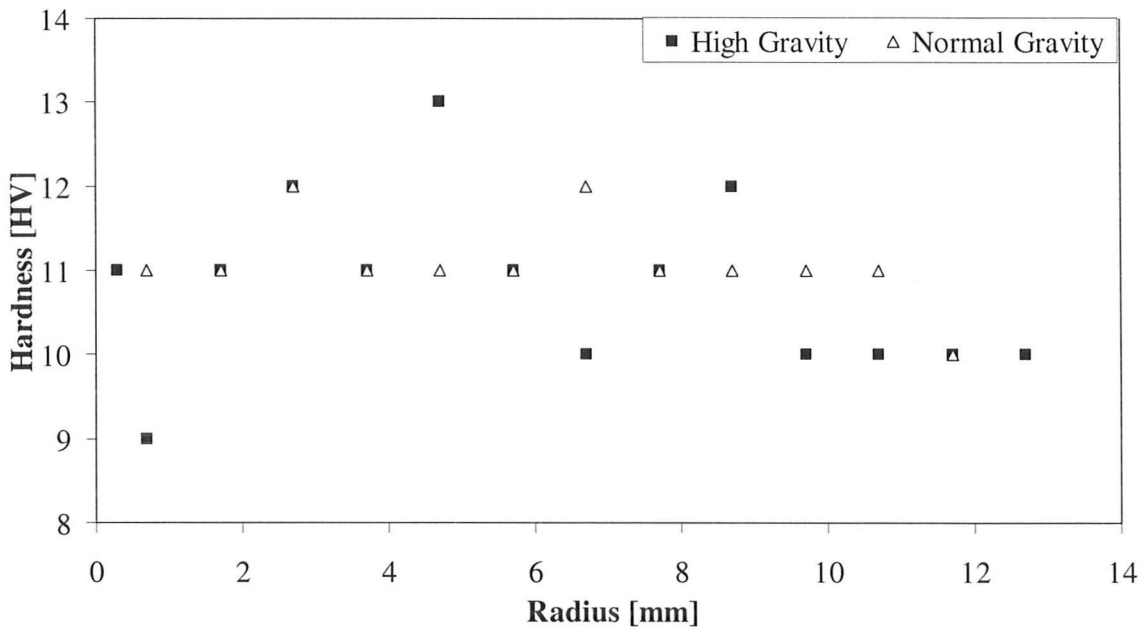


Figure 6.19: Plot of microhardness against radius for water-cooled $Sn_{99.7}Cu_{0.3}$ in Rθ plane

From Figure 6.19, the average microhardness was 10.8 ± 1.1 HV for the high-gravity sample and 11.1 ± 0.6 HV for the normal gravity sample. There does not appear to be any correlation between the hardness and the radius of the sample. Figure 6.20 shows the plot of the microhardness against the radius of the $Sn_{99.7}Cu_{0.3}$ sample in the RZ plane. The hardness was measured with a load of 25 g and a dwell time of 10 s.

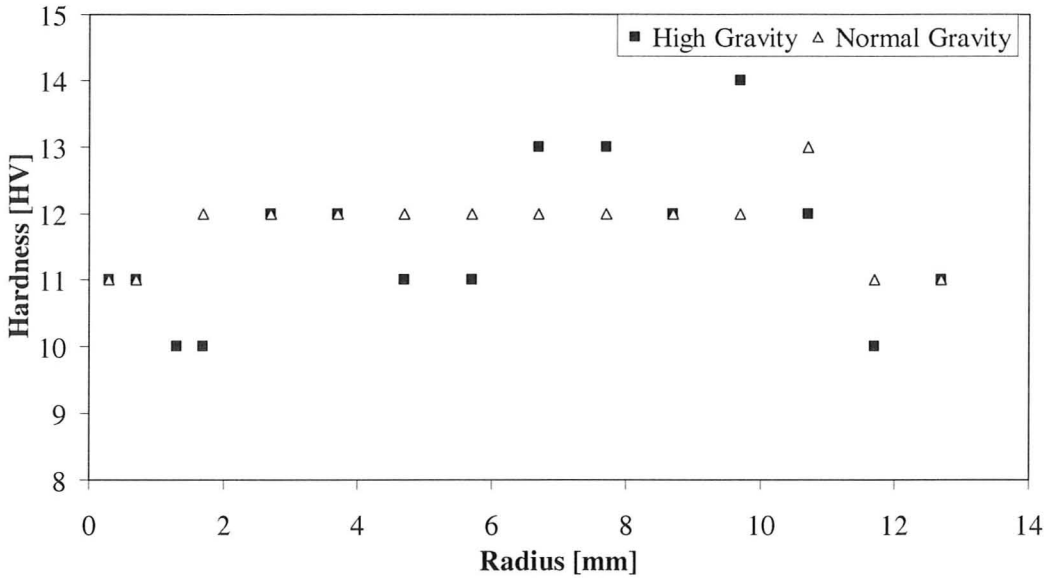


Figure 6.20: Plot of microhardness against radius for water-cooled $Sn_{99.7}Cu_{0.3}$ in the RZ plane

From Figure 6.20, the average microhardness was 11.5 ± 1.2 HV for the high-gravity sample and 11.9 ± 0.6 HV for the normal gravity sample. For the Sn and $Sn_{99.7}Cu_{0.3}$ samples, it was determined that the length of the indentations were actually smaller than the size of the grain. Therefore, the Vickers macrohardness test was conducted for the air-cooled Bi-Sn hypereutectic samples and the air-cooled Sn samples.

### 6.2.4 Macrohardness of Bi-Sn

With the Zwick 3212 indenter, the hardness of the air-cooled Bi-Sn samples was measured with a load of 5 kg and a dwell time of 10 s. Figure 6.21 shows the plot of hardness against radius for the air-cooled Bi-Sn hypereutectic sample in high-gravity in the Rθ plane, and the Bi-Sn sample in normal gravity in the hypereutectic and eutectic areas in the Rθ plane.

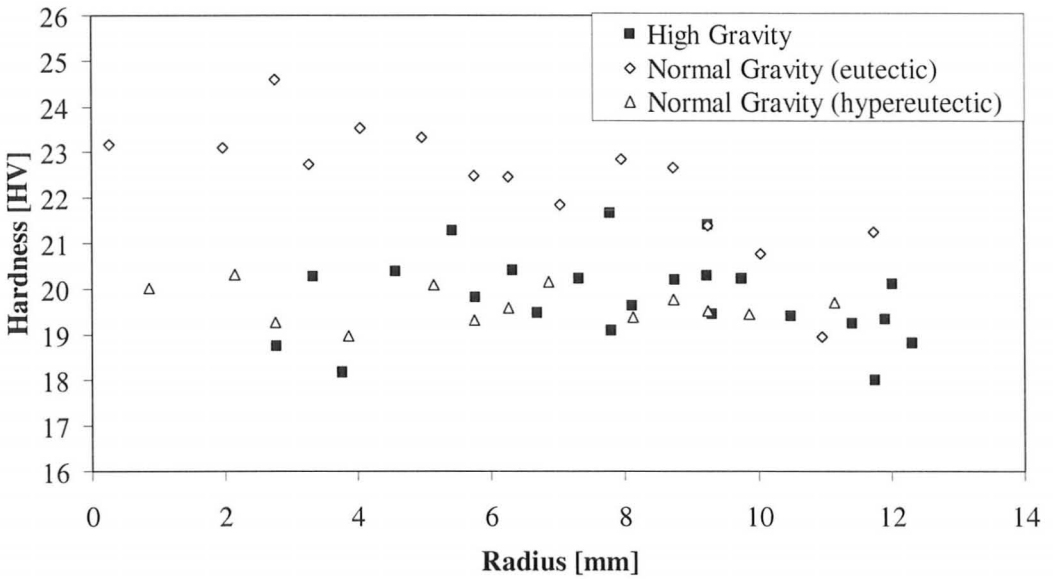


Figure 6.21: Plot of macrohardness against radius for air-cooled Bi-Sn in Rθ plane

From Figure 6.21, the average macrohardness was 19.8 ± 0.9 HV for the high-gravity sample, 22.3 ± 1.4 HV for the normal gravity sample in the eutectic area, and 19.7 ± 0.4 HV for the hypereutectic area. The hardness was about the same for the normal and high-gravity hypereutectic sample, but the normal gravity sample in the eutectic area had a higher hardness relative to both hypereutectic samples.

### 6.2.5 Macrohardness of Air-Cooled Sn

Macrohardness of the Sn samples was also measured by using a 5 kg load and a dwell time of 10 s. Figure 6.22 shows a plot of the macrohardness against the radius of the air-cooled Sn samples in the Rθ plane.

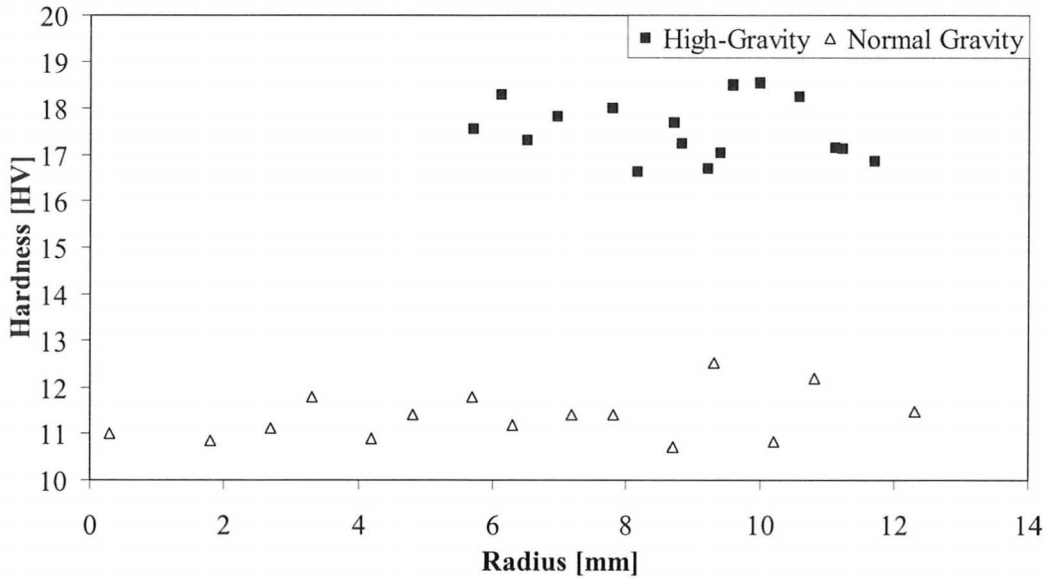


Figure 6.22: Plot of macrohardness against radius for air-cooled Sn in Rθ plane

From the plot in Figure 6.22, the average macrohardness is calculated as 17.7 ± 0.8 HV for the high-gravity sample and 11.4 ± 0.5 HV for the normal gravity sample. The high-gravity sample showed a higher range of macrohardness when compared to the normal gravity sample.

## 6.3 Calculation of the Rayleigh Number

The Rayleigh numbers were calculated using the dimensions of the sample container, the physical properties of the materials, and the unstable thermal gradient determined during solidification. Table 6.1 lists the physical and thermal properties of liquid Bi-Sn eutectic and liquid Sn.

Table 6.1: Fluid properties of liquid Bi-Sn eutectic (Hua et al. 1998) and liquid Sn (Faulkner 1954)

| | **Bi-Sn** | **Sn** |
|---|---|---|
| **liquid density,** $\rho_{liquid}$ | $8.49\times10^{3}$ kg/m$^3$ | $6.99\times10^{3}$ kg/m$^3$ |
| **coefficient of thermal expansion,** $\alpha$ | $15\times10^{-6}$ /K | $106\times10^{-6}$ /K |
| **specific heat capacity of liquid,** $c_p$ | 188 J/(kg·K) | 257 J/(kg·K) |
| **thermal conductivity,** $K_L$ | 22 W/(m·K) | 32.6 W/(m·K) |
| **dynamic viscosity,** $\mu$ | 0.022 kg/(m·s) | 0.00271 kg/(m·s) |

From the solidification conditions determined from Figure 5.2, there was a maximum unstable thermal gradient of 30 K/m when the Bi-Sn was solidifying by cooling in air. Using the physical properties of the melt and a fluid depth of 19.1 mm, the height of the capsule cavity, the Rayleigh number in normal gravity is calculated as:

$$Ra = \frac{(15\times10^{-6}\ /\mathrm{K})(-30\ \mathrm{K/m})(-9.81\ \mathrm{m/s^2})(19.1\times10^{-3}\ \mathrm{m})^4}{\left(\frac{22\ \mathrm{W/(m\cdot K)}}{(8.49\times10^{3}\ \mathrm{kg/m^3})(188\ \mathrm{J/(kg\cdot K)})}\right)\left(\frac{0.022\ \mathrm{kg/m\cdot s}}{8.49\times10^{3}\ \mathrm{kg/m^3}}\right)} = 16.4$$

The same unstable thermal gradient was used for calculating the Rayleigh number in high-gravity, but gravity was increased by a factor of 287. The fluid depth was also changed to 12.7 mm to reflect the change in the direction of acceleration from downward acceleration to radial acceleration. Thus, the high-gravity Rayleigh number is calculated as:

$$Ra = \frac{(15\times10^{-6}\ /\mathrm{K})(-30\ \mathrm{K/m})(287)(-9.81\ \mathrm{m/s^2})(12.7\times10^{-3}\ \mathrm{m})^4}{\left(\frac{22\ \mathrm{W/(m\cdot K)}}{(8.49\times10^{3}\ \mathrm{kg/m^3})(188\ \mathrm{J/(kg\cdot K)})}\right)\left(\frac{0.022\ \mathrm{kg/m\cdot s}}{8.49\times10^{3}\ \mathrm{kg/m^3}}\right)} = 923$$

From the solidification conditions determined from Figure 5.18, when the Bi-Sn eutectic was solidifying by quenching in ice-water slurry, there was a maximum unstable thermal gradient of 50 K/m. Thus, the Rayleigh number in normal gravity is calculated as:

$$Ra = \frac{(15\times10^{-6}\ /\mathrm{K})(-50\ \mathrm{K/m})(-9.81\ \mathrm{m/s^2})(19.1\times10^{-3}\ \mathrm{m})^4}{\left(\frac{22\ \mathrm{W/(m\cdot K)}}{(8.49\times10^{3}\ \mathrm{kg/m^3})(188\ \mathrm{J/(kg\cdot K)})}\right)\left(\frac{0.022\ \mathrm{kg/(m\cdot s)}}{8.49\times10^{3}\ \mathrm{kg/m^3}}\right)} = 27.4$$

By changing the same gravity and depth parameters as before, the Rayleigh number in high-gravity is calculated as:

$$Ra = \frac{(15\times10^{-6}\ /\mathrm{K})(-50\ \mathrm{K/m})(287)(-9.81\ \mathrm{m/s^2})(12.7\times10^{-3}\ \mathrm{m})^4}{\left(\frac{22\ \mathrm{W/(m\cdot K)}}{(8.49\times10^{3}\ \mathrm{kg/m^3})(188\ \mathrm{J/(kg\cdot K)})}\right)\left(\frac{0.022\ \mathrm{kg/(m\cdot s)}}{8.49\times10^{3}\ \mathrm{kg/m^3}}\right)} = 1{,}538$$

From the solidification conditions determined from Figure 5.34, when the Sn melt was solidified by cooling in air, there was a maximum unstable thermal gradient of 200 K/m. Thus, the Rayleigh number in normal gravity is calculated as:

$$Ra = \frac{(106\times10^{-6}\ /\mathrm{K})(-200\ \mathrm{K/m})(-9.81\ \mathrm{m/s^2})(19.1\times10^{-3}\ \mathrm{m})^4}{\left(\frac{32.6\ \mathrm{J/(m\cdot K\cdot s)}}{(6.99\times10^{3}\ \mathrm{kg/m^3})(257\ \mathrm{J/(kg\cdot K)}}\right)\left(\frac{0.00271\ \mathrm{kg/(m\cdot s)}}{6.99\times10^{3}\ \mathrm{kg/m^3}}\right)} = 3{,}934$$

The Rayleigh number in high-gravity is calculated as:

$$Ra = \frac{(106\times10^{-6}\ /\mathrm{K})(-200\ \mathrm{K/m})(287)(-9.81\ \mathrm{m/s^2})(12.7\times10^{-3}\ \mathrm{m})^4}{\left(\frac{32.6\ \mathrm{J/(m\cdot K\cdot s)}}{(6.99\times10^{3}\ \mathrm{kg/m^3})(257\ \mathrm{J/(kg\cdot K)}}\right)\left(\frac{0.00271\ \mathrm{kg/(m\cdot s)}}{6.99\times10^{3}\ \mathrm{kg/m^3}}\right)} = 220{,}700$$

From the solidification conditions determined from Figure 5.41, when the Sn melt was solidifying by quenching in water, there was a maximum unstable thermal gradient of 50 K/m. Thus, the Rayleigh number in normal gravity is calculated as:

$$Ra = \frac{(106\times10^{-6}\ /\mathrm{K})(-50\ \mathrm{K/m})(-9.81\ \mathrm{m/s^2})(19.1\times10^{-3}\ \mathrm{m})^4}{\left(\frac{32.6\ \mathrm{J/(m\cdot K\cdot s)}}{(6.99\times10^{3}\ \mathrm{kg/m^3})(257\ \mathrm{J/(kg\cdot K)}}\right)\left(\frac{0.00271\ \mathrm{kg/(m\cdot s)}}{6.99\times10^{3}\ \mathrm{kg/m^3}}\right)} = 1{,}113$$

In high-gravity, the Rayleigh number is calculated as:

$$Ra = \frac{(106\times10^{-6}\ /\mathrm{K})(-50\ \mathrm{K/m})(287)(-9.81\ \mathrm{m/s^2})(12.7\times10^{-3}\ \mathrm{m})^4}{\left(\frac{32.6\ \mathrm{J/(m\cdot K\cdot s)}}{(6.99\times10^{3}\ \mathrm{kg/m^3})(257\ \mathrm{J/(kg\cdot K)}}\right)\left(\frac{0.00271\ \mathrm{kg/(m\cdot s)}}{6.99\times10^{3}\ \mathrm{kg/m^3}}\right)} = 55{,}175$$

6.4 Transport of Primary Dendrites

To determine the effect of high-gravity on the velocity of the primary phase in the eutectic melt, a spherical Sn particle in a Bi-Sn eutectic melt was given a fixed radius of 5 μm. Using Stokes formula (Equation 2.15), the velocity of the particle in normal gravity is calculated as:

$$v = \frac{2(5\times10^{-6}\ \mathrm{m})^2(9.81\ \mathrm{m/s^2})(7.27\times10^{3}\ \mathrm{kg/m^3} - 8.49\times10^{3}\ \mathrm{kg/m^3})}{9(0.022\ \mathrm{kg/(m\cdot s)})}$$
$$= -3.02\times10^{-6}\ \mathrm{m/s}$$

Because the velocity is negative, the particle would move counter to the direction of gravity in the eutectic melt. Assuming that nucleation of the particle occurred at the bottom of the sample, the maximum distance that the particle could travel in normal gravity is the height of the sample, 19.1 mm. Thus, the time to travel the height of the sample is expressed as:

$$t = \frac{d}{v} \tag{6.1}$$

$$t = \frac{19.1\times10^{-3}\ \mathrm{m}}{3.02\times10^{-6}\ \mathrm{m/s}} = 6{,}367\ \mathrm{s}$$

With centrifugal acceleration, the gravitational acceleration becomes dependent on the radial position of the particle in the sample. So as the particle moves to the center of the sample, its velocity would steadily decrease. Using the formula for centrifugal acceleration (Equation 4.3), the Stokes formula is rewritten to reflect the radial dependence of the particle velocity and is expressed as:

$$v = \frac{2r_{particle}^2\omega^2 r_{sample}\left(\rho_{fluid} - \rho_{particle}\right)}{9\mu} \tag{6.2}$$

where the angular velocity of the spinning melt, $\omega$, is 471 radians/s and $r_{sample}$ is the radial position of the particle in the sample [m]. At the outer radius of the sample (12.7 mm), the velocity of the particle is calculated as:

$$v = \frac{2(5\times10^{-6}\ \mathrm{m})^2\left[2\pi(75\ \mathrm{rps})\right]^2(12.7\times10^{-3}\ \mathrm{m})(7.27\times10^{3}\ \mathrm{kg/m^3} - 8.49\times10^{3}\ \mathrm{kg/m^3})}{9(0.022\ \mathrm{kg/(m\cdot s)})}$$
$$= -8.68\times10^{-4}\ \mu\mathrm{m/s}$$

At the center of the sample, the velocity of the particle becomes zero. Knowing the initial and final velocities of the particle and the distance traveled, the deceleration is calculated with the following equation:

$$v_f^2 = v_i^2 + 2ad \tag{6.3}$$

$$a = \frac{0 - (8.68\times10^{-4}\ \text{m/s})^2}{2(12.7\times10^{-3}\ \text{m})} = -2.97\times10^{-5}\ \text{m/s}^2$$

Assuming that the particle nucleated at the outer radius of the sample, the time it takes for it to move to the center is determined with the following equation:

$$v_f = v_i + at \tag{6.4}$$

$$t = \frac{0 - 8.68\times10^{-4}\ \text{m/s}}{-2.97\times10^{-5}\ \text{m/s}^2} = 29.5\ \text{s}$$

Therefore, the solid particle in a melt in high-gravity would move faster than in a melt in normal gravity. Consequently, it would take less time in high-gravity for the particle to travel the radial length of the sample than in normal gravity to travel the height of the sample.

## 6.5 Solid-Liquid Interface Stability

In the Sn-Cu binary system, the liquidus slope, $m_L$, is −7.14 K/wt%, and the equilibrium partition ratio, $k$, is $8.57\times10^{-4}$ (Greenfield and Bowden 1949). The $Sn_{99.7}Cu_{0.3}$ sample has a solute concentration, $C_0$, of 0.3 wt%, a diffusion coefficient, $D_L$, of $4.5\times10^{-9}$ m$^2$/s (Flemings 1974), a solid thermal conductivity, $K_S$, of 56.5 W/(m·K) (Faulkner 1954), a liquid thermal conductivity, $K_L$, of 32.6 W/(m·K) (Faulkner 1954), and a latent heat of solidification, $L$, of 59,413 J/kg (Faulkner 1954). Because the Sn-Cu melt was also solidified by quenching in water, the Rayleigh numbers calculated for the water-quenched Sn were used. From Figure 5.41, the solid-liquid interface velocity, $R$, was 10.16 mm/s, and the liquid thermal gradient, $G_L$, was 0.05 K/mm. It could then be determined if the solidification conditions met the Mullins-Sekerka criteria for planar stability (Flemings 1954) with no convection, which is expressed as:

$$\frac{G_L}{R} + \frac{\rho_L L}{2K_L} \geq -\frac{m_L C_0 (1-k)}{kD_L}\frac{K_S + K_L}{2K_L}\zeta \tag{6.5}$$

It was assumed that the value of the stability function, $\zeta$, is equal to unity. The term for solidification conditions, on the left, is calculated as:

$$\frac{G_L}{R} + \frac{\rho L}{2K_L}$$

$$= \frac{0.05\ \text{K/mm}}{10.16\ \text{mm/s}} + \frac{(6.99\times10^3\ \text{kg/m}^3)(59.4\times10^3\ \text{J/kg})}{2\times32.6\ \text{W/(m}\cdot\text{K)}}$$

$$= 6{,}373{,}111\ \text{K}\cdot\text{s/m}^2$$

The critical value without convection, on the right, is calculated as:

$$-\frac{m_L C_0(1-k)}{kD_L}\frac{K_S+K_L}{2K_L}$$

$$=\frac{(-7.14\text{ K/wt\%})(0.3\text{ wt\%})(1-8.57\times10^{-4})}{(8.57\times10^{-4})(4.5\times10^{-9}\text{ m}^2/\text{s})}\frac{56.5\text{ W/(m}\cdot\text{K)}+32.6\text{ W/(m}\cdot\text{K)}}{2\times32.6\text{ W/(m}\cdot\text{K)}}$$

$$=7.60\times10^{11}\text{ K}\cdot\text{s/m}^2$$

When the Sn was solidified by quenching in water, the Rayleigh number in high-gravity was calculated as 55,175. Therefore, centrifugal acceleration likely caused laminar convection during solidification. The Mullins-Sekerka criteria for stable solidification assumes no convection (Flemings 1974), but if perfect convection was taken into consideration, the critical value could be rewritten similar to the Rutter-Chalmers criteria for interface stability with perfect convection:

$$-\frac{m_L C_0(1-k)}{D_L}\frac{K_S+K_L}{2K_L}$$

$$=-\frac{(-7.14\text{ K/wt\%})(0.3\text{ wt\%})(1-8.57\times10^{-4})}{4.5\times10^{-9}\text{ m}^2/\text{s}}\times\frac{56.5\text{ W/(m}\cdot\text{K)}+32.6\text{ W/(m}\cdot\text{K)}}{2\times32.6\text{ W/(m}\cdot\text{K)}}$$

$$=4.76\times10^{8}\text{ K}\cdot\text{s/m}^2$$

## 6.6 Hydrostatic Pressure and Transformation Temperatures

The simplified Clausius-Clapeyron equation was used to determine the change in transformation temperature for freezing and other phase transformations with increasing hydrostatic pressure caused by high-gravity. The phase transformations examined were β-Sn to α-Sn, liquid to solid Sn, and liquid to solid Bi-Sn eutectic. It was assumed that increasing centrifugal acceleration only affected the hydrostatic pressure in terms of the samples' weight, and not the external atmospheric pressure since a significant effort was made to fill the capsule cavity as much as possible. Furthermore, any trapped gas would have moved towards the center of the cavity where centrifugal acceleration would be near zero.

For the transformation from α-Sn to β-Sn, the density of α-Sn, $\rho_\alpha$, was 5,750 kg/m$^3$, and the density of β-Sn, $\rho_\beta$, is 7,280 kg/m$^3$ (Faulkner 1954). Thus, the change in volume per unit mass of α-Sn to β-Sn is calculated as:

$$\Delta V=\left(\frac{1}{7280\text{ kg/m}^3}-\frac{1}{5750\text{ kg/m}^3}\right)=-3.655\times10^{-5}\text{ m}^3/\text{kg}$$

Because it was assumed that atmospheric pressure was not affected by centrifugal acceleration, the change in hydrostatic pressure is expressed as:

$$\Delta p=\rho 287gh+p_0-(\rho gh+p_0)=286\rho gh \qquad (6.6)$$

Thus, with a height of 12.7 mm, the change in hydrostatic pressure is calculated as:

$$\Delta p=(7365\text{ kg/m}^3)(286)(9.81\text{ m/s}^2)(0.0127\text{ m})=2.62\times10^5\text{ Pa}$$

The change in enthalpy for the phase transformation, $L$, is 248.1 J/kg and the transformation temperature, $T_{trans}$, is 286 K (Swalin 1954). Substituting the changes in pressure and volume into the simplified Clausius-Clapeyron equation so that the change in transformation temperature is calculated as:

$$\Delta T = \frac{T_{trans}\Delta V \Delta P}{L} \tag{2.20}$$

$$\Delta T = \frac{(286\text{ K})(-3.655\times10^{-5}\text{ m}^3/\text{kg})(2.62\times10^{5}\text{ Pa})}{248.1\text{ J/kg}} = -11.0\text{ K}$$

With the solid and liquid densities are listed in Table 4.1, the change in volume for the liquid to solid transformation of Sn is calculated as:

$$\Delta V = \frac{1}{6990\text{ kg/m}^3} - \frac{1}{7280\text{ kg/m}^3} = 7.28\times10^{-7}\text{ m}^3/\text{kg}$$

The change in hydrostatic pressure is calculated as:

$$\Delta p = (6990\text{ kg/m}^3)(286)(9.81\text{ m/s}^2)(0.0127\text{ m}) = 2.49\times10^{5}\text{ Pa}$$

Thus, the change in freezing temperature is then calculated as:

$$\Delta T = \frac{(505\text{ K})(7.28\times10^{-7}\text{ m}^3/\text{kg})(2.49\times10^{5}\text{ Pa})}{59{,}200\text{ J/kg}} = 0.002\text{ K}$$

With the solid and liquid densities of Bi-Sn eutectic listed in Table 4.1, the change in volume for the liquid to solid transformation of Bi-Sn eutectic is calculated as:

$$\Delta V = \frac{1}{8489\text{ kg/m}^3} - \frac{1}{8553\text{ kg/m}^3} = 8.815\times10^{-7}\text{ m}^3/\text{kg}$$

The change in hydrostatic pressure is calculated as:

$$\Delta p = (8489\text{ kg/m}^3)(286)(9.81\text{ m/s}^2)(0.0127\text{ m}) = 3.02\times10^{5}\text{ Pa}$$

Thus, the change in freezing temperature is then calculated as:

$$\Delta T = \frac{(411\text{ K})(8.814\times10^{-7}\text{ m}^3/\text{kg})(3.02\times10^{5}\text{ Pa})}{46{,}520\text{ J/kg}} = 0.002\text{ K}$$

# CHAPTER 7: DISCUSSION

## 7.1 Microstructure of the Bi-Sn Samples

Although the Bi and Sn metals were mixed in the correct proportions to produce the eutectic, the microstructure showed areas of primary Sn indicating that the sample was not at the correct composition. This was most likely due to the Sn content of the Sn-coated steel containers which would have increased the Sn concentration in the sample during melting. However, the increase in concentration was minimal and areas of the eutectic phase could still be examined. Furthermore, later use of the Al capsule resolved this issue. The Bi-Sn eutectic microstructure consisted of a lamellar interphase of rhombohedral Bi and tetragonal Sn. When the melt was cooled in air, the eutectic lamellar appeared to be irregular in normal gravity and more complex, but with some regularity in high-gravity. The average eutectic spacing of the lamellar microstructure increased from 4.82 ± 2.37 μm in normal gravity to 5.60 ± 2.70 μm, in high-gravity. The regularity of the lamellar structure is attributed to Rayleigh-Bénard convection induced by centrifugal acceleration. The calculated Rayleigh number, when air-cooled, was 16.4 in normal gravity and 923 in high-gravity. In normal gravity, the critical Rayleigh number for convection is 1708 because the melt was completely contained by the capsule, thereby creating rigid-rigid boundary conditions. In high-gravity, the critical Rayleigh number for convection is lowered to 658 because the melt leakage and the transport of air bubbles to the center of the melt created a free surface, thereby creating rigid-non-rigid boundary conditions. Thus, there was likely no convection in the melt during normal gravity solidification, but the centrifugal acceleration enhanced the buoyancy effect in the high-gravity sample thereby increasing the Rayleigh number and inducing convection in the melt.

When the Bi-Sn eutectic melt was solidified by quenching in ice-water slurry, the microstructures of both the high- and normal gravity samples appeared to have complex regular lamellar eutectic. Furthermore, the average eutectic spacing decreased which was expected due to the increased growth rate. The average eutectic spacing of the Bi-Sn microstructure was 1.66 ± 0.69 μm for normal gravity sample and 1.94 ± 0.93 μm for the high-gravity sample. Statistically speaking, the average eutectic spacing between the high- and normal gravity samples are so close that they are virtually equal within error. The Rayleigh numbers were calculated to be 27.4 in normal gravity and 1,538 in high-gravity so that there was likely no Rayleigh-Bénard convection in normal gravity, but it was supposedly present in high-gravity. This indicates that even though the conditions were sufficient for the onset of convection in high-gravity, convection did not have an effect on the eutectic microstructure due to the increased solidification rate.

Even if the critical Rayleigh number was not exceeded, it cannot be concluded that convection and fluid motion were absent. Other factors could

have caused fluid motion such as solidification shrinkage, transverse solute distribution, and Marangoni convection. Another mode of convective heat transport is caused by a crystal moving in a melt at rest, or relative to the melt, due to the difference between their densities. This mechanism is similar to forced convection and was evident in the Bi-Sn hypo- and hypereutectic samples in high-gravity. For the hypereutectic Bi-Sn melt (50 wt% Sn), primary Sn solidified before the eutectic and primary Bi solidified for the hypoeutectic Bi-Sn alloy (25 wt% Sn). The velocity of a 5 μm Sn particle in a Bi-Sn eutectic melt was 886 μm/s in high-gravity which was much faster than 3 μm/s calculated for the particle in normal gravity. When the Bi-Sn melt was solidified by cooling in air, the cooling rate from Figure 5.2 indicates that it took 249 s for the temperature to go from the nucleation temperature of the primary Sn phase (~160°C) to eutectic solidification temperature (138°C). Thus, the Sn crystals would not be able to travel very far in the melt in normal gravity, but in high-gravity they would be able to travel farther in the melt. As a result, this caused the separation of primary Sn to the center of the solidified sample. For the hypoeutectic sample, the Bi crystals moved to the outer radius of the sample due to the high-gravity.

When the hypereutectic Bi-Sn melt was quenched in ice-water slurry, the cooling rate was faster, giving the Sn crystals less time to travel in the melt. Based on the cooling rate determined from Figure 5.18, it took 51 s for the melt temperature to go from the primary phase nucleation temperature to the eutectic solidification temperature. Thus, the Sn crystals would not travel very far in normal gravity, but would travel farther in high-gravity. However, the micrographs show that the primary Sn phase was not completely isolated to the center of the sample like that seen for the air-cooled sample. Quenching would create a higher undercooling before nucleation so that there would be less time for the Sn crystals to move in the melt and increasing the nucleation rate. Therefore, several grains would travel in the melt, growing very fast and stack on top of one another so that the distribution of Sn dendrites would be more uniform in the quenched samples than in the air-cooled samples.

## 7.2 Microstructure of the Sn Samples

When the Sn melt was solidified by cooling in air, both high- and normal gravity samples appeared to have equiaxed microstructures. The Rayleigh numbers were calculated as 3,934 in normal gravity and 220,700 in high-gravity indicating Rayleigh-Bénard convection likely occurred during solidification in both high- and normal gravity, but the convective flow would be greater in high-gravity. From the grain size histograms of the specimens, shown in Figure 6.5 to Figure 6.7, the mean grain size between the high- and normal gravity samples was approximately the same (between 0.4 mm to 0.6 mm). However, the distributions of the high-gravity specimens were narrower or had a higher percentage of grains smaller than the mean size than the normal gravity specimens. Furthermore, the graphs for grain density (number of grains per unit area) shown in Figure 6.8 and Figure 6.9 indicate that in the Rθ plane, the grain density is higher in high-gravity

than in normal gravity. Conversely for the RZ plane, there is a higher grain density in normal gravity than in high-gravity. The normal gravity sample should have had a columnar microstructure, but it is believed that hot-mounting the specimens exposed them to high heat and pressure, causing them to recrystallize. The recrystallization described in Section 5.5, would have nucleated equiaxed grains in both the high- and normal gravity specimens after the solidification process, thereby making the grain size histograms and grain density charts inaccurate.

When the Sn melt was solidified by quenching in water, the high-gravity sample had an equiaxed microstructure whereas the microstructure of the normal gravity sample was columnar. Because these specimens were cold-mounted, they did not recrystallize during the mounting process, as demonstrated in Section 5.5. The Rayleigh numbers were calculated as 1,113 in normal gravity and 55,175 in high-gravity, indicating that Rayleigh-Bénard convection likely only took place in the high-gravity sample. The enhanced fluid flow would have transported Sn nuclei to the outer radius of the container, thereby impinging columnar growth. It also would have increased shear stress on the growing columnar grains, thereby fragmenting the grains. The fluid flow would have subsequently transported the fragments to the center of the sample where they would continue to grow as equiaxed grains.

## 7.3 Microstructure of the $Sn_{99.7}Cu_{0.3}$ Samples

The presence of the copper pipe increased the Cu concentration in the Sn melt and affected the microstructure of the solidified sample. The microstructure of the $Sn_{99.7}Cu_{0.3}$ sample appeared to be cellular in high-gravity, as seen in Figure 5.50 to Figure 5.52, and dendritic in normal gravity, as seen in Figure 5.53 to Figure 5.55. In addition, microstructure of the high-gravity sample showed evidence of what is believed to be entrapped liquid within the cellular grains during solidification as seen in Figure 5.50 to Figure 5.52. Even though the specimens were hot-mounted, it is believed that the increased Cu concentration increased the recrystallization temperature. The transition from dendritic to cellular solidification is believed to be caused by the presence of convection during solidification in high-gravity. The Rayleigh numbers were calculated as 1,113 in normal gravity and 55,175 in high-gravity indicating that the Rayleigh-Bénard convection occurred in the melt during solidification in high-gravity. Based on the Mullins-Sekerka criteria for stable solidification (Flemings 1974), the solidification conditions give a calculated value of $6.37\times10^{6}$ K·s/m$^2$. Without convection during solidification, the critical value is calculated as $7.60\times10^{11}$ K·s/m$^2$, but when there is perfect convection, the critical value decreases to $4.76\times10^{8}$ K·s/m$^2$, three orders of magnitude lower than the value without convection. Thus, the solid-liquid interface was more stable in high-gravity than in normal gravity during solidification, but the interface was not stable enough to be planar. However, because the actual Rayleigh number was so much higher than the critical Rayleigh number, the centrifugal acceleration may have induced

turbulent convection as opposed to perfect convection. The turbulent convection could have created instabilities along the solid-liquid interface which would have caused the entrapped liquid. The interface would have grown around the entrapped liquid which would have subsequently nucleated and crystallized, but in a different crystal orientation. Because the critical value was higher in normal gravity, the solid-liquid interface was unstable and as the cellular dendrites were growing, secondary dendrite arms would branch off from along the dendrite length.

## 7.4 Effect of High-Gravity on Variation in Hardness

In order to characterize the samples' strength, the Vickers hardness was measured to determine the resistance to localized plastic deformation. Hardness is determined by how well dislocations are created and how much energy is required to move them in the crystal lattice. Changes in crystal orientations, such as in grain boundaries or eutectic lamella would impinge dislocation movement during plastic deformation. As a result, in order to transport the dislocations from one crystal orientation to another, more energy would be required, thereby making the sample stronger. Therefore, smaller grains or finer eutectic spacing would improve the hardness of a material, as is known from study of metals (i.e. the Hall-Petch effect) (Callister 2003).

Microhardness studies of the air-cooled Bi-Sn eutectic samples, as seen in Figure 6.15 and Figure 6.16, the air-cooled Sn samples, as seen in Figure 6.17 and Figure 6.18, and the water-quenched $Sn_{99.7}Cu_{0.3}$ samples, as seen in Figure 6.19 and Figure 6.20, showed a slight increase in the average microhardness in the high-gravity samples over the normal gravity samples, but the difference was so small that the two values were virtually equal within the standard deviation. Since the instrument for microhardness measurement uses a low load and hence makes small indentations, the indentations made in this experiment were typically smaller than the grains of the samples. A Bi-Sn eutectic grain consists of two different crystallographic phases and the interphase region would act as a barrier to dislocation movement, thereby making it stronger than pure Sn, but since the eutectic spacing in high-gravity was very close to that in normal gravity, the microhardness was not affected by gravity. Because the indentations were smaller than the Sn grains, it could be concluded that the centrifugal acceleration did not affect crystal structure of the Sn samples in terms of the atomic spacing.

Microhardness of the air-cooled solidified Sn, air-cooled solidified Bi-Sn hypereutectic in high-gravity, and air-cooled Bi-Sn in the hypereutectic and eutectic regions in normal gravity was studied by using a higher load. As a result, the indentations were larger and covered more area of the sample. Thus, the indentations were probably influenced by grain boundaries of the samples which made the samples seem harder. The study for the air-cooled Bi-Sn samples, as seen in Figure 6.21, indicates that the normal gravity hypereutectic sample was as hard as its high-gravity counterpart. However, the normal gravity sample in the eutectic area was harder than the hypereutectic areas of both the normal and high-

gravity samples. This is attributed to the large primary crystals in the hypereutectic which have less area to impinge dislocation movement, hence making them softer than the eutectic. For Sn solidified by cooling in air, the high-gravity sample was harder than the normal gravity sample. The high-gravity sample had a higher grain density than the normal gravity sample. Thus, there were more grain boundaries which would cause increase the dislocation impingement.

## 7.5 Effect of Hydrostatic Pressure

Another effect of high-gravity was the increase in hydrostatic pressure which changed the phase transformation temperature. The centrifugal acceleration would increase the hydrostatic pressure of the melt next to the container's wall which could have changed the solidification morphology and hence the microstructure of the sample formed under high-gravity. Using the simplified Clausius-Clapeyron equation, it was determined that in principle, the temperature of the α-Sn to β-Sn transformation decreased 11°C when put in a high-gravitational field where atmospheric pressure is not affected. However in practice, the sample did not reach that temperature so the change in transformation temperature was not observed. Furthermore, certain alloying elements added to the metal by the manufacturer, also inhibit this transformation. For the freezing of pure Sn and Bi-Sn eutectic, the calculated changes in freezing temperatures due to centrifugal acceleration for Sn and Bi-Sn were ~0.002 K, which were too small to be accurately measured to be confirmed. Moreover, according to Dudley and Hall (1960), a change in the solidification temperature of Sn from 232°C to 250°C would require an atmospheric pressure of 5000 atm. Attaining this change in hydrostatic pressure by increasing the weight of the Sn requires a gravitational acceleration equivalent to $545{,}000g_0$, which the present equipment is not capable of attaining. Therefore, even though centrifugal acceleration increased the hydrostatic pressure of the sample during solidification, there was no significant change in the solidification temperature.

# CHAPTER 8: CONCLUSIONS

A high-gravitational field was effectively simulated on a melt by spinning the melt in a container inducing centrifugal acceleration. The gravitational field simulated, for the condition used, was about 287 times the earth's gravity. Solidification of the melt under this condition had effects on microstructure development, many of which are attributed to enhanced fluid flow and increased convection during the solidification/crystallization process. Therefore, the study of this experiment has led to the following conclusions:

1. When solidifying the Bi-Sn melts by cooling in air, the centrifugal acceleration induced the Rayleigh-Bénard convection causing a transition in the eutectic lamellar microstructure from irregular to "complex regular." Furthermore, although the average eutectic spacing decreased when the Bi-Sn melt was solidified by quenching the chamber in ice-water slurry, the convection had less of an effect on the regularity of the eutectic microstructure relative to the microstructure developed from the air-cooled samples since both normal and high-gravity samples demonstrated complex regular structures when quenched.
2. For the Bi-Sn hypereutectic and hypoeutectic samples, the centrifugal acceleration caused the separation of the primary phase from the eutectic phase and the concentration of the primary phase to the center or outer radius of the sample, depending on the density of the primary phase relative to the eutectic melt. By using the Stokes formula, it was determined that the high-gravitational field increased the velocity of the primary phase by a factor of 287 causing separation.
3. When commercially-pure Sn was solidified by quenching in water in high-gravity, the microstructure consisted of more equiaxed grains that were smaller and more uniform than the microstructure of the normal gravity sample. This was caused by the enhanced convection in the melt which impinged columnar grain growth leaving equiaxed grains. The centrifugal acceleration caused the Sn sample to have a higher Vickers hardness which was likely due to the decreased average grain size.
4. Centrifugal acceleration also caused a transition in the solidification mechanisms of the $Sn_{99.7}Cu_{0.3}$ sample to grow from dendritic to cellular. In addition, the average grain size of the high-gravity sample was smaller than that of the normal gravity sample. Using the Mullins-Sekerka criteria for stable solidification, it was determined that centrifugal acceleration enhanced convection which in turn lowered the critical value for stable solidification so that solidification produced a cellular structure whereas in normal gravity, secondary branched-out dendrite arms formed.
5. The Rayleigh numbers show that inducing centrifugal acceleration either caused the onset of convection or its enhancement. The convection in high-gravity would increase the rate at which heat and solute are transported away from the solid-liquid interface. The enhanced convection would also cause

columnar grains to fragment, thus making smaller grains, or else transport nuclei to the solidification front, thereby impinging columnar grain growth.

6. The centrifugal acceleration did not have an effect on the eutectic spacing of the Bi-Sn eutectic nor did it have any effect on its micro- or macrohardness. The microhardness of the Sn samples were unaffected by centrifugal acceleration indicating that it did not have an effect on the atomic structure. Finally, the effect of high-gravity on hydrostatic pressure was too small to be measurable for the solidification temperature of Sn and the Bi-Sn alloy. Furthermore, although there was a notable for the β-Sn to α-Sn transformation in principle, impurities in the metal would inhibit this transformation in practice.

# APPENDIX: A

## A.1 Derivation of the Clausius-Clapeyron Equation (Swalin 1972)

The transformation of α-phase to β-phase occurs at a fixed temperature and pressure so that at the transition temperature, the change in free energy, $\Delta G$, for the phase change is zero so that:

$$G_\alpha = G_\beta \tag{A.1}$$

and:

$$dG_\beta = dG_\alpha \tag{A.2}$$

Because the transformation is reversible, the change in free energy can be written as:

$$dG = Vdp - SdT \tag{A.3}$$

Extending Equation (A.3) for the β-phase and α-phase gives:

$$dG_\alpha = V_\alpha dp - S_\alpha dT \tag{A.4}$$

and:

$$dG_\beta = V_\beta dp - S_\beta dT \tag{A.5}$$

Using Equation (A.1) and rearranging so that:

$$\frac{dp}{dT} = \frac{S_\beta - S_\alpha}{V_\beta - V_\alpha} \tag{A.6}$$

Equation (A.6) can also be expressed as:

$$\frac{dp}{dT} = \frac{\Delta S}{\Delta V} \tag{A.7}$$

Because the reaction occurs at constant temperature and pressure, the change in entropy is expressed as:

$$\Delta S = \int_\alpha^\beta \frac{DQ}{T} = \int_\alpha^\beta \frac{dH}{T} = \frac{L}{T} \tag{A.8}$$

where $L$ is the change in enthalpy of the reaction. Substituting Equation (A.8) into Equation (A.7) gives the Clausius-Clapeyron equation:

$$\frac{dp}{dT} = \frac{L}{T\Delta V} \tag{A.9}$$

The Clausius-Clapeyron equation shows that a change in transition temperature results in a subsequent pressure change. Assuming that the change in the transition temperature is small compared with $T_{trans}$, $\Delta V$, and $L$, and if $T_{trans}$ is considered constant, then Equation (A.9) can be simplified and expressed as:

$$\Delta T = \left( \frac{T_{trans} \Delta V}{L} \right) \Delta p \tag{A.10}$$

## BIBLIOGRAPHY


Allen, B.C. and Isserow, T., *Acta Met.*, **5**, 465 (1957).

Baker, H. (Editor), *ASM Handbook: Alloy Phase Diagrams, v.3*, ASM International, USA (1992).

Battaile, C.C., Grugel, R.N., Hmelo, A.B. and Wang, T.G., *Metallurgical and Materials Transactions A*, **25A**, 865 (1994).

Bénard, H., *Rev. Gén. Sci. Pur. Appl.*, **11**, 1261 (1900).

Bergé, P. and Dubois, M., *Contemporary Physics*, **25**, 535 (1984).

Block, M.J., *Nature*, **178,** 650 (1956).

Bodenschatz, E., Pesch, W. and Ahlers, G., *Annu. Rev. Fluid Mech. 2000*, **32**, 709 (2000).

Boussinesq, J., *Theorie Analytique de la Chalor, Vol. 2*, Gauthier-Villars, Paris (1903).

Callister, W.D. Jr., *Materials Science and Engineering: an Introduction, 6th ed.*, John Wiley & Sons, Inc., USA, (2003).

Carruthers, J.R., *J. Crystal Growth*, **42**, 379 (1977).

Carruthers, J.R. and Testardi, L.R., *Ann. Rev. Mater. Sci.*, **13**, 247 (1983).

Chalmers, B., *Principles of Solidification*, John Wiley & Sons, Inc., New York (1964).

Chandrasekhar, S., *Hydrodynamic and Hydromagnetic Stability*, Oxford University Press, Oxford (1961).

Chereminsinoff, N.P., *Handbook of Heat and Mass Transfer – Volume 1: Heat Transfer Operations*, Gulf Publishing Company, United States (1986).

Curreri, P.A. and Stefanescu, D.M., *Low-gravity effects during solidification*, in: *Metals Handbook, v.15*, ASM International, Metals Park, OH., (1988), pp.147-158.

Dudley, J.D. and Hall, H.T., *Physical Review*, **118**, 1211 (1960).

Faulkner, C.J., *The Properties of Tin*, Tin Research Institute, England (1954).

Feuerbacher, B., *Microgravity Materials Sciences: Introduction*, in: Feuerbacher, B., Zamacher, H. and Naumann, R.J., (Eds.), *Materials Sciences in Space: A Contribution to the Scientific Basis of Space Processing*, Springer-Verlag, Berlin (1986), pp.3-10.

Fishlock, D., *Chemistry World*, **1**, 46 (2004).

Flemings, M.C., *Solidification Processing*, McGraw-Hill Book Company, New York (1974).

Glicksman, M.E., Koss, M.B., Bushnell, L.T. and Lacombe, J.C., *Mat. Res. Soc. Symp. Proc.*, **367**, 13 (1995).

Glicksman, M.E. and Sokolowski, R.S., *Adv. Space Res.*, **3**, 129 (1983).

Greenfield, L.T. and Bowden, J.S., *Equilibrium Data for Tin Alloys*, Tin Research Institute, England, (1949).

Grugel, R.N., *Met. Trans. A.*, **20A**, 1284 (1989).

Grugel, R.N. and Anilkumar, A.V., *42nd AIAA Aerospace Sciences Meeting and Exhibit*, 6091 (2004).

Hamacher, H., Fitton, B. and Kingdon, K., *The Environment of Earth-Orbiting Systems*, in: Walter, H.U., (Ed.), *Fluid Sciences and Materials Science in Space*, Springer-Verlag, Berlin (1987), pp.1-46.

Hua, F., Mei, Z. and Glazer, J., *1998 Electronic Components and Technology Conference*, 277 (1998).

Hung, J.D. and Jackson, K.A., *Transactions of the Metallurgical Society of AIME*, **236**, 843 (1966).

Ivantsov, G.P., *Dokl. Akad. Nauk.*, **58**, 56 (1947).

Jeffreys, H., *Phil. Mag.*, **2** 833 (1926).

Jeffreys, H., *Proc. Roy. Soc. London A*, **118**, 195 (1928).

Johnston, M.H. and Griner, C.S., *Met. Trans. A.*, **8A**, 77 (1977).

Johnston, M.H. and Parr, R.A., *Met. Trans. B.*, **13B**, 85 (1982).

Koschmieder, E.L., *Bénard Cells and Taylor Vortices*, Cambridge University Press, Cambridge (1993).

Kumar, P., Srinivasan, K. and Dutta, P., *Mechanics Research Communications*, **33**, 593 (2006).

Lord Rayleigh, *Phil. Mag.*, **32** 529 (1916).

Mack, T. and Tensi, H.M., *Z. Metallkd.*, **91**, 397 (2000).

Manneville, P., *Rayleigh-Benard convection: Thirty years of experimental, theoretical, and modeling work*, in Mutabuzi, I. et al., (Eds.), Spatio-Temporal Cellular Structures: Henri Benard Centenary Review, Springer-Tracts in Modern Phys., New York (2006), pp.41-60.

Mashimo, T., *Acta Astronautica*, **48**, 145 (2001).

McCay, T.D. et al., *J. Thermodynamics*, **3**, 345 (1989).

Müller, G., *Adv. Space Res.*, **3**, 51 (1983).

Müller, G., *J. Crystal Growth*, **99**, 1242 (1990).

Müller, G., Schmidt, E. and Kyr, P., *J. Crys. Growth*, **49**, 387 (1980).

Mullins, W.W. and Sekerka, R.F., *J. App. Phys.*, **34**, 323 (1963).

Naumann, R.J., *Microgravity Materials Sciences: Historical Development*, in: Reuerbacher, B., Hamacher, H. and Naumann, R.J., (Eds.), *Materials Sciences in Space: A Contribution to the Scientific Basis of Space Processing*, Springer-Verlag, Berlin (1986), pp.11-30.

Nield, D.A., *J. Fluid Mech.*, **19**, 341 (1964).

Oberbeck, A., *Ann. Phys. Chem.*, **7**, 271, (1879).

Oertel Jr., H., *Adv. Space Res.*, **3**, 11 (1983).

Owen, R.B., *Research in materials processing using a low gravity simulation aircraft*, in: Koster, J.N., (Ed.), *Science and Technology Series, Low Gravity Sciences, v 67*, Univelt Inc., San Diego (1987), pp.195-216.

Pearson, J.R.A., *J. Fluid Mech.*, **4**, 489 (1958).

Pellew, A. and Southwell, R.V., *Proc. of the Roy. Soc. A*, **176**, 312 (1940).

Porter, D.A. and Easterling, K.E., *Phase Transformations in Metals and Alloys, 2nd Ed.*, Stanley Thornes Ltd., U.K. (1992).

Regel, L.L., *Materials Science in Space: Theory, Experiments, Technology*, Halsted Press, New York (1987).

Rodot, H., Regel, L.L. and Turtchaninov, A.M., *J. Crystal Growth*, **104**, 280 (1990).
Ruddle, R.W., *Solidification of Casting*, Institute of Metals, London (1957).
Rutter, J.W. and Chalmers, B., *Can. J. Phys.*, **31**, 15 (1953).
Schrage, D.S., *J. Crystal Growth*, **205**, 410 (1999).
Schwabe, D. and Scharmann, A., *Adv. Space Res.*, **8**, 175 (1988).
Shlichta, P.J., *J. Crystal Growth*, **119**, 1 (1992).
Scott, W.B., Aviation Week and Space Technology, **162**, 62 (2005).
Scriven, L.E. and Sternling, C.V., *J. Fluid Mech.*, **19**, 321 (1964).
Sokolowski, R.S. and Glicksman, M.E., *J. Crys. Growth*, **119**, 126 (1992).
Sutton, O.G., *Proc. Roy. Soc. London A*, **204**, 297 (1951).
Swalin, R., *Thermodynamics of Solids, 2nd ed.*, John Wiley & Sons, New York (1972).
Zhao, P., Heinrich, J.C. and Poirier, D.R., *42nd AIAA Aerospace Sciences Meeting and Exhibit*, 1 (2004).
Zhao, Z., Lu, D., Liu, L. and Zhu, M., *Chinese Journal of Materials Research*, **10**, 153 (1996).
Zhao, Z., Lu, D. and Pei, C., *Chinese Journal of Materials Research*, **12**, 395 (1998).